DEVELOPMENT OF CONFORMATION-SENSITIVE PROBES TO FIBRONECTIN FOR ECM TARGETING AND IMAGING OF FIBROSIS

A Dissertation
Presented to
The Academic Faculty

by

Lizhi Cao

In Partial Fulfillment
of the Requirements for the Degree
Doctor of Philosophy in the
School of Biomedical Engineering

Georgia Institute of Technology
May 2014

DEVELOPMENT OF CONFORMATION-SENSITIVE PROBES TO FIBRONECTIN FOR ECM TARGETING AND IMAGING OF FIBROSIS

Approved by:

Dr. Thomas H Barker, Advisor
School of Biomedical Engineering
Georgia Institute of Technology

Dr. Wilbur Lam
School of Biomedical Engineering
Georgia Institute of Technology

Dr. Cheng Zhu
School of Mechanical Engineering
Georgia Institute of Technology

Dr. Harry Bermudez
School of Polymer Science and
Engineering
University of Massachusetts Amherst

Dr. Michael Smith
Department of Biomedical Engineering
Boston University

Date Approved: January 23, 2014

To my wonderful family for all their support over the years,

ACKNOWLEDGEMENTS

A PhD program is a long and arduous journey, and in this age of big science – a truly multidisciplinary endeavor. I would like to take this opportunity to thank all those who have helped me along the way to see this project to completion.

First, I would like to thank my advisor, Dr. Thomas Barker, not only for his guidance and support, but also for the freedom he gave his students to pursue interesting (and potentially risky) research projects. Dr. Barker also actively encouraged us build and foster research collaborations, and helped me in organizing my committee. For his support, I will always be grateful.

I would like to also thank Dr. Harry Bermudez who, in addition to being on my committee, was a gracious host to me in his lab during the first summer of my graduate school. Dr. Bermudez's advice and mentoring introduced me to microbiology and phage display, and is key part of this thesis project.

I would like to thank Dr. Michael Smith, whose pioneering work in this field formed the early basis of my thesis. Without his work on fibronectin fibers, no one would even consider mechanics of fibronectin fibers to be a research area. I am grateful for the advice he has given me, and for his willingness to serve on my committee.

Special thanks to Dr. Wilbur Lam, who I've known for over 8 years. Dr. Lam can be credited as the one who introduced me to research, having mentored when I was an undergraduate student. I'm very fortunate to know Dr. Lam and continue to work with his lab. I am grateful for Dr. Lam's advice and support as a committee member.

To the IBB research staff (microscope guru Andrew Shaw, PRL masters Dr. Laura O'Farrell and Kim Benjamin, and histology lab manager Aqua Ashberry) for their assistance and support in all things IBB.

And finally, to my family for their support over the years. Their inspiration and sacrifices allowed me to be a career-student. Without their unwavering support, none of this would be possible.

TABLE OF CONTENTS

LIST OF TABLES

LIST OF FIGURES

LIST OF SYMBOLS AND ABBREVIATIONS

α-SMA	alpha smooth muscle actin
AEC	alveolar epithelial cell
ANOVA	analysis of variance
BSA	bovine serum albumin
CHO	chinese hamster ovary
cFn	cellular fibronectin
CFU	colony forming unit
DMEM	Dulbecco's modified eagle's minimum essential medium
ECM	extracellular matrix
EDC	1-ethyl-3-(3-dimethylaminopropyl)carbodiimide
EDTA	ethylenediaminetetraacetic acid
ELISA	enzyme linked immunosorbant assay
FACS	fluorescence activated cell sorting
FBS	fetal bovine serum
FMT	fluorescence molecular imaging
Fn	fibronectin
HEPES	4-(2-hydroxyethyl)-1-piperazineethanesulfonic acid
HFF	human foreskin fibroblast
HRP	horseradish peroxidase
IC_{50}	concentration at which 50% inhibition of signal is achieved
IPF	Idiopathic pulmonary fibrosis
IPTG	isopropyl β-D-1-thiogalactopyranoside
IVIS	in vivo imaging system

MD	molecular dynamics
MMP	matrix metalloproteinase
MW	molecular weight
OD	optical density
PBS	phosphate buffered saline
PBST	phosphate buffered saline, with 0.1% Tween-20
PCR	polymerase chain reaction
PDMS	polydimethylsiloxane
PEG	polyethylene glycol
pFn	plasma fibronectin
PTM	post translational modifications
RPMI	Roswell park memorial Institute medium
SAM	self-assembled monolayer
scFv	human single fold antibody
SDS-PAGE	sodium dodecyl sulfate polyacrylamide gel electrophoresis
SPR	surface plasmon resonance
Sulfo-NHS	sulfo-N-hydoxysuccinimide
TAG	TYE, with 4% glucose, and 100ug/mL ampicillin
TCEP	tris(2-carboxylethyl)phosphine
TYE	medium for E. Coli culture, for 1L culture: 10g tryptone, 5g yeast extract, 8g NaCl
WB	western blotting

SUMMARY

Mechanical forces have become increasingly important for determining cell behavior and maintaining normal tissue physiology. Mis-regulation of mechanical forces has been implicated in fibrotic conditions in which the extracellular matrix of the diseased tissue is significantly less compliant compared to ECMs of healthy tissues. In the case of idiopathic pulmonary fibrosis (IPF), which affects 5 million people worldwide, the fibrotic regions are characterized by the accumulation of myofibroblasts - highly contractile cells which produce collagen and fibronectin at the leading edge of existing scars. Consequently, it is thought that abnormal myofibrolast contractility and excess matrix deposition are key drivers for fibrogenesis. Of particular interest is the ECM protein fibronectin, which can be assembled into fibers within the ECM and serve as the early provisional matrix in wound healing.

Fibronectin (Fn) has the potential to be an ECM mechanosensing protein. Both *in silico* and *in vitro* studies have indicated that Fn and its many type III repeats can be extended and partially unfolded under physiological forces. Indeed, it has been hypothesized that the unfolding/refolding phenomenon of Fn type III repeats may be a possible mechanism for relating mechanical forces in the extracellular environment to intracellular biochemical signals, through changes in the structure of Fn. It has been shown by our lab and others that conformational changes in Fn may potentially instruct cell behaviors through modulating interactions with cell surface receptors such as integrins. Additionally, altered Fn structure has been suggested to affect biochemical modifications to Fn, including enzymatic degradation and post-translational modifications. Current

studies of Fn conformational change has been restricted to non-specific adhesion-and-pulling experiments by atomic force microscopy (AFM), or studied via molecular dynamic simulations of Fn at short timescales. As a consequence, considerable debate has emerged regarding the physiological relevance of Fn conformational change *in vivo*, and it remains to be shown that Fn exists in different conformations in native ECMs.

The governing hypothesis for this project was that conformational changes imparted to Fn by mechanical forces could alter presentation of molecular epitopes to cells, and that these changes could be exploited to develop molecular probes. Such probes may be useful for both fundamental studies of Fn-integrin mechanobiology as well as for molecular diagnostic imaging of fibrosis. This hypothesis was investigated with the following specific aims:

Specific Aim 1: Investigate the role of fiber strain on conformational alterations of Fn fibers, and isolate strain-sensitive peptide probes by phage display.

Native plasma Fn was purified and deposited into *in vitro* fibers on flexible patterned PDMS membranes. Uniaxial straining of the PDMS membrane (and thus straining of the immobilized Fn fibers) was shown to correlate with the solvent exposure of known buried cysteine residues, suggesting a correlation between fiber strain and conformational change of the 7th and 15th type III Fn repeats. Phage display and selection using a random peptide library was used to isolate phage clones that targeted to Fn fibers under relaxed and strained conditions.

Specific Aim 2: Investigate conformational changes within the Fn III$_{9\text{-}10}$ region through engineered Fn fragments, and isolate specific Fn fragment targeting antibodies by phage display.

Engineered Fn fragments modeling the spatial orientation between the PHSRN and RGD sequences in the 9th and 10th Fn type III repeats was used as a model of force-induced conformational changes to the central cell binding region of Fn. (Engineered fragments: Fn$_{III9*10}$, Fn$_{III9\text{-}4G\text{-}10}$). Specific scFv antibodies were isolated by phage display and selection on these Fn fragments. One specific antibody, the H5 clone, was found to preferentially bind the Fn$_{III9\text{-}4G\text{-}10}$ fragment, and inhibited cell attachment through modulating specific Fn-αvβ3 integrin interactions.

Specific Aim 3: Explore the utility of scFv antibodies for fibronectin targeting in diagnosis and monitoring of disease progression in mouse model of pulmonary fibrosis

The H5 scFv antibody was evaluated for mechano-sensitive staining of Fn in multiple model systems. Using *in vitro* deposited Fn fibers, staining of H5 increased with increasing Fn fiber strain. In Fn within fibroblast assembled ECMs, H5 staining patterns was capable of distinguishing specific Fn fibers within the matrix, and was enhanced by treatment of cells with the contractility promoter TGF-β. On lung tissues isolated from normal and from fibrotic mice, H5 staining was more pronounced on fibrotic lung tissue and showed distinct staining patterns. In a

minimally invasive live animal model, the H5 antibody targeted to and accumulated

more in lungs of bleomycin-induced fibrotic mice compared to uninjured mice.

CHAPTER 1

LITERATURE REVIEW

Fibronectin

Fibronectin (Fn) is widely considered to be a paradigm adhesion protein, and is involved in crucial cellular and physiological processes including development, wound healing, and cancer.

Fn's most widely explored function has been to confer adhesiveness of tissue culture surface to cells by adsorption or immobilization of Fn from solution onto tissue culture surfaces, and it is for this reason that Fn has been the focus of much research. Though Fn has been well studied for over three decades, many new activities of Fn are being revealed and much remains to be elucidated about the structure-function relationship of this glycoprotein, particularly with regards to the highly modular domain structure of Fn, with its many Fn type III repeats.

At the molecular scale, Fn is a dimer of two nearly identical ~250kDa subunits linked at their C-termini by a pair of disulfide bonds. Each monomer is structurally organized and composed predominantly of repeating modules termed type I, II, and III repeats(1). These distinct domains of Fn serve functional roles that mediate binding interactions between Fn to cell surface receptors, to other ECM components, as well as to Fn itself. The N-terminal type I repeats of Fn have been shown to be essential for Fn-Fn associations for Fn fibrillogenesis and matrix assembly. As evidence, recombinant Fn proteins lacking these domains do not assemble into matrices(1), and exogenous addition

of the amino-terminal 70kDa fragment of Fn (which contain these type I repeats) have been shown to disrupt and disassemble Fn matrices(2, 3).Type II repeats of Fn are less well understood, but are thought to be involved in binding to collagens and gelatin(4). Indeed, the gelatin binding property of Fn is often used to purify Fn from plasma, and homologs of Fn type II repeats have been found in many other ECM proteins that bind gelatin(5).

Most interesting of all are the 15 to 17 Fn type III repeats that make up the majority of the protein. These Fn type III repeats are composed of seven antiparallel beta-strands that fit together to form a beta sandwich structure (6, 7). Fn type III domains are ubiquitous, found not only in Fn, but in an estimated 2% of all vertebrate proteins. This wide distribution of Fn type III domains in mammalian proteins suggested that Fn III domains are evolutionarily conserved and its unique structure may have conferred Fn type III repeats the flexibility to perform multiple functions. Unlike type I and II repeats, Fn type III repeats are not stabilized by intramolecular disulfide bonds (8). Consequently, the folded Fn type III repeats are stabilized only by non-covalent interactions and have been shown to be structurally flexible and even unfold under physiologically relevant forces (9-11).

Considerable work *in vitro* and *in silico* have suggested that Fn type III domains can be unfolded with applied forces in the range of tens to hundreds of pN(11-15). Furthermore, different Fn type III domains were found to have a range of mechanical stabilities. Among the Fn III domains that make up the III_{7-10} central cell binding domain, molecular dynamic simulation results suggested that III_{10} required the lowest threshold of force to unfold, while III_7 required the highest force (16). Both MD and AFM force spectroscopy data have also suggested that stable intermediate states of unfolding exist for Fn III_{10} domains(14, 16). Given that Fn III_{10} contains the RGD integrin binding motif

responsible for engaging a variety of integrin receptors on the cell surface, these results strongly implicate that mechanical perturbations of Fn III domains in the central cell binding domain can regulate biochemical events such as integrin engagement and affect cell processes such as adhesion and migration. Furthermore, the results inferred from III_{10} may also apply to other Fn type III repeats. Indeed, experimental evidence from Erickson and coworkers[17] suggested that multiple Fn type III repeats can undergo domain opening and unfolding both as purified proteins in solution, as well as in assembled fibers in cultured ECMs.

Evidence of Fn unfolding *in vivo* within native ECMs have not been reported, and controversy remains as to whether Fn unfolding events occur *in vivo*, or if the unfolding and extension of Fn observed *in vitro* were in fact re-orientation of the Fn molecules under force[18]. However, it is generally accepted and appreciated conformational changes in Fn do occur and may have an important role *in vivo* for mediating Fn-protein interactions [19].

In vivo, Fn is found as both soluble dimeric plasma fibronectin (pFn) and crosslinked cellular fibronectin (cFn) constituting the Fn matrix found in many cellular microenvironments. Plasma Fn is synthesized and secreted by hepatocytes, whereas cellular Fn is produced primarily by fibroblasts and assembled into an organized fibrillar matrix in an integrin-mediated, cell-dependent manner. Additionally, circulating or exogenously added plasma fibronectin can also be crosslinked into this matrix [20]. Plasma and cellular Fn differ in their domain composition, and arise due to alternative splicing of a precursor Fn mRNA transcript that can generate a number of Fn variants[21-23]. Splicing can occur in the variable (V) region that connects III_{14} and III_{15}, but also in inclusion/exclusion of specific Fn type III domains. Of all the Fn type III domains in human

Fn, 15 are constitutively included, and 2 are alternative spliced. These two are termed "extra" domains, or EDA and EDB domains. Plasma Fn produced by hepatocytes contains very little to no EDA and EDB domains, whereas Fn synthesized by other cell types are much more heterogeneous, and the inclusion of EDA and EDB domains is cell type specific. Functionally, Fn containing EDA is found at higher levels in tissues where the cells are actively migrating: such as during embryonic development, wound healing, or surrounding tumors (24). The presence of EDA is thought to destabilize adjacent Fn type III domains, reducing the forces needed to unfold them (25, 26). This may be yet another mechanism by which mechanic forces can affect the structure of Fn and alters its protein binding activities.

Integrins are the most well studied receptors for Fn. Integrins are heterodimeric cell surface receptors that link the ECM to the cytoskeleton, with as many as 12 distinct integrins having been shown to be capable of ligating to Fn (27). The classical Fn integrin is integrin $\alpha 5\beta 1$, and binds to the RGD recognition motif in III_{10} - this is one of the most well studied Fn-integrin interactions. The interaction between integrin $\alpha 5\beta 1$ and RGD is also dependent on the adjacent PHSRN "synergy" site in III_9, which greatly enhances binding of $\alpha 5\beta 1$ to Fn, presumably by binding to the $\alpha 5$ subunit and altering its conformation. Other integrins, such as $\alpha v\beta 3$, $\alpha 4\beta 1$, and $\alpha 4\beta 7$ also bind to Fn at specific recognition sites(1).

In addition to integrins, Fn can also bind a variety of extracellular ligands: including fibrin(4), collagens and gelatin(4), heparin(28), and tenascins(29, 30). More recently, binding sites for heparin sulfate and growth factors such HGF and VEGF have also been found(31). Even many bacterial proteins target Fn as a method to attach to and colonize

their hosts (32, 33). This large number of protein binding partners has prompted investigators to hypothesize that perhaps with its modular structure rich in binding sites, Fn can regulate the distribution, activation, and presentation of growth factors and proteins to cells(31). This fundamentally changes the view that Fn, and indeed the ECM as a whole as passive scaffolds, and instead supports the view that ECMs can actively guide and direct cellular processes. In this new paradigm, the role of mechanical forces and Fn conformational changes becomes ever more important. Mechanical forces can allow for dynamic regulation of cell-ECM interactions, a concept supported by the many binding sites in Fn type III domains that have been characterized as so called "cryptic" binding sites(34-36), in which binding of the protein of interest only occurs under unfolded or conformationally open conditions.

Fn also contains a number of enzymatically active regions and can undergo a number of post-translational modifications, the extent of which is different for Fn in different tissue and in different environments. The list of PTMs to Fn include phosphorylation, sulfation, acylation, and glycosylation. The significance of these modifications is not well known, but it has been observed that Fn from cultured cells contain much less sugar content than Fn from embryonic fibroblasts(4). Both plasma and cell derived Fn can be enzymatically digested by tPA, urokinase, and other matrix metalloproteinases(37). Though these digestion sites have been largely determined (38), it is unclear whether enzymatic digestion of Fn is dependent on Fn conformation state. However, it is reasonable to hypothesize that Fn conformational changes may play a role, as MMP mediated degradation of the Fn matrix is thought of as an early event in malignant transformation, where cells are actively exerting contractility forces on their ECMs.

Integrins

Integrins comprise a family of heterodimeric transmembrane receptors that link the cell cytoskeleton to the ECM(27). The name for the integrin family of receptors was termed to describe this structurally related family of receptors for their function in *integrating* the extracellular matrix proteins with the cytoskeleton for mediating cell migration and adhesion. Currently, 8 distinct integrin β subunits, and 18 distinct integrin α subunits have been discovered. Together, 24 distinct integrin receptors have been observed to form from the noncovalent association of α and β subunits(39).

A considerable body of literature exists that describe the structural biology of integrin receptors(40, 41), including requirements for divalent cation binding(27), intracellular signaling events that mediating integrin inside-out-signaling(42-44), and conformational changes that results in switching from the low-affinity to high affinity conformations(45, 46).

Integrins play a critical role in the assembly of Fn into fibrils within the ECM(47). As evidence, Fn matrix assembly is integrin dependent, and cells lacking the α5 and αV integrin subunits fail to assemble Fn into fibrils, even though the protein is still secreted normally by the cells(48). Though many integrins can bind to Fn, integrin α5β1 is the major Fn integrin that cells use to engage and assemble Fn molecules into the matrix (49, 50). The two most well studied Fn integrins, α5β1 and αvβ3, both engage the RGD site within the 10th Fn type III repeat. Integrin α5β1, however, can simultaneously engage both the RGD and the PHSRN ("synergy") site in the 9th Fn type III repeat for high-affinity Fn-integrin interactions(51). Furthermore, recent evidence suggested that integrins α5β1 and αvβ3 can work together to optimize fibroblast rigidity sensing on a Fn-based substrate (52), and may have implications for cell migration and invasion in fibrotic pathologies and cancer.

Thus, investigators have hypothesized that alterations in the molecular spacing between the RGD and PHSRN sites may result in an integrin "switch" in which force-actuated

changes to molecular conformations of the FnIII9-10 region can result in differential integrin engagement and possibly mediate different signaling events. Such a mechanism, if confirmed, could offer a powerful tool for researchers to engineer integrin-specific cell response by control of the ECM for tissue engineering and regenerative medicine applications(53). Evidence of this integrin switch has not been demonstrated *in vivo*, due to the lack of appropriate molecular probes.

Phage Display

 Phage display is a technique whereby functional motifs are presented at the surface of bacteriophage coat proteins by fusion to the viral coat protein genes (54, 55). These functional motifs are most often peptides or single chain antibodies, but other forms of display technologies are also possible (56-58).

 The power of phage display is realized from the generation of large libraries of phage displayed peptides or antibodies and the ability to link the displayed motif with the genotype. Conceptually, this library can then be screened against a target molecule to isolate specific binding motifs, without *a priori* knowledge of the binding site structure or sequence. Randomization of the peptide or antibody repertoire occurs at the genetic level, whereby random oligonucleotides can be generated by PCR and ligated into vectors. Design of the random oligonucleotide library can be fully degenerated, where all 20 amino acids are represented equally, or biased towards a specific subset of amino acid by randomizing at only certain positions in the codon triplet (56). It may be desirable to avoid certain amino acids, or avoid certain stop codons when expressed in microorganism hosts. After the generation of a random oligonucleotide library, these random fragments are then ligated into digested vectors and transformed into competent *E. Coli*. cells. The diversity, or different number of possible displayed peptides, is determined by the length and manner of randomization (ie. a fully degenerate 10-mer library will have a diversity of 2^{10} different

peptides). However, this can be limited by the transformation efficiency of host cells. For *E. Coli*, this is usually limited to 10^9 transformants per 1ug of DNA (56).

Phage display screening procedures consists of repetitive cycles of incubation with the target, extensive washing, elution of bound phage particles, and amplification of recovered phage (59-61). After 3 to 5 rounds of panning, the pool of recovered phage is enriched for binders that target the antigen of interest. Individual clones from this pool can then be isolated, sequenced, and assayed for their ability to bind the target.

Phage display biopannings have previously been applied to Fn, where work by Ruoslahti and coworkers(62) used phage display to isolate a cyclic peptide that mimics the binding of β1 and β3 integrins to Fn. Much remains to be explored about the potential for using phage display to isolate Fn targeting peptides and antibodies, especially with regard to conformation specific peptides and antibodies. As part of this thesis, I will use phage display to isolate molecular probes that target both Fn fibers under varying mechanical strain, as well as single molecules of Fn fragments spanning the 9-10th type III repeats engineered to model molecular tension in the Fn molecule.

Pulmonary fibrosis

Tissue fibrosis is characterized by excess extracellular matrix (ECM) deposition and is associated with scarring and impairment of tissue function. In the case of idiopathic pulmonary fibrosis (IPF), a disease of unknown pathogenesis and no current cures (63), early diagnosis and monitoring may offer significant patient benefits. The pathogenesis of IPF in humans is not known, but is thought to involve cellular changes to alveolar epithelial cells (AEC) that may result from abnormal wound healing responses in the lung(64). It is thought that type I AEC, which normally serves to keep interstitial mesenchymal cells in a state of homeostasis through secretion of soluble factors, can be injured or lost. Type II AECs are then thought to proliferate and occupy spaces previously occupied by type I AECs. However, in normal wound healing, these type II AECs undergo regulated apoptosis

and remaining type II AECs differentiate to become type I AECs. In pathological conditions, this does not occur and fibroblasts (especially α-SMA expressing myofibroblast) instead accumulate in these damaged regions and secrete large amounts of ECM proteins. These large regions of scar tissue and fibroblasts are termed "fibroblastic foci" and is a characteristic marker of the disease.

There is currently no cure for IPF other than a lung transplant. However, treatment options exists that can help manage comorbidities associated with IPF, as well as investigational therapies that may help slow the progression of fibrosis. These include anti-inflammatory and immunomodulatory agents such as corticosteroids, antioxidant agents such as N-acetylcysteine, cytokines such as interferon-γ(63), and cell contractility inhibitors such as fasodil(65), among others.

The mechanics of the ECM is an underexplored area with regards to the pathophysiology and potential therapies for pulmonary fibrosis. Recent investigations, however, have suggested that reduced lung compliance is associated with increased integrin α5β1 mediated Fn deposition and basement membrane matrix assembly(66). Furthermore, our lab has shown that fibrotic lung ECM is significantly stiffer compared to normal ECM, using atomic force spectroscopy (67). Thus, it is hypothesized that the mechanical changes to the Fn matrix may be a molecular signature for progression of the disease.

Due to the severity of IPF, early detection and disease management, including monitoring of fibrosis progression, could offer significant patient benefits. To this end, non-invasive imaging of IPF has become an active area of research, with recent reports of collagen targeted MRI probes(68) as well as optical probes that are cleavable by specific MMPs upregulated in a mouse model of IPF(69). In this work, we take a similar inspiration in developing ECM targeting probes to detect biophysical changes to Fn that may occur in fibrotic ECMs.

CHAPTER 2

REAGENTS AND EQUIPMENT

Antibodies and reactive dyes

Alexa Fluor 488 TFP ester, Alexa Fluor 633 SE, and Alexa Fluor 546 C5 maleimide dyes were purchased from Invitrogen (Life Technologies, Grand Island, NY). Alexa Fluor 488 goat anti-rabbit, Alexa Fluor 546 goat anti-mouse, Alexa Fluor 546 streptavidin, quantum dots Qdot 585, and Qdot 705 antibody labeling kits were purchased from Invitrogen (Life Technologies, Grand Island, NY).Peptides were produced by solid phase synthesis (Genscript, Piscataway, NJ). Anti-myc antibody was purchased from Invitrogen (Life Technologies, Grand Island, NY). Biotinylated anti-Myc antibody and biotinylated anti-M13 antibody were purchased from Sigma (St. Louis, MO). Rabbit anti-rat Fn antibody was purchased from Millipore (Billerica, MA). Anti-beta1 integrin antibody was obtained from developmental studies hybridoma bank (AIIb2 clone, Univ of Iowa). Antibodies for flow cytometry were the following: anti-integrin α2 (10G11 clone, Millipore, Billerica, MA), anti-integrin α3 (ralph 3.2 clone, Santa Cruz Biotechnology Inc, Dallas, TX), anti-integrin α5 (P1D6 clone, Millipore, Billerica, MA), anti-integrin α6 (NKl-GoH3 clone, Millipore, Billerica, MA), anti-integrin α8 (F-11 clone, Santa Cruz Biotechnology Inc, Dallas, TX), anti-integrin αVβ3(LM609 clone, Millipore, Billerica, MA), anti-integrin β1 (TS2/16 clone, Biolegend, San Diego, CA).

Cell culture

Tg1 and HB2151 *E. Coli* cells were obtained from Geneservice (SourceBioScience, United Kingdom). Mouse primary lung fibroblasts, human foreskin fibroblasts, K562 cells, CHO-B2 and integrin αvβ3 transfected CHO-B2 cells were kindly provided from Vince Fiore (BME, GaTech). H69 cells were kindly provided by Dr. Ashely Brown (BME, GaTech). Primary lung fibroblast, and HF were maintained in growth medium of DMEM,

10% FBS, and 1% penicillin/streptomycin. CHOB2, and CHOB2- αvβ3 cells were maintained in DMEM, 10% FBS, 1% non-essential amino acids, and 1% penicillin/streptomycin. H69 cells were maintained in RPMI 1640 medium, with 10% FBS, and 1% penicillin/streptomycin. K562 cells were maintained in RPMI 1640 medium, with 10% FBS, 1% non-essential amino acids, and 1% penicillin/streptomycin. All cells were cultures in 37 ℃ incubator, with 5% CO_2 atmosphere.

Animal model

Mice (female, C57/Bl6, 8 weeks old) were obtained from Charles River Laboratories (Wilmington, MA) and were house for one week prior to bleomycin injection. All procedures were performed in accordance to Georgia Tech IACUC protocol (A12079).

Protein purification

Recombinant protein production and scFv antibody purification was performed on an AKTAFPLC liquid chromatography system (GE Lifescience, Pittsburg, PA). For recombinant protein purification, lysed product was filtered and run on a GST column (HiTrap GSTPrep, GE Lifescience, Pittsburg, PA), followed by thrombin digestions overnight to cleave GST tag, and purified fragments were separated from cleaved products by purification with GST column in series with Benzamidine column (HiTrap Benzamidine FF, GE Lifescience). For scFv antibody purification, filtered cell culture medium containing scFv antibody were pumped by a sample pump (P960) over a HiTrap ProteinA column (GE Lifescience, Pittsburg, PA) and elution using 200mM glycine, pH 2.5 buffer.

SPR

SPR experiments were performed on a BIACORE 2000 instrument (GE Lifesciences, Pittsburg, PA). Buffers used were the following: Immobilization buffer (0.1M sodium acetate, pH 4.5), quenching buffer: 1M ethanolamine, pH 9, binding buffer

(10mM HEPES, 150mM NaCl, 0.0001% Triton-X 100, pH 7.4, regeneration buffer (20mM EDTA, 1M NaCl, pH 6). SPR binding experiments were done using kinetic injections at 30 μL/min, with a 10min dissociation time. Regeneration of surface was performed using two injections of 5 μL each of regeneration buffer. SPR sensograms were processed with Scrubber2 software for double referencing, and curves were fit to experimental data using a 2-site heterogeneous surface model using ClampXP software.

Microscopy

Widefield fluorescence microscopy was performed on a Nikon Eclipse T*i* microscope, with epifluorescence illumination and standard DAPI/FITC/TRITC filter sets. Confocal fluorescence microscopy was performed using a Zeiss LSM 510 NLO w/ META MPE confocal microscope, using excitation lasers at 488nm, 545nm, and 633nm.

In vivo imaging

In vivo imaging in mice was performed on two small animal bioimaging systems. Preliminary IVIS images were acquired using Xenogen Lumina® imaging system using the following parameters: excitation: 745nm, emission, 780nm, exposure 10 seconds, medium binning, field stop: 2, stage position C. FMT images were acquired with fluorescence efficiencies corrections.

Monitoring of fibrosis progression and time course imaging with the H5 antibody was performed with fluorescence molecular tomography (FMT). Mice were imaged on a FMT 2000 fluorescence tomography system (Perkin Elmer) with 745nm laser excitation. Images were acquired and image reconstruction was performed using TrueQuant software.

CHAPTER 3

SPECIFIC PHAGE DISPLAYED PEPTIDES COULD BE DEVELOPED TO TARGET FN FIBERS OF VARYING STRAIN

We began to explore Fn conformational changes by starting our investigation using Fn in the form of fibers, specifically *in vitro* fibers deposited from plasma Fn. This approach has the advantages of ease of generation of Fn fibers of defined strain, as well as previously published reports (70, 71) suggesting that applying strain to these *in vitro* Fn fibers could result in conformational changes of Fn molecules within the Fn and concomitant unfolding of Fn type III repeats. In addition, incorporation of a small percentage of fluorescently labeled Fn molecules within the deposited Fn fibers allowed for facile imaging of the Fn fibers. Thus, using Fn fibers of varying strain, we sought to ask if mechanical straining of the fibers could result in altered presentation of molecular epitopes on the surface of the Fn fibers, and if molecular probes in the form of phage-displayed peptides could be generated against these Fn fibers of varying strain. In this chapter, we aimed to develop a platform technology to perform high throughput screening on Fn fibers of varying mechanical strain. Our intended application was to develop imaging probes targeted to Fn fibers (discussed in Chapter 6), but this approach could be adapted to other high throughput biomolecular screening on mechanically perturbed Fn fibers.
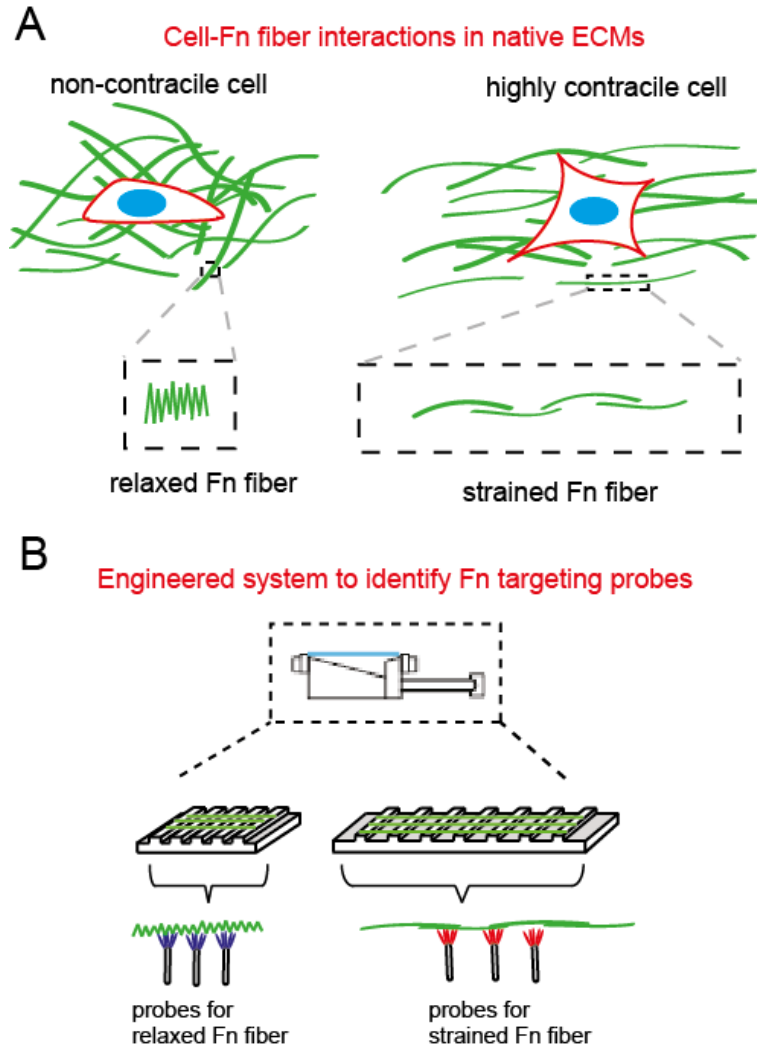
Figure 1. Integrated system for identifying conformation sensitive molecular probes for Fn fibers. A) Schematic for single Fn fibers in native ECM under different mechanical environments. Left, a relaxed Fn fiber. Right, a strained Fn fiber under loading of the ECM in the longitudinal direction. **B)** (1) Fn fibers were deposited onto chemically treated, patterned PDMS surfaces. (2) PDMS with Fn fibers were then strained using a homemade PDMS straining device capable of applying strain of up to 300%. (3)Schematic of freely suspended Fn fibers on relaxed (left) and strained (right) patterned PDMS substrates on which phage panning were performed to identify, strain specific probes for Fn fibers.

Experimental Design

Fn molecules within fibers of native ECMs are thought to adopt a range of conformations induced by applied forces **(Figure 1a).** In order to realize the goal of identifying strain-selective probes to Fn fibers, methods are needed for highly reproducible and controlled mechanical straining of pure Fn fibers. To this end, we manually extruded Fn fibers onto flexible PDMS membranes and aligned them perpendicular to the long axis

of micropatterned plateau/trough structures as previously described with minor modifications (72-74). Subsequent crosslinking of Fn fibers to the PDMS allowed for the suspension and controlled straining of fibers using a uniaxial mechanical straining device (**Figure 1b steps 1, 2**). The second element of our strategy consisted of applying a random phage display library to interrogate the Fn fiber surface **(Figure 1b, step 3).** Strained or relaxed fibers were placed in a holding chamber to enable phage incubation under controlled conditions. The phage enrichment process followed a typical workflow starting with a randomized library (10^{12} clones of 6.4×10^7 diversity).

Materials and Methods

Purification of Fn from plasma and fluorescent labeling

Fibronectin was purified from frozen pooled human plasma (Red Cross, Douglasville, GA) following a gelatin affinity chromatography protocol (75). Frozen plasma aliquots were thawed in a 37 °C water bath, and residual red cells were removed by centrifugation. Phenylmethylsulfonyl fluoride (PMSF) was added to inhibit serine proteases, and plasma was then filtered over a packed Sepharose 4B column (GE lifesciences, Pittsburg, PA), then over a packed Gelatin Sepharose column (GE lifesciences, Pittsburg, PA). Bound Fn was eluted from the column by 6M urea, and refolded by dialysis into PBS overnight at 4 °C. Purified Fn was verified by SDS-PAGE and western blotting against Fn. Labeling of purified Fn with Alexa Fluor 488 was done by addition of 10% by volume of 1M sodium bicarbonate (pH 9) to Fn in PBS, then reaction with 20X molar excess of Alexa Fluor 488 TFP ester for 1 hour at room temperature. Unreacted dye was removed by overnight dialysis into PBS at 4 °C. For Fn fiber deposition, labeled Fn was mixed with unlabeled Fn in 5-95 (w/w) ratios, at a final concentration of 1mg/mL.

Fn fiber deposition:

Substrates for Fn fiber deposition were prepared on PDMS by soft lithography, features were 10μm by 100μm ridges, separated by 50μm spacing. Masks were designed in CAD software and silicon masters were fabricated using standard photolithography. Fn was purified from frozen human plasma by gelatin-sepharose affinity chromatography. Fn fibers were deposited on PDMS from 1mg/mL concentrated solutions as previously described (73, 74). For phage display panning, the deposited fibers were allowed to air dry, and non-fibrillar Fn spots were blocked with 2mg/mL gelatin. The substrate was then blocked with 10mg/mL BSA for 1 hour, strained to defined amounts using a homemade straining device (**Figure 1b**), and a holding chamber was formed with cloning cylinders (6mm diameter, Corning, Corning, NY) for incubation for phage or antibodies.

Phage display panning:

Fuse5 6-mer phage library on Fn fibers:

A negative screen was first performed with BSA and gelatin-blocked PDMS. An aliquot containing 10^{11} phage from the fuse5 6-mer library (gift from Dr. George Smith, Univ of Missouri, Columbia, MO) was incubated for 1 hour on the blocked PDMS, with gentle shaking. Supernatant phage were collected and amplified by infection of 10mL of starved Tg1 *E.Coli.* cells and grown overnight in LB broth, 15μg/mL tetracycline, and 1mM IPTG. Phage particles were precipitated from overnight cultures by first centrifuging the cultures at 10,800g for 15 min then adding 15% (by volume) 3.3M NaCl and 25% w/v PEG 8000 to the culture supernatant. After overnight precipitation at 4°C, the solution was centrifuged at 6000g for 45 min and the phage pellet was resuspended in PBS. Phage physical concentration was determined using UV/Vis spectroscopy (CFU/mL = $(A_{269nm}-A_{320nm})/9225 \times 6 \times 10^{17}$)and 1×10^{11} phage particles were used as the input for first round of positive selection. Phage were allowed to incubate on deposited Fn fibers for 1 hour, followed by incubation with wash buffer (PBS, 0.05% tween-20) for 10 min, and eluted with 0.2M glycine, pH 2.1, and neutralized with 1M Tris-HCl, pH 9. Eluted phage were

propagated into Tg1 cells, and purified as above. Three rounds of selection were performed in parallel on both relaxed and strained Fn fibers. Stringency of selection was controlled by subsequently increasing the number of wash steps prior to phage elution for each successive screen.
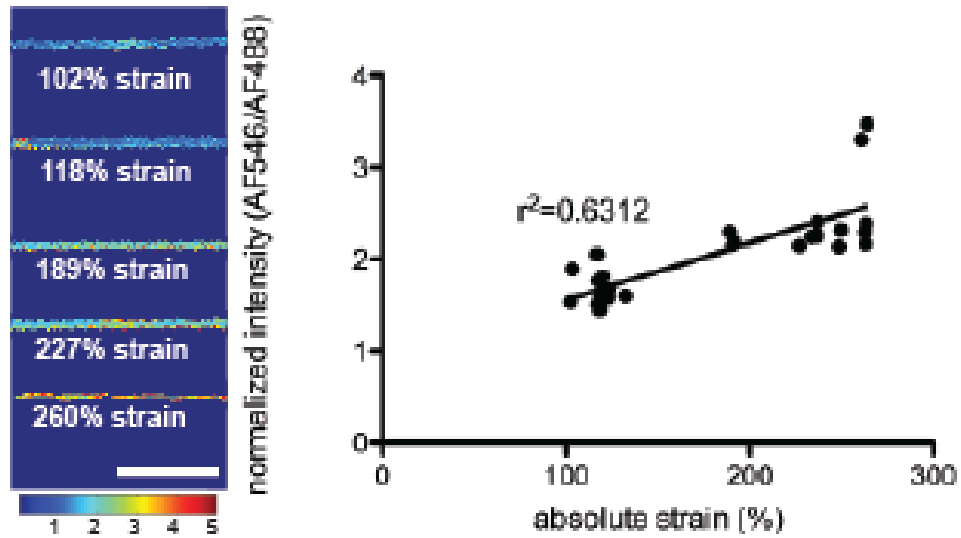
Figure 2. Cysteine exposure within III₇ and III₁₅ correlate with Fn fiber strain. A thiol-reactive compound (AlexaFluor 546-maleimide) was used to detect the unmasking of the buried free cysteine residues in FnIII₇ and FnIII₁₅. Images were acquired at 63X, shown is normalized intensity of AF546 channel divided by AF488 channel. Scale bar is 20 μm.

Results

Straining of Fn fibers immobilized on PDMS exposes buried cys in FnIII$_7$ and FnIII$_{15}$

As a first step to establish that mechanical straining of Fn fibers *in vitro* can result in measurable conformational changes in Fn type III repeats, and to validate our experimental system for Fn fiber straining - we followed an assay to detect the exposure of buried cysteine residues within 7th and 15th Fn type III repeats. Using a uniaxial straining device we were able to apply tension to the patterned PDMS substrate and achieve strains of the deposited Fn fibers exceeding 260% without significant breaking of Fn fibers. Because the Fn fibers were crosslinked to the underlying PDMS substrate, strain applied to the PDMS will be equivalent to the strain applied to the Fn fibers.

We quantified the exposure of cryptic cysteine residues in 7th and 15th type III domains using a modified cysteine shotgun method(76). We observed increasing exposure of the buried cysteine residues with increasing Fn fiber strain **(Figure 2)**. Normalized images of the reporter dye to total amount of Fn displayed increasing thiol-reactive reporter dye binding with increasing strain of the PDMS (top to bottom). Analysis of at least 25 Fn fibers displayed a robust and linear (r^2=0.63) relationship between Fn fiber strain and exposure of cryptic cysteine residues. We note that it is likely for other domains of Fn in addition to III$_7$ and III$_{15}$ to also be partially unfolded as a result of the applied macroscopic strain, as literature reports suggests that III$_7$ is among the strongest Fn type III repeats in terms of structural stability, while III$_{10}$ is among the weakest(16).

Table 1. Sequences of isolated phage following selection on Fn fibers. Clones were sequenced after 3 rounds of panning.

Phage clone	Sequence	Identification freq.
fuse5-s1	**SRWYRI**	5
fuse5-12	ARIRSN	2
fuse5-s5	**RFSAFY**	2
fuse5-34	AFAFNT	1
fuse5-19	AGQSVR	1
fuse5-16	ALSYGH	1
fuse5-40	AWTGSL	1
fuse5-39	EVIRQR	1
fuse5-03	**GHVTRN**	1
fuse5-11	GIYLLP	1
fuse5-15	GKPHGW	1
fuse5-25	IGGVSR	1
fuse5-21	KPSGLY	1
fuse5-24	KPTTVD	1
fuse5-35	LTRKSD	1
fuse5-07	LVGVLS	1
fuse5-33	PESSIG	1
fuse5-23	PPNDVH	1
fuse5-05	PRNLRQ	1
fuse5-22	QAPSFR	1
fuse5-28	RLVHGP	1
fuse5-27	RTVKYW	1
fuse5-14	SSHWFT	1
fuse5-31	SSSRTQ	1
fuse5-17	SSTYGH	1
fuse5-02	TGRRID	1
fuse5-20	TLAKAH	1
fuse5-32	TRSGGK	1
fuse5-13	TVLVGQ	1
fuse5-10	VRGVTL	1
fuse5-01	**VTRLLH**	1
fuse5-29	WRAKLV	1
fuse5-04	**WRVLYA**	1
fuse5-36	WSYILS	1
fuse5-41	YFFVDT	1
fuse5-30	YIQDYN	1
fuse5-38	YTHLAK	1
----	----	----
fuse5-c20	**LNLPHG**	3
fuse5-c12	**ARERFY**	2
fuse5-c11	**GSNSKY**	1

Isolation of specific phage clones targeting Fn fibers under varying strain

A Negative selection

B Round 1 panning

C Round 2 panning

D Round 3 panning

☐ Relaxed Fn fibers   ■ Strained Fn fibers
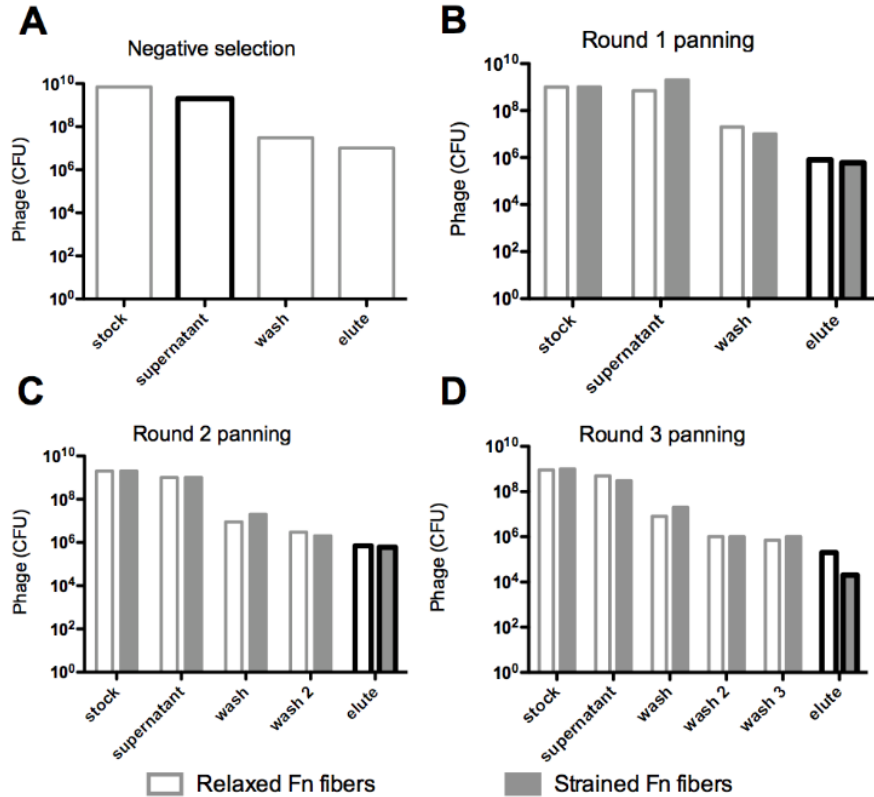
Figure 3. Enrichment of a population of phage binding to Fn fibers following 3 rounds of phage panning on Fn fibers. A) Negative selection round to deplete library of nonspecific binders to surface. **B-D)** 3 successive rounds of panning, with stringency of binding controlled by number of wash incubations.

We performed phage display pannings to identify unique peptides that discriminate Fn fibers under varying strain, specifically a 'relaxed' and a 'strained' state. The fuse5 6-mer phage peptide library was chosen because the random peptides are fused to the pIII coat proteins, located at the tip of the phage, and are therefore thought to be sterically favorable to probing unfolded domains. Furthermore, the relatively low number of copies of pIII per phage makes multivalent binding less likely and as a result yields higher affinity interactions. Our panning strategy involved an initial negative selection step to remove phage clones that bound to other targets besides Fn fibers, specifically gelatin and serum albumin. Supernatant phages (i.e., unbound phage) from this negative selection were then

amplified and used for the round one of positive selection. Positive selection was performed on both 'relaxed' (extension ratio = 1.0; $\lambda = \ell / L$) and 'strained' ($\lambda = 2.6$) Fn fibers. After each round of selection, all phages were collected and accounted for by phage titers, ensuring enrichment of a population of phage that bound strongly to the Fn fibers under each condition (**Figure 3**). After a total of three rounds of positive selection, each with increasing stringency, phage clones were isolated from individual Tg1 *E. Coli.* colonies and phage DNA was sequenced (**Table 1**)**.** Translated sequences revealed multiple identical sequences recovered from different colonies, suggesting enrichment of selective sequences from the initial repertoire of random peptides. No clear homology was identified comparing sequences within each population (derived from relaxed or strained fibers). However, considering the short length of the randomized peptide sequence and the structural complexity of Fn fibers, this result was not unexpected.

Eight of the identified phage clones were then individually produced and purified, and their binding to Fn fibers characterized by standard phage titer counts (**Figure 4**).
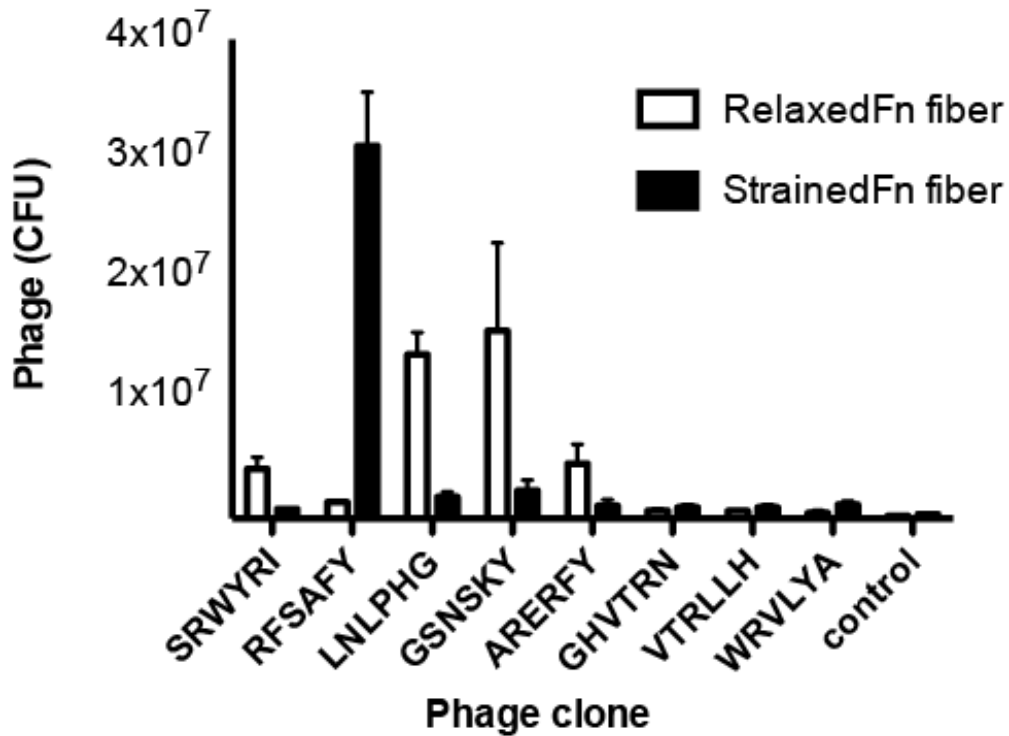
Figure 4. Binding of phage clones to Fn fibers of low and high strain. Eight clones were individually assayed for their binding to Fn fibers. 1 X 10^{11} phage were used per experiment. Control phage was phage population after round 3 of panning

Five clones of the 8 tested displayed significant ($>10^7$ CFU) and strain-selective binding to Fn fibers. Of particular interest were the clones displaying peptide sequences LNLPHG and RFSAFY. These two phage clones showed the greatest binding to Fn fibers and the greatest efficiency in discriminating between relaxed and strained Fn fibers. The clone RFSAFY preferentially bound to strained fibers over relaxed fibers (3.1×10^7 CFU compared to 1.4×10^6 CFU, or a selectivity of 22.1) whereas clone LNLPHG preferentially bound relaxed fibers over strained fibers (1.4×10^7 CFU compared to 1.8×10^6 CFU, or a selectivity of 7.8). Clones displaying SRWYRI and ARERFY peptides showed good discrimination between relaxed and strained fibers (both binding relaxed), but their overall
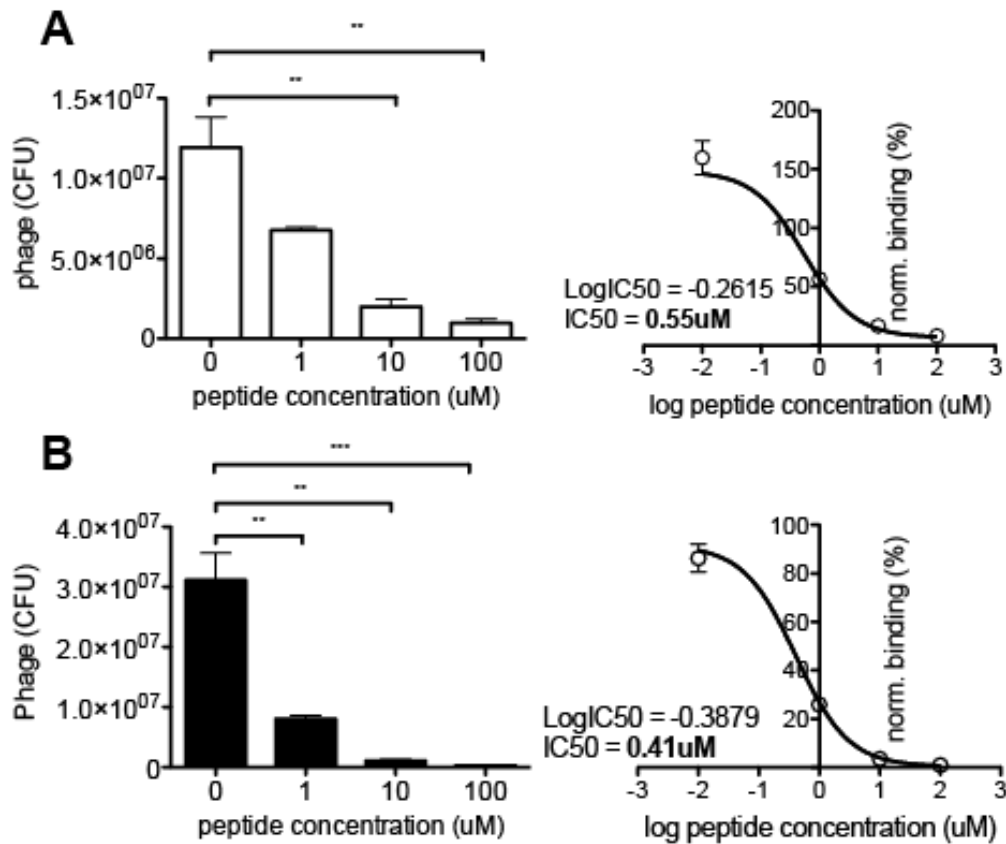
Figure 5. Competitive binding of phage clones with corresponding soluble peptides on Fn fibers of low and high strain. Two phage clones that show the greatest dynamic range in difference between binding closed compact (top, LNLPHG phage) and partially unfolded (bottom, RFSAFY phage) Fn fibers were characterized for their binding specificity. Each phage clone was co-incubated with its corresponding displayed peptide at increasing concentrations. Data was fitted using a nonlinear log(inhibitor) vs. normalized response fit and IC_{50} values were calculated to 0.55 μM for LNLPHG-phage, and 0.41 μM for RFSAFY-phage. N > 3 for all samples, error bars are SEM, Statistics were performed using a one-way ANOVA with Bonferroni post-test correction. (**, p<0.01)

binding efficiency to Fn fibers was significantly lower. The only other clone that displayed significant binding to Fn fibers was GSNSKY, which bound preferentially to relaxed fibers (1.5×10^7 CFU) but had greater variability, as evidenced by the standard error of repeated titer counts. Based on these observations, clones LNLPHG and RFSAFY were chosen for competitive binding assays with their corresponding soluble peptides (**Figure 5**).Binding of each phage clone to its antigen (LNLPHG to relaxed Fn fibers (**A**), RFSAFY to strained Fn fibers (**B**)) was found to be inhibited in a dose-dependent manner when co-incubated with its corresponding soluble peptide, indicative of peptide-mediated binding and not
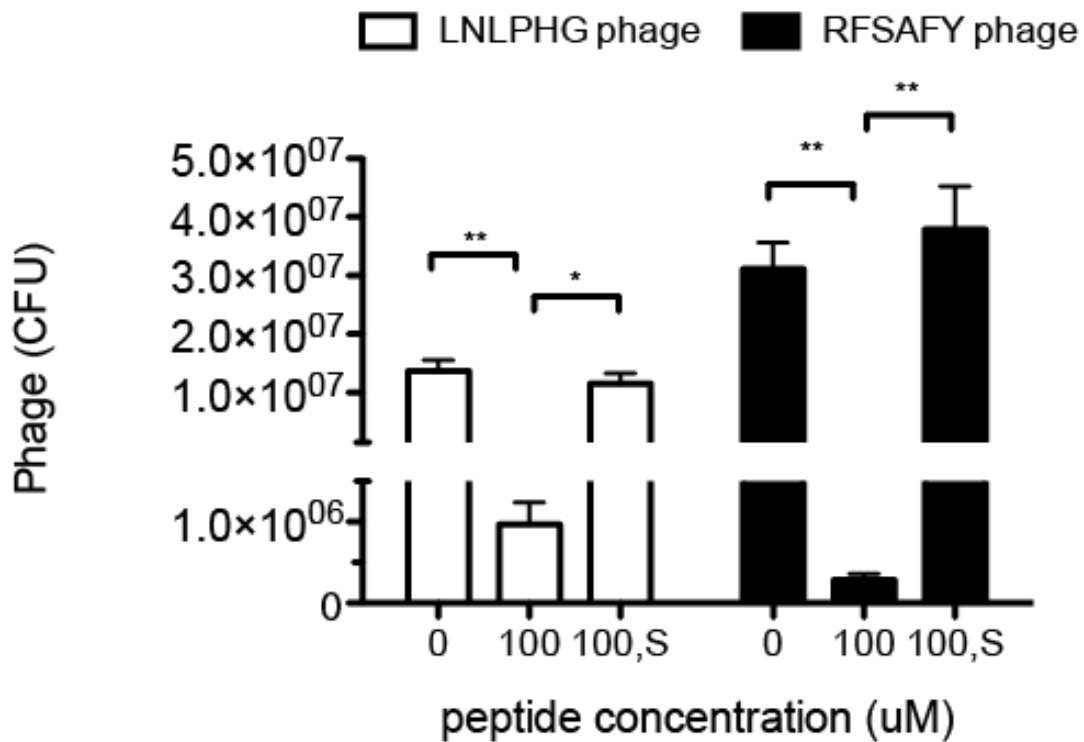
Figure 6. Scrambled peptides do not inhibit phage binding to Fn fibers Phage clones displaying either the LNLPHG or RFSAFY peptide were incubated with its corresponding peptide or a scrambled peptide (HLNPGL or AYSRFF) at 100 μM in the presence of relaxed ($\lambda = 0.93$) or strained ($\lambda = 2.64$) Fn fibers, respectively. Incubation with 100 μM peptide that matched the phage-displayed peptide showed competitive inhibition (labeled "100"), whereas incubation with scrambled peptides did not (labeled "100, S"). N > 3 for all samples, error bars are SEM, Statistics were performed using a one-way ANOVA with Bonferroni post-test correction. (*, p<0.05, ** p<0.001)

nonspecific phage-related effects. Calculation of the IC_{50} from the competitive binding data indicates nanomolar IC_{50} for both LNLPHG- and RFSAFY-antigen interactions (550 nM and 410 nM, respectively). Furthermore, inhibition was not observed when phage clones were incubated with scrambled versions of the peptides at 100 μM concentration (**Figure 6**), demonstrating specificity of the interactions. Binding of the LNLPHG phage clone to relaxed Fn fibers, and of the RFSAFY phage clone to Fn fibers were found to be reversible **(Figure 7),** whereby strain application after phage incubation can displace bound phage from Fn fibers.

Discussions and Conclusion
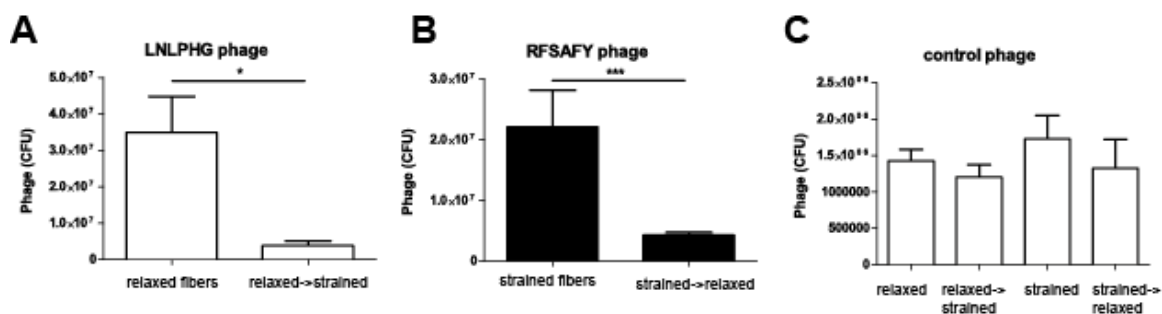
Figure 7. Reversibility of phage binding. A) LNLPHG Phage (1e12 CFU) was incubated on relaxed Fn fibers (λ=0.93) for 30mins, fibers were then strained to λ=2.6 and phages were recovered and quantitated by titers. B) RFSAFY Phage (1e12 CFU) was incubated on strained Fn fibers (λ=2.6) for 30mins, fibers were then relaxed to λ=1 and phages were recovered and quantitated by titers. C) control phage (1e12 CFU) incubated on Fn fibers, and recovered after strain application. (statistics performed using t-test, 2 tailed *, p<0.05, ***, p<0.001)

In developing a platform to interrogate the mechanics of Fn fibers, we discovered that indeed Fn fibers of varying strain present molecular epitopes in the form of alterations in the conformations of specific Fn type III repeats, observable by monitoring exposure of known buried cysteine residues. Furthermore, we showed that these biophysical changes to Fn fibers could be exploited to develop targeting agents using molecular evolution techniques such as peptide phage display. Using such an approach, we isolated two phage-peptide probes displaying the LNLPHG and RFSAFY peptides, that bound relaxed (λ=0.93) and strained (λ=2.6) Fn fibers, respectively. Furthermore, we demonstrate that specificity and reversibility of the peptide mediated interactions, and showed that soluble peptides could effectively inhibit binding of the phage-peptide probes to their corresponding targeted Fn fibers.

However, these peptide based probes have a number of important limitations. Indeed, as our later imaging characterization showed, the relatively low binding affinities of these peptide based probes limit their usefulness in fluorescent imaging applications. More importantly, we recognize that the molecular surface of Fn fibers are heterogeneous and not well defined. As such, the binding epitopes of the peptide-based probes are unknown. To address these issues, we next sought to engineer a better defined system to

investigate Fn conformational change in a force-sensitive region of Fn, and employed antibody phage display and selection methods to isolate high affinity binding antibodies to our model proteins.

CHAPTER 4

DEVELOPMENT OF ANTIBODIES THAT TARGET MOLECULAR-STRAIN WITHIN THE FNIII$_{9\text{-}10}$ REGION

The central cell binding domain of Fn spans the 7th through 10th Fn type III repeats, and is perhaps the most biologically active portion of the molecule in terms of engaging integrin receptors and mediating cell-ECM adhesions. Indeed, the RGD peptide sequence is derived from the 10th Fn type III repeat(77), and is perhaps the most widely used peptide sequence to confer adhesiveness to implanted biomaterials(78) and for targeted delivery of cargo to specific integrin-expressing cells(79).

The central cell binding domain of Fn is also exquisitely sensitive to conformational perturbations resulting from mechanical forces exerted by cells on the ECM. Reports suggested that the relative separation distance between the "synergy" PHSRN sequence in the 9th Fn type III repeat and the RGD site in the 10th Fn type III repeat is critical for engagement and activation of integrin $\alpha5\beta1$(80). Indeed, a synthetic peptide-amphiphile consisting of the sequence PHSRN-(SG)$_5$-RGD, in which the PHSRN and RGD sites were separated by 3.7nm, has been shown to specifically engage integrin $\alpha5\beta1$(81) and promote robust cell adhesion and spreading(82). This peptide, termed the PR_b peptide, has similar bioactivity as full length Fn in *in vitro* cell adhesion assays (82-84), and has been used as a targeting motif in functionalizing liposomes and other carriers for targeted delivery drug and gene delivery both *in vitro(85, 86)* and *in vivo(87, 88)*.

These observations led us to hypothesize that force-induced alterations in the conformational state of the FnIII$_{9\text{-}10}$ region may serve as a mechanosensor and "integrin switch" – that is, differential integrin engagement of Fn may result from conformationally alteration to integrin binding domains of Fn. This differential integrin engagement may then mediate different cell signaling events and perhaps alter cell phenotypes. Developing

antibody based probes to detect these conformational changes in the integrin binding FnIII$_{9-10}$ region was thus the aim of this chapter.
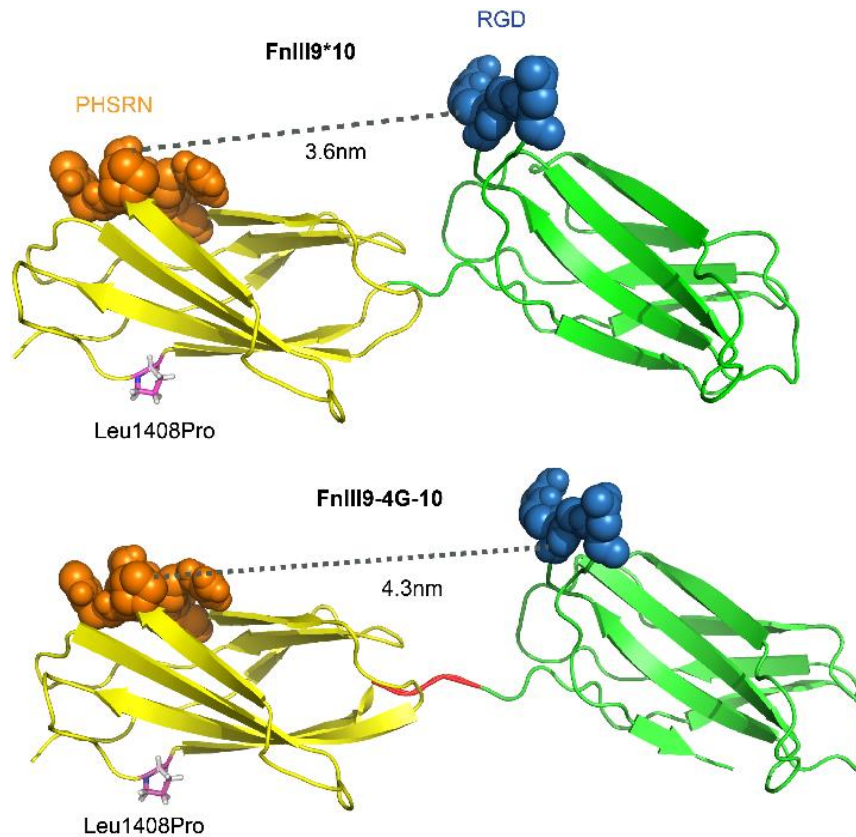
Figure 8. Structural models of recombinant Fn fragments mimicking molecular strain.
(top) stabilized 9*10 mutant, (bottom) 4 glycine insertion mutant. Molecular visualization was performed in PyMol software, 4 glycine insertion was assumed to adopt alp

Experimental Design

We sought to take a similar approach as our earlier work of phage-peptide probes developed on Fn fibers of varying strain. First, we engineered two Fn fragments spanning the FnIII$_{9-10}$ region (**Figure 8**), one fragment was a stabilized fragment (Leu^{1408}Pro mutation) mimicking the native active FnIII$_{9-10}$ conformation (80, 89), while the second fragment introduced 4 glycine insertion mutations in the linker region between III$_9$ and III$_{10.}$ These insertion mutations were created to model the increase in separation distance between PHSRN and RGD that could result from force-induced conformational changes to the central cell binding domain of Fn. Next, we performed phage display pannings using antibody libraries, and isolated human single fold antibodies (scFv) that were capable of

28

distinguishing the two model Fn fragments in an ELISA assay. Purified antibodies were quantified to their binding affinities to the two model Fn fragments by SPR. Finally, we characterized the ability of one particular antibody clone (H5) for the ability to selectively modulate Fn-integrin interactions, using cell attachment assays with engineered cell lines expressing specific integrin receptors**.**

Materials and Methods

Cloning and production of Fn fragments

Fn DNA was isolated from pFH154 plasmid (ATCC, Manassas, VA), and PCR amplification of Fn fragments spanning specific FnIII repeats was performed with following primers:

Forward primers:

(1)FnIII5:5'AGTC<u>GTCGAC</u>**TG**GAACAAAAACTTATTTCTGAAGAAGATCTGAAA CTGGATGCTCCCACTAA-3',

(2)FnIII6:5'AGTC<u>GTCGAC</u>**TG**GAACAAAAACTTATTTCTGAAGAAGATCTGCCT GGGAGCTCTATTCCACC-3',

(3)FnIII7:5'AGTC<u>GTCGAC</u>**TG**GAACAAAAACTTATTTCTGAAGAAGATCTGCCA TTGTCTCCACCAACAAA-3',

(4)FnIII10:5'AGTC<u>GTCGAC</u>**TG**GAACAAAAACTTATTTCTGAAGAAGATCTGGT TTCTGATGTTCCGAGGGA-3',

Reverse primers:

(5) FnIII9:5'AGTC<u>GCGGCCGC</u>**CTA**GCATGTTGATTGTTGGCCAATCA-3',

(6) FnIII11: 5'-AGTC <u>GCGGCCGC</u>**CTA**GCAGGTTACTGCAGTCTGAACCAGA-3',

(7) FnIII14: 5'-AGTC<u>GCGGCCGC</u>**CTA**GCACGAGCATTGTCATTCAAGGT-3'.

Cloning vector pGEX4T-1 (GE Lifesciences, Pittsburg, PA) was digested with Sal1 and Not1 restriction enzymes (New England Biolabs, Ipswich, MA) and ligated with amplified PCR fragments digested with the same enzymes. Ligated vectors were transformed into

29

electrocompetent XL1-Blue cells, and clones were sequenced to verify successful transformations. Plasmid DNA was then isolated from transformed XL1-Blue cells, and re-electroporated into BL21 cells for protein production. BL21 cell stocks were grown in 10mL overnight cultures in 2YT + 100 μg/mL Ampicillin, 37 °C in incubator, and transferred to 1L cultures until OD_{600} reaches 0.8-1. Cells were induced to produce recombinant protein by IPTG and cultured for an additional 4 hours. Cells were pelleted by centrifugation, resuspended in PBS with complete proteases inhibitor tablet (Roche applied sciences, Indianapolis IN) and lysed by addition of lysozyme and sonication. Lysed product was filtered and run on a GST column (HiTrap GSTPrep, GE Lifescience, Pittsburg, PA) using an AKTAFPLC liquid chromatography system (GE Lifescience, Pittsburg, PA). Products was digested with thrombin overnight to cleave GST tag, and purified Fn fragments were separated from cleaved products by purification with GST column in series with Benzamidine column (HiTrap Benzamidine FF, GE Lifescience). Purified Fn fragments were checked for purity by SDS-PAGE and western blotting.

Phage displaying panning using Tomlinson I+J and human domain antibody libraries (dAb)

Fn fragments ($FnIII_{9*10}$, $FnIII_{9-4G-10}$) were coated on Nunc MaxiSorp plates (Thermo Fisher Scientific, Pittsburg, PA), (10 μg/well, 40 wells per Fn fragment) overnight at 4 °C. Next day, the plates were aspirated, and blocked with 2% milk in PBS for 1 hours to block against non-specific binding. Tomlinson I+J and human domain antibody (dAb) library (Geneservice, United Kingdom) phage pannings were performed in parallel. Phage were incubated on plates for 1 hour, and supernatant phage was collected by aspiration. To deplete binding of phages selected on $FnIII_{9*10}$ fragment for binding to the $FnIII_{9-4G-10}$ fragment, the plates were incubated with soluble Fn fragments (soluble $FnIII_{9*10}$ fragments incubated on $FnIII_{9-4G-10}$ coated plates, and *visa versa*), for 1 hour. Plates were then washed with PBST 3 times, and bound phage eluted by incubation with 1mg/mL trypsin in PBS

for 1 hour. Eluted phage were infected into freshly grown Tg1 *E.Coli.* cells from an overnight grown culture, and grown on 2YT + 4% glucose + $100\,\mu g/mL$ ampicillin plates overnight. After overnight growth on the plates, colonies were scraped off the plates and pooled to create cell stocks. To produce phage for the next round of panning, aliquots of phage-infected cell stocks were grown overnight and induced to produce phage by co-infection with KM13 helper phage, and phage purified by PEG/NaCl precipitation. Three rounds of phage panning was performed.

ELISA assay for specific binding scFv antibodies

After scFv phage pannings were completed on Fn fragments, individual scFv antibody clones were picked into wells of a 96-well plate, with 2YT + 4% glucose + $100\,\mu g/mL$ ampicillin and grown overnight at $37\,°C$ in shaker incubator. Next day, a fresh plate was inoculated with $5\,\mu L$ of overnight cultures and grown for additional 3 hours. Cells were pelleted by centrifugation, resuspended in 2YT + 0.1% glucose + $100\,\mu g/mL$ ampicillin, and 1mM IPTG to produce scFv antibodies for 16 hours at $25\,°C$, 220rpm in incubator. ELISA plates were coated with antigen ($FnIII_{9*10}$ on one half of plate, $FnIII_{9\text{-}4G\text{-}10}$ on the other half) overnight at $4\,°C$, and blocked with 2% milk in PBS for 2 hours at room temperature. Blocking solution was aspirated, and scFv antibodies were incubated in duplicates on left and right halves of the ELISA at room temperature for 1 hour. Wells were washed 3 times with PBST, and primary anti-Myc biotin antibody was incubated for 1 hour at room temperature. Well of the plate were washed 3 times with PBST, and secondary antibody (Extravidin HRP) was incubated for 1 hour at room temperature. Plates were washed 3 times with PBST, and 2 times with PBS. One-step Ultra ELISA TMB substrate ($65\,\mu L$) was incubated in the wells, until a deep blue color develops. The reaction was stopped by addition of $40\,\mu L$ of 2N sulphuric acid, and OD at 450nm was recorded using a multiwell plate spectrophotometer. Analysis of ELISA signal for each scFv

antibody was performed by the ratio of the signal from the FnIII$_{9-4G-10}$ well over ratio from the FnIII$_{9*10}$ well.

scFv antibody production in HB2151 cells

Clones identified from scFv ELISA assay were streaked out on TAG plates. For each scFv to purify, 20mL of 2YT + 4% glucose + 100 μg/mL ampicillin was inoculated with a single colony and grown for 4 hours at 37 ℃, 220rpm in incubator. To each culture, $2x10^{11}$ KM13 helper phage was added, and incubated for 1 hour at 37 ℃ water bath. Infected cells were pelleted by centrifugation, and resuspended in 50mL of 2YT + 0.1% glucose + 100 μg/mL ampicillin and 50 μg/mL kanamycin. Cultures were grown at 25 ℃, 220rpm in incubator for 20 hours to produce phage. Phages were purified by PEG/NaCl precipitation and infected into fresh HB2151 E.Coli. cells grown mid log-phase growth, OD$_{600}$ 0.4, and incubated for 30mins in a 37 ℃ water bath. Infected HB2151 cells were pelleted by centrifugation, resuspended in 0.5ml of 2YT, and plated out onto TAG plates to grow overnight at 37 ℃. After overnight growth, cells were scrapped off the plates, and frozen cells stocks were created by addition of 20% glycerol, to be stored at -80 ℃. One vial of frozen stock of scFv producing HB2151 cells was added to 1L of 2YT + 0.1% glucose + 100 μg/mL ampicillin, and grown at 37 ℃, 220rpm for until OD$_{600}$ reaches 0.8. To the culture, IPTG was added to a final concentration of 1mM to induced scFv antibody expression, and grown overnight at 25 ℃, 220rpm in the incubator. Overnight cultures were centrifuged to pellet the cells, and supernatant containing the soluble scFv antibodies were filtered using a 0.22 μm filter. Filtered media was run over a HiTrap ProteinA column (GE Lifescience, Pittsburg, PA) using an AKTA FPLC liquid chromatography system. Purified scFv antibodies were separated into aliquots, lyophilized, and stored at -20 ℃. Purity of the purified scFv was checked SDS-PAGE and WB.

scFv antibody labeling with Alexa Fluor 546 and Alexa Fluor 750

One milligram (1mg) of purified scFv antibodies was used per labeling reaction. To each reaction, 20X mole excess of TCEP was added to reduce disulfide bonds within the scFv antibodies, and 10X mole excess of the dye, either Alexa Fluor 546 C5 maleimide or Alexa Fluor 750 C5 maleimide was reacted for 4 hours at room temperature. Unreacted dye was removed by extensive dialysis against PBS. Degree of labeling was calculated using the following formula:

$$\frac{A_x}{\epsilon} \times \frac{MW \ of \ protein}{mg \ protein/mL} = \frac{moles \ of \ dye}{moles \ of \ protein}$$

Where A_x is the absorbance values at absorption maximum wavelength, and ϵ is the molar extinction coefficient of the dye. A_x = 93,000 at 556nm for Alexa Fluor 546, and A_x = 290,000 at 753nm for Alexa Fluor 750. Tomlinson I+J scFv antibodies have MW of approximately 30kDa, while dAb scFv antibodies have MW of 17kDa.

Epitope mapping of scFv antibodies with competitive ELISA

ELISA plates were coated with the Fn fragment that the scFv antibodies was isolated against (FnIII$_{9*10}$ or FnIII$_{9-4G-10}$) overnight at 4 ℃, and blocked with 2% milk in PBS for 2 hours at room temperature. The wells were then aspirated, and the scFv antibody of interest was co-incubated with soluble FnIII$_{6-9}$, FnIII$_{10-14}$, FnIII$_{9*10,}$ or FnIII$_{9-4G-10}$ in a dose dependent manner (from 0.1 μg/mL up to 100 μg/mL) for 1 hour at room temperature. Wells were washed 3 times with PBST, and primary anti-Myc biotin antibody was incubated for 1 hour at room temperature. Well were washed 3 times with PBST, and secondary antibody (Extravidin HRP) was incubated for 1 hour at room temperature. Plates were washed 3 times with PBST, and 2 times with PBS. One-step Ultra ELISA TMB substrate (65 μL) was incubated in the wells, until a deep blue color develops. The reaction was stopped by addition of 40 μL of 2N sulphuric acid, and OD at 450nm was recorded using a multiwell plate spectrophotometer. Analysis of dose dependent inhibition of scFv binding due to competitive binding of soluble Fn fragments was performed by 3 parameter

non-linear regression curve fit using GraphPad Prism software, and IC$_{50}$ inhibition values were calculated.

Cell attachment assay with scFv antibodies

This assay was developed based on a published protocol for quantitative analysis of cell-substrate adhesions(90). Wells of a 96-well tissue culture plate was coated with Fn (10 μg/ml) in PBS overnight at 4 ℃. Wells of the plate was then blocked with 200uL of 10mg/mL heat denatured BSA solution for 1 hour, at room temperature. Cells of interest were then prepared at a concentration of 2 X 10^5 cells/mL for HFF, 7.5 X 10^5 cells/mL for H69 cells, 6 X 10^5 cells/mL for CHOB2 and CHOB2-αvβ3 cells, and 1 X 10^6 cells/mL for K562 cells. To estimate 100% cell attachment, dilutions of 5%, 10%, 20%, 50%, and 100% of the working concentrations of cells were prepared and added to uncoated, unblocked wells. For assays using β1 integrin blocking antibodies, an aliquot of the cell suspension at twice the working concentration was mixed with the β1 mAb at 30 μg/mL. To test the effect of the scFv antibody, 50 μL of the scFv antibody was added to the appropriate wells, incubated for 5mins at 37 ℃, and 50 μL of cell suspension was added the wells. The plate was incubated for 20min (HFF) or for 1 hour (other cell types) at 37 ℃, with the lid removed. Wells used for estimating 100% cell attachment was fixed by adding 100 μL per well of 5% glutaraldehyde. Experimental well were washed gently 3 times with PBS, using cut-off pipette tips, and fixed for 20mins with 100 μL of 5% glutaraldehyde. Wells were washed 3 times with deionized water, and 100 μL of 0.1% (w/v) crystal violet was added to each well. After overnight staining, wells were washed 3 times with 400 μL of deionized water, crystal violet was solubilized with 10% (w/v) acetic acid, and absorbance at 590nm was recorded using a multiwell plate spectrophotometer. Data from 5%, 10%, 20%, 50%, and 100% attachment wells were used to determine the value for 100% attachment by linear regression curve fitting, and experimental data was expressed as a percentage of

input cells attached. Statistical analysis was performed using one-way ANOVA with Tukey's post-test.

Integrin cell surface staining and flow cytometry analysis

Cells (HFF, CHOB2, CHOB2-αVβ3, and K562) were harvested and resuspended at a concentration of 5×10^6 cells/mL in ice-cold FACS buffer (PBS, 10% FBS, 0.1% sodium azide). One hundred microliters (100 μL) was used for each staining condition. Cells were stained with the appropriate antibody at manufacturers suggested dilutions for 30min on ice. Cells were then washed with ice-cold PBS by centrifugation at 1500rpm for 5min three times, then resuspended in 100 μL ice cold FACS buffer. Staining with secondary antibodies, or isotype control antibodies, were performed on ice and incubated for 30mins in the dark. Cells were then washed with ice-cold PBS by centrifugation at 1500rpm for 5min three times, then resuspended in 200 μL ice cold FACS buffer and stored for analysis the same day. For storage longer than 16 hours, the cells were resuspended in 200 μL of ice cold 4% formaldehyde for 10mins, then resuspended in 200 μL ice cold PBS. Flow cytometry was performed on an Accuri C6 flow cytometer (BD Biosciences, San Jose, CA). At least 50,000 events was recorded per group. Data analysis was performed using FlowJo software, gating on the isotype controls.

Spinning disk cell adhesion strength assay

Assays of the effects of scFv antibodies on adhesion strength of fibroblasts to Fn was tested with the help of Dr. Imen Hannachi (ME, GaTech) following a similar published protocol(91). Glass coverslips (25mm diameter) were treated with oxygen plasma and coated with 10ug/ml of Fn in PBS overnight. Fn was then aspirated, and coverslips were blocked with 10mg/mL heat denatured BSA for 1 hour at room temperature. scFv antibodies or HFN7.1 antibodies were incubated on the coverslips for 1 hour at room temperature, then coverslips were washed 3 times and stored in PBS for use the same day.

Fibroblasts (HFF) were seeded at 125,000cells/cm^2 and allowed to attach for 2 hours at 37 ℃. Coverslips were spun on a spinning disk apparatus as described in (91), attached cells were fixed with 4% paraformaldehyde, and stained with DAPI. Imaging of the attached cells was performed, and image analysis was performed using home developed MATLAB script to plot adhesion fraction as function of shear stress (Garcia Lab, GaTech). Experimental points were fit to a sigmoid to obtain the τ_{50} value, or shear stress at 50% detachment of cells. Statistical analysis was performed using one-way ANOVA with Tukey's post-test.

SPR analysis of scFv antibodies binding to Fn fragments

A self-assembled monolayer of alkanethiols comprised of 20% -COOH and 80% -OH functional groups (Prochimia, Poland) was assembled on a BIACORE gold sensor chip surface, by incubation of 1mM stock alkanethiol solution on the gold chip overnight at room temperature. SPR experiments were performed on a BIACORE 2000 instrument. Fn fragments in immobilization buffer (0.1M sodium acetate, pH 4.5) were immobilized on the chip using EDC/sulfo-NHS chemistry, and unreacted –COOH was quenched by injections of 1M ethanolamine, pH 9. Dilutions of scFv antibodies were prepared in binding buffer (10mM HEPES, 150mM NaCl, 0.0001% Triton-X 100, pH 7.4) in concentrations ranging from 0.5 μg/mL to 120 μg/mL, and injected over the chip surface using kinetic injections at 30 μL/min, with a 10min dissociation time. Regeneration of surface was performed using two injections of 5 μL each of regeneration buffer (20mM EDTA, 1M NaCl, pH 6). SPR sensograms were processed with Scrubber2 software for double referencing, and curves were fit to experimental data using a 2-site heterogeneous surface model using ClampXP software.

Results

Isolation of scFv antibodies selected against stabilized Fn fragments

Engineered Fn fragments spanning the 9th and 10th type III repeats of Fn were produced as reported(51), in which a $Leu^{1408}Pro$ mutation was created to stabilize the spatial orientation of the synergy site (PHSRN) in III_9 with respect to the RGD site in III_{10} (stabilized mutant - $FnIII_{9*10}$). In native Fn, the synergy site is approximately 3.5nm away from the RGD loop, and its precise spatial location and orientation is thought to be critical for mediating high affinity $\alpha5\beta1$ integrin engagement(92, 93). An increase in this separation distance could then perhaps serve as an extracellular matrix cue to guide differential cell-integrin engagement and mediate a different cell response.
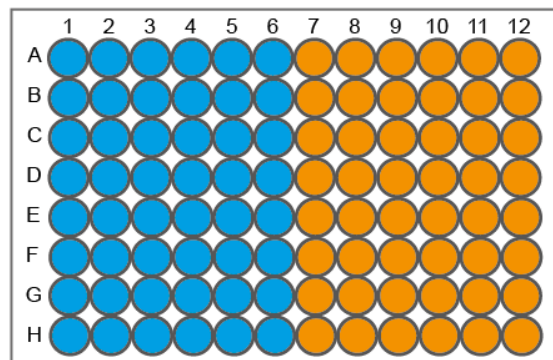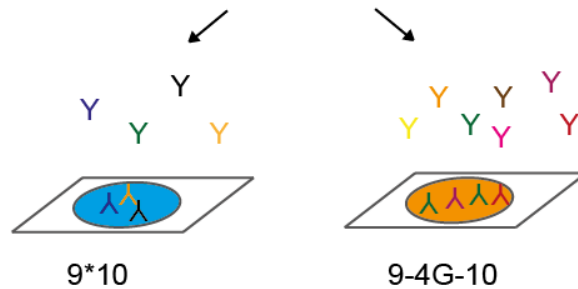
Figure 9. ELISA assay for selection of scFv antibodies following phage panning on Fn fragments. Individual scFv antibodies was produced and incubated on both $FnIII_{9*10}$ and $FnIII_{9-4G-10}$. Ratio of ELISA signal was used as a metric to assess scFv antibodies with skewed preference in binding one Fn fragment over the other.

To this end, engineered Fn fragments mimicking the extension of III_9 and III_{10} repeats were created by insertion of 4 glycine residues in the linker region between III_9 and III_{10} (**Figure 8**). This was created to model the increase in the separation distance between the synergy site in the 9th type III repeat and the RGD loop in the 10th type III repeat and may arise from mechanical loading of the Fn molecule along a fiber. Molecular visualizations in PyMol software suggested that this 4 glycine insertion increased the separation distance between the PHSRN and RGD sites to an average of 4.3nm. These fragments were produced recombinantly in BL21 *E. Coli* cells and purified using an AKTAFPLC liquid chromatography system.

Phage display and selection using human single fold (scFv) antibody has distinct advantages over peptide phage display, including higher binding affinities, ease of addition

Table 2. scFv antibodies identified by ELISA following selection on Fn fragments

scFv	Date	Library	(4G/9*10) ratio	Preference
B1	5/3/2012	Tomlinson I	2.818306	9-4G-10
C2	5/3/2012	Tomlinson I	2.256894	9-4G-10
B2	5/3/2012	Tomlinson I	1.328435	9-4G-10
G2	5/9/2012	Tomlinson I	2.547049	9-4G-10
F4	5/9/2012	Tomlinson I	1.577504	9-4G-10
G8	5/9/2012	Tomlinson I	5.009584	9-4G-10
A4	5/16/2012	dAb	0.485305	9*10
B4	5/16/2012	dAb	0.452006	9*10
D1	5/16/2012	dAb	0.601751	9*10
A8	5/16/2012	dAb	2.491379	9-4G-10
C8	5/16/2012	dAb	3.458188	9-4G-10
D7	5/16/2012	dAb	5.234991	9-4G-10
E8	5/16/2012	dAb	0.474262	9*10
F7	5/16/2012	dAb	2.776091	9-4G-10
F8	5/16/2012	dAb	1.901473	9-4G-10
E3	7/4/2012	Tomlinson I - 4G	3.171049	9-4G-10
C4	7/4/2012	Tomlinson I - 4G	2.065507	9-4G-10
G1	7/4/2012	Tomlinson I - 4G	0.514737	9*10
F1	7/18/2012	Tomlinson I - 4G	2.7782	9-4G-10
G3	7/18/2012	Tomlinson I - 4G	2.1611	9-4G-10
H5	7/18/2012	Tomlinson I - 4G	2.0163	9-4G-10
D2	7/18/2012	Tomlinson I - 4G	1.8265	9-4G-10
D2	7/18/2012	Tomlinson I- 9*10	0.1197	9*10
E4	7/18/2012	Tomlinson I- 9*10	0.1923	9*10
H5	7/18/2012	Tomlinson I- 9*10	0.2454	9*10
F7	5/3/2012	Tomlinson I- 9*10	3.1062	9-4G-10
A10	5/3/2012	Tomlinson I- 9*10	0.4958	9*10
G7	5/3/2012	Tomlinson I- 9*10	0.4997	9*10
H5	5/3/2012	Tomlinson I- 9*10	0.4453	9*10
H9	5/3/2012	Tomlinson I- 9*10	1.4553	9-4G-10
B5	7/4/2012	dAb - 4G	1.8663	9-4G-10
F4	7/4/2012	dAb - 4G	1.785	9-4G-10
G2	7/4/2012	Tomlinson I - 9*10	0.4988	9*10
H5	7/4/2012	Tomlinson I - 9*10	2.6235	9-4G-10
E2	7/4/2012	Tomlinson I - 9*10	0.582	9*10
A5	7/4/2012	Tomlinson I - 9*10	2.0489	9-4G-10
C5	7/4/2012	Tomlinson I - 9*10	2.1898	9-4G-10
E3	7/4/2012	Tomlinson I - 4G	3.171	9-4G-10
C4	7/4/2012	Tomlinson I - 4G	2.0655	9-4G-10
G1	7/4/2012	Tomlinson I - 4G	0.5147	9*10

of epitope tags, and inducible expression and purification of soluble antibodies. The scFv antibodies libraries that we chose to utilize in phage pannings was developed by Greg Winter's and co-workers by incorporating diversity at human framework V_H (domain antibody library – dAb)(94) or V_H and V_K (Tomlinson I+J library)(95). Large libraries could be generated, with diversities estimated at 1.47 x 10^8 for Tomlinson I, 1.37 x 10^8 for Tomlinson J, and 3 x 10^9 for the dAb antibody library.

Thus, by performing phage display and selection using these scFv antibody libraries on recombinant Fn fragments mimicking molecular tension in FnIII$_{9-10}$ domains, we could isolate specific antibodies with high binding affinities against a known portion of Fn that mediate specific ECM-integrin interactions.

Table 3. Translated sequences of selected scFv antibodies

H2 CDR 2	H3 CDR 3	VL CDR 2	VL CDR 3	scFv(s) with this sequence
YISTSGCSTX				B1_TomI-I_5_3_2012
SIGSYGYYTG	SAAT	NASSL	QQYYDTPYT	B2_TomI_5_3_2012, E3_TomI-4G_7_4_2012, D2_TomI-*_7_18_2012
SIYTSGYATA	SAAT			G2_TomI_5_9_2012
DIYDGGGTN	TADN	AASTL	QQANSAPTT	F7_TomI*_5_3_2012, H5_TomI4G, 7_18_2012
SIYYDGSTTG	GYDT	DASSL		G3_TomI4G_7_18_2012
	ADTSWARLNQADKLAF			A4_dAb_5_16_2012, B4_dAb_5_16_2012, D1_dAb_5_16_2012
	SWRRSPAQLRS			A8_dAb_5_16_2012, F8_dAb_5_16_2012
	RVLAMSKGQNYTMPF			C8_dAb_5_16_2012
	TSCMVDCTPESLGY			D7_dAb_5_16_2012
	TSRWARYFKLLPSNIGS			E8_dAb_5_16_2012
	TDMDDSSQALGS			F7_dAb_5_16_2012

Following phage display panning and selection, we developed an ELISA assay (**Figure 9**) to select scFv antibodies with differential targeting selectivity towards the stabilized FnIII$_{9*10}$ mutant versus the 4 glycine insertion mutant (FnIII$_{9-4G-10}$). This ELISA detected the Myc tag that was present on the scFv antibodies - and by analyzing the ratio of the relative ELISA signal of each individual antibody on binding to FnIII$_{9*10}$ vs. FnIII$_{9-4G-10}$, conformational specific antibodies could be isolated. This ELISA assay identified 40 clones (**Table 2**), of which preliminary sequencing identified 11 unique scFv antibodies (**Table 3**). Cell stocks of these antibodies were then created in HB2151 *E. Coli* production cells, and purified using an AKTA FPLC liquid chromatography system.

Characterization of scFv antibodies binding epitopes and binding kinetics to Fn fragments
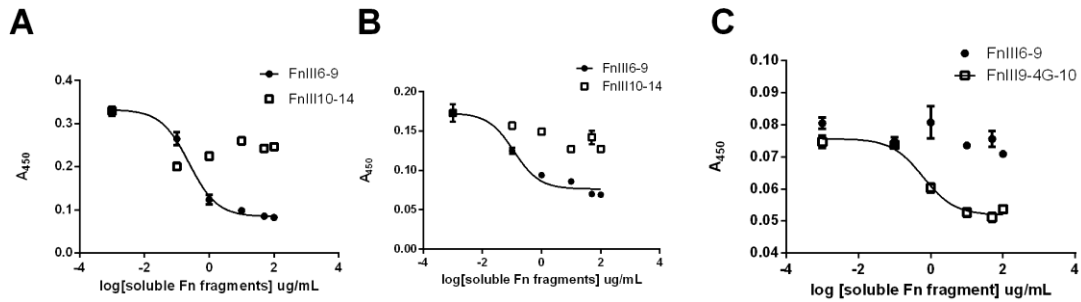

Figure 10. Epitope mapping of scFv antibodies by competitive ELISA. A) Competitive binding of soluble FnIII6-9 and FnIII10-14 with H5 antibody, on ELISA plate coated with FnIII9-4G-10, B) competitive binding of soluble FnIII6-9 and FnIII10-14 with G8 antibody, on ELISA plate coated with FnIII9-4G-10, C) competitive binding of FnIII6-9 and FnIII9-4G-14 with F8 antibody, on ELISA plate coated with FnIII9-4G-10

A competitive ELISA assay was developed to localize the binding epitope for the purified scFv antibodies of interest. To establish whether the binding epitope of each scFv is within the 9th, 10th, or spans both Fn type III repeats: soluble Fn fragments including either the 9th type III repeat alone ($FnIII_{6-9}$), or the 10th type III repeat alone ($FnIII_{10-14}$) were co-incubated with scFv antibodies on ELISA plates adsorbed with the $FnII_{9-10}$ fragments to which the scFv was selected against. By varying the concentration of soluble Fn fragments in a dose dependent manner, if the epitope that the scFv antibody recognized is also found within the soluble Fn fragments, then a dose-dependent inhibition of scFv antibody binding to the adsorbed Fn fragments is expected. This inhibition could be quantitatively determined using standard non-linear regression analysis, and IC_{50} values could be determined for each scFv antibody for which inhibition of ELISA signal was observed. Of the scFv antibodies tested (**Figure 10**), H5 and G8 scFv antibody binding were found to be effectively inhibited by soluble Fn fragments containing the 9th type III

repeat (**Figure 10A-B**), F8 scFv antibody binding was only inhibited by soluble Fn fragments including both the 9th and 10th type III repeats (**Figure 10C**).
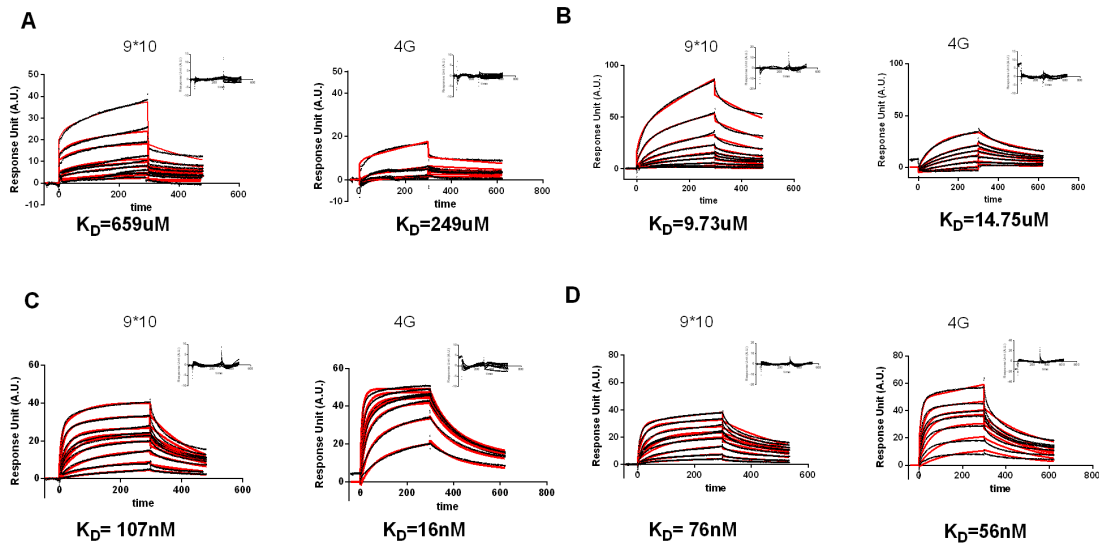

Figure 11. SPR sensograms of scFv antibodies on Fn fragments mimicking molecular tension in 9th and 10th type III repeats. Simulations are shown in red, while experimental datasets are shown in black. Insets show residuals for simulations. Fn fragment immobilized to SPR chip is indicated on each plot. **A)** A4 scFv, **B)** F8 scFv, **C)** H5 scFv, **D)** G8 scFv.

Binding kinetics of scFv antibodies to Fn fragments were evaluated using SPR. Fn fragments (100 μg/mL) were immobilized using EDC/sulfo-NHS chemistry, and kinetic binding experiments were performed using kinetic injections of the scFv antibodies analyte, with a 10min dissociation phase following each injection. Sensograms for each scFv antibody was double referenced using Scrubber2 software against both blank injections as well as to a blank sensor surface. Modeling and curve fitting was done in ClampXP software, using a heterogeneous surface model. Equilibrium dissociation constants for each scFv was determined to be the following: (**Figure 11A**) A4 scFv antibody: 659 μM for binding to FnIII$_{9*10}$, 249 μM for binding to FnIII$_{9-4G-10}$, (**Figure 11B**) H5 scFv: 107nM for binding to FnIII$_{9*10}$, 16nM for binding to FnIII$_{9-4G-10}$, (**Figure 11C**)

F8 scFv: 9.73 μM for binding to FnIII$_{9*10}$, 14.75 μM for binding to FnIII$_{9-4G-10}$, (**Figure 11D**) G8 scFv: 76nM for binding to FnIII$_{9*10}$, 56nM for binding to FnIII$_{9-4G-10}$.
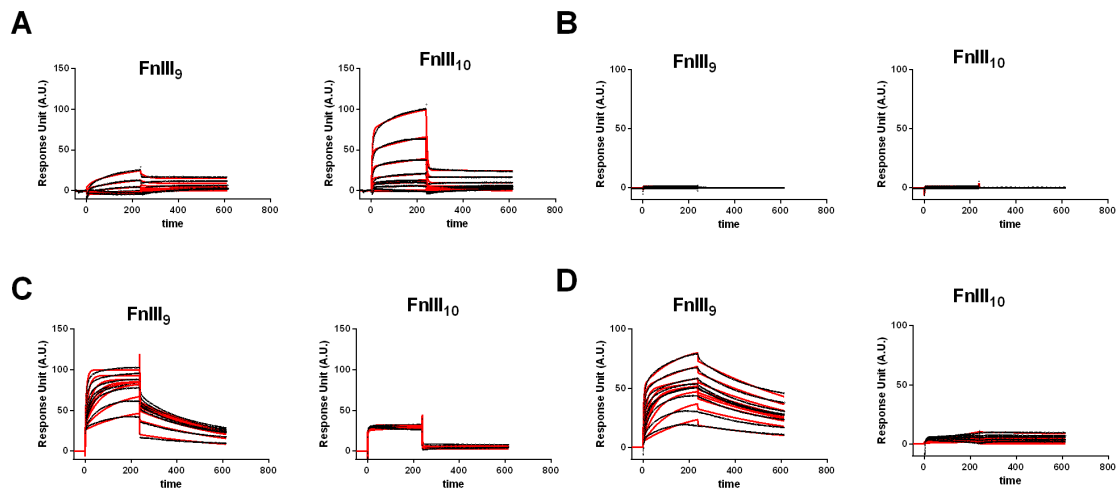

Figure 12. SPR sensograms of scFv antibodies on 9th or 10th Fn type III repeats. Simulations are shown in red, while experimental datasets are shown in black. Insets show residuals for simulations. A) A4 scFv antibody, **B)** F8 scFv antibody**, C)** H5 scFv antibody**, D)** G8 scFv antibody

In addition, we performed SPR analysis using Fn fragments containing either the 9th, or 10th type III repeats to further confirm and localize the binding epitopes for the selected scFv antibodies. Results suggested that the epitope for the A4 antibody binds within the 10th type III repeat (**Figure 12A**), H5 and G8 antibody binds within the 9th type III repeat (Figure 12C, D), and that the F8 antibody binds an epitope spanning both the 9th and 10th type III repeats (**Figure 12B**). Together, these results confirmed and were consistent with the observed results from the competitive ELISA assays (**Figure 10**).

Inhibition of cell attachment to Fn by scFv antibodies

Following phage display pannings and selection by ELISA assay, isolated and purified scFv antibodies were assessed in a functional assay in which the ability to modulate and inhibit cell attachment to Fn was tested. In an initial assay with a panel of 4 scFv antibodies, only the H5 clone was found to functionally inhibit attachment of human foreskin fibroblasts (HFF) to Fn. Incubation of HFF with H5 reduced attachment to Fn to

approximately 55% (**Figure 13**). Incubations of HFF cells with a function blocking antibody against β1 integrins reduced cell attachment to about 23%, and incubation of both β1 mAb and H5 antibody reduced cell attachment to 11%, though the difference was not statistically significant at a p-value of 0.05 (**Figure 13**).
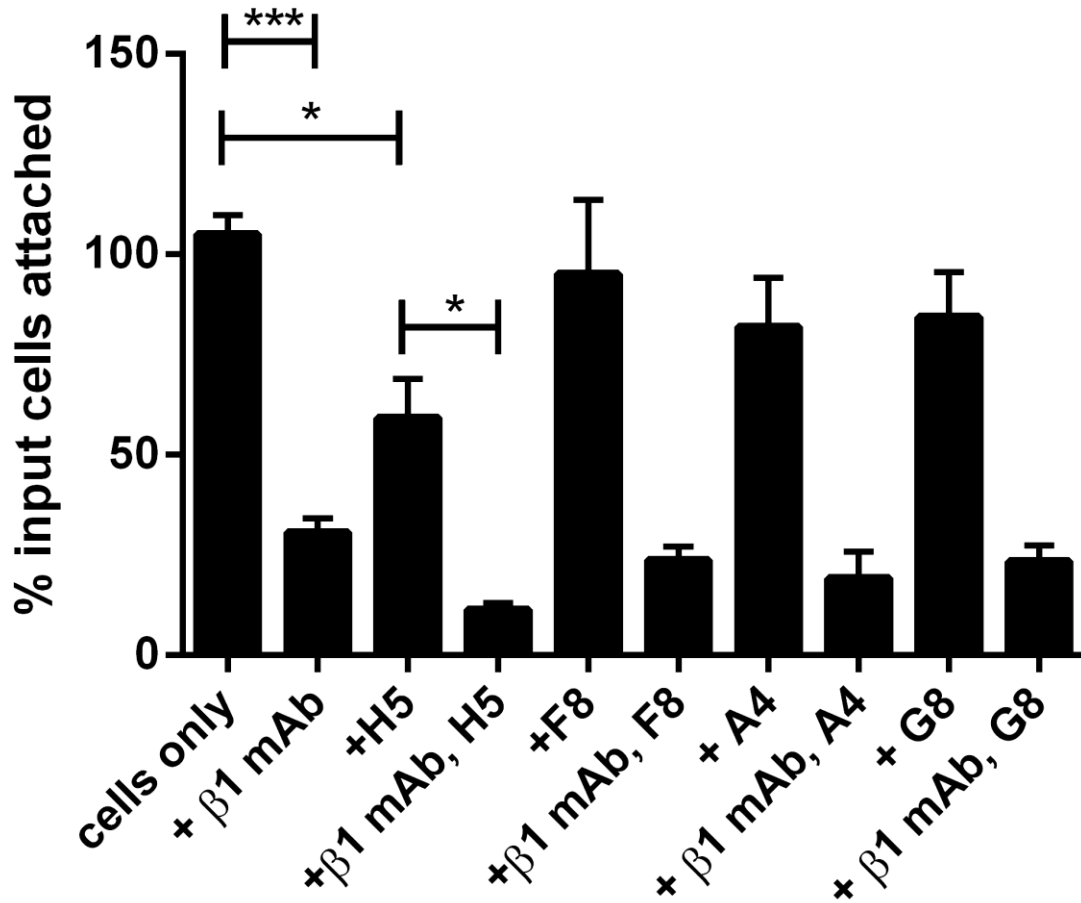
Figure 13. Modulation of HFF cell attachment to Fn by scFv antibodies. HFF cells (20,000 cells/well) were seeded on Fn (3 μg/mL) and assayed for attachment in the presence of H5, and an anti-integrin β1 antibody. At least six replicates were used per sample, error bars are SEM. (statistics performed using one way ANOVA with Tukey's post-test *, p<0.05, ***, P<0.001)

In another model cell line of H69 small cell carcinoma cells, which express primarily α3β1 (laminin, Fn) and small amounts of α6β1 integrins (laminin), we found that H5 scFv did not significantly affect H69 cell attachment, and that inhibition using a β1 integrin mAb did not significantly block cell attachment, suggesting that in these cells β1 integrins are not the primary integrin used to attach to Fn. (**Figure 14**).
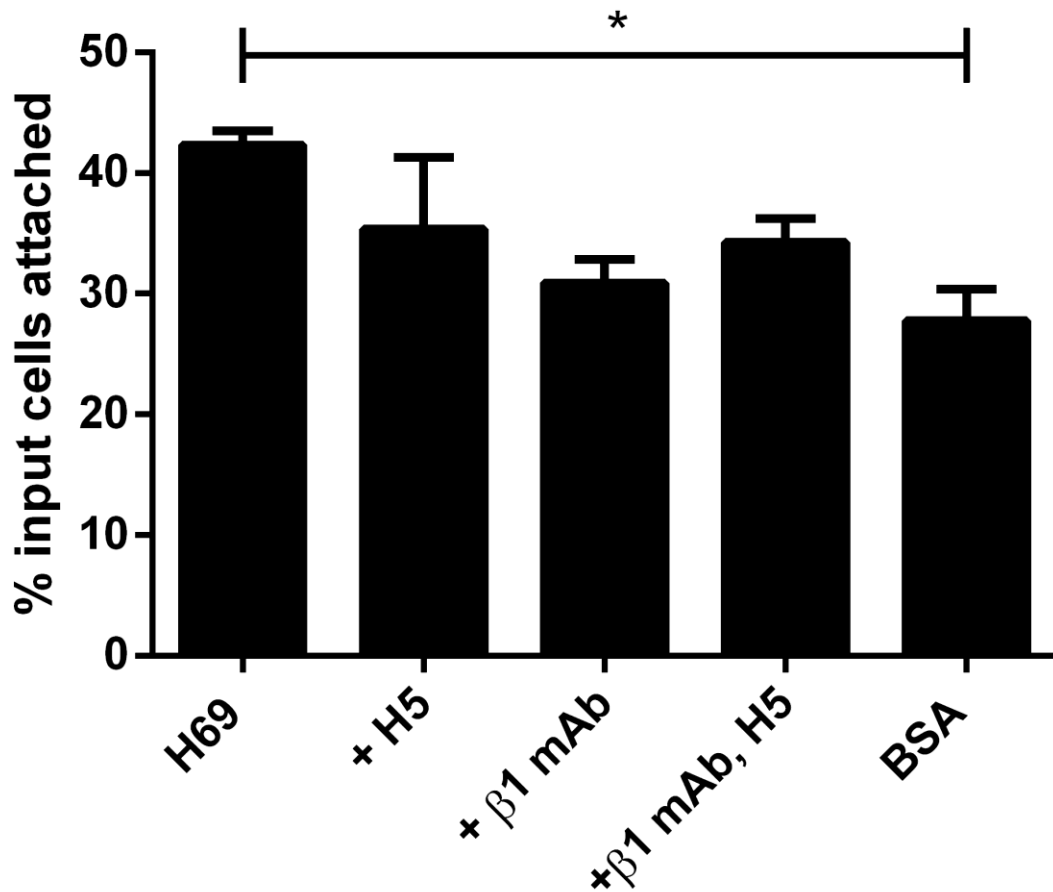
Figure 14. Inhibition of H69 cell attachment to Fn by H5 scFv and β1 mAb. H69 cells (250,000 cells/well) were seeded on Fn ($3\,\mu g/mL$) and assayed for attachment in the presence of H5, and an anti-integrin β1 antibody. At least six replicates were used per sample, error bars are SEM. (statistics performed using one way ANOVA with Tukey's post-test *, $p<0.05$)

The additive effects of both the β1 mAb and H5 scFv antibody in inhibition of cell attachment in human foreskin fibroblasts led us to hypothesize that H5 may be inhibiting another integrin receptor in addition to α5β1 integrins. The CHO-B2 cell line(96), a mutant variant of the popular Chinese hamster ovary (CHO) cells deficient in integrin α5β1, was chosen as an a model cell line to test this hypothesis.

CHO-B2-αvβ3 cells stably expressing integrin αvβ3 was created by transfection of the parent CHO-B2 cells with the appropriate plasmids and selection by flow cytometry. Assessing modulation of cell attachment by the H5 antibody in these cells revealed that
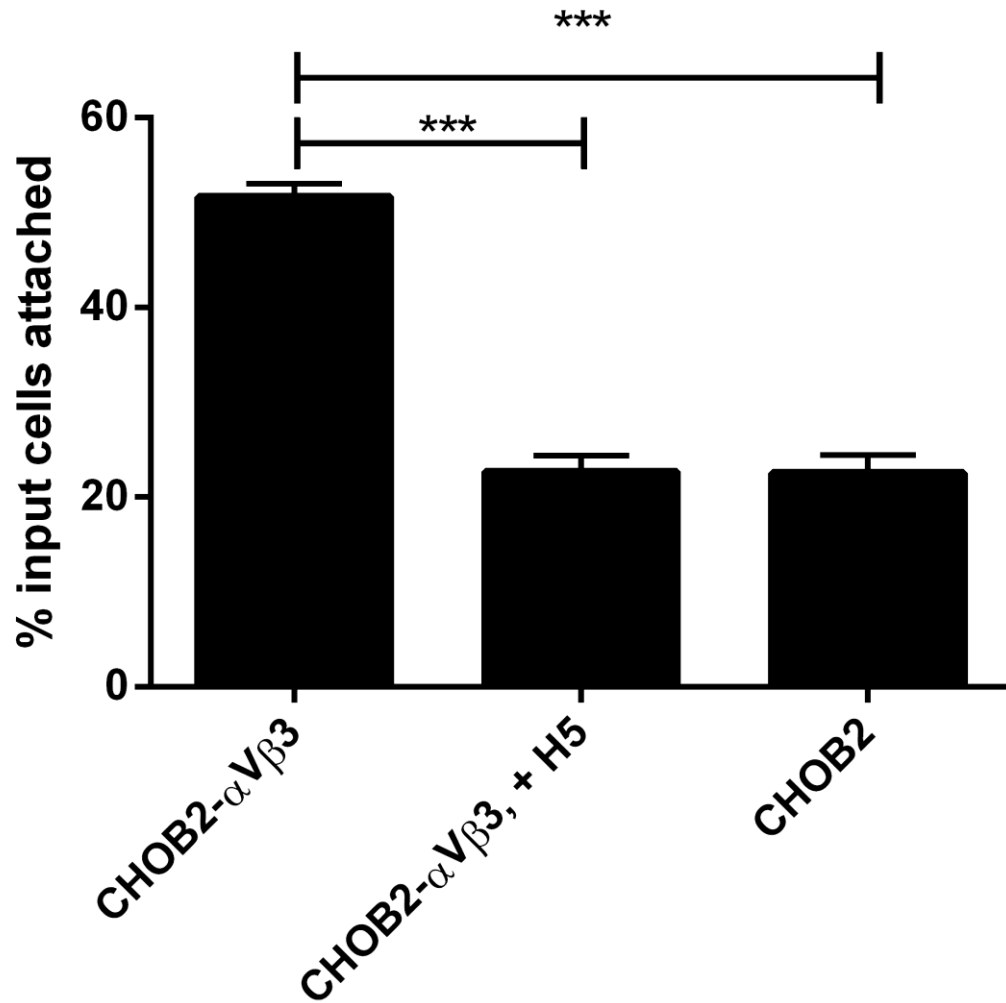
Figure 15. Modulation of CHO cell attachment to Fn by H5 scFv antibody. CHO cell variants (10,000 cells/well) were seeded on Fn (3 μg/mL) and assayed for attachment in the presence of H5, and an anti-integrin β1 antibody. At least six replicates were used per sample, error bars are SEM. (statistics performed using one way ANOVA with Tukey's post-test *, p<0.05, ***, p<0.001)

incubation of H5 antibody with the CHO-B2-αvβ3 cells completely blocked αvβ3 based cell attachment and reduced attachment levels to the same as the parent CHO-B2 cell line (**Figure 15**). To assess integrin α5β1 dominated attachment, we chose to use the K562 cell line (97). These cells were derived from a myelogenous leukemia origin, and do not express αV or β3 integrins (98, 99). The K562 cells only expressed α5β1 integrins, and also free

45

β1 integrins not associated with α5(100). Furthermore, these cells required a β1 activating antibody(101) for switching to high affinity integrin conformations. Incubation of H5 with the β1 activated K562 cells reduced cell attachment to Fn by approximately 30% (**Figure 16**), and this effect was abolished by blocking β1 integrins on the cell surface with an anti-β1 function blocking antibody. Together, these data suggested that the H5 antibody has selectivity in completely blocking integrin αvβ3-Fn interactions, and only moderately inhibited integrin α5β1-Fn interactions.

Discussion and Conclusions

We used engineered Fn fragments of the FnIII$_{9-10}$ region to model the molecular scale conformational spacing between the PHSRN and RGD sites with the Fn central cell binding domain. By performing phage display and selection using antibody libraries, we isolated scFv antibodies that demonstrated specificity in binding to the two model Fn fragments in an ELISA assay. Furthermore, the H5 antibody clone, which preferentially targeted to FnIII$_{9-4G-10}$, was found to be particular effective in blocking Fn-integrin αVβ3 interactions.

By epitope mapping studies, the binding epitope of the H5 antibody was localized to within the 9th Fn type III repeat. It was then surprising to find that H5 is effective for blocking binding of integrin αVβ3 to Fn, which binds to the RGD loop in the 10th Fn type III repeat. It is possible that binding of H5 to Fn could cause steric inhibition of the neighboring RGD site and thus prevent integrin αVβ3 binding. The finding that integrin α5β1 was still able partially bind to Fn in the presence of H5 could be attributed to its very high binding affinity (4nM) to Fn(102) when compared to binding affinity of αVβ3 to Fn(103) (affinity of αVβ3 to RGD: 1.3uM), or perhaps by differences in the conformational fit of the integrin headpieces when bound to Fn between integrin α5β1 versus αVβ3. More
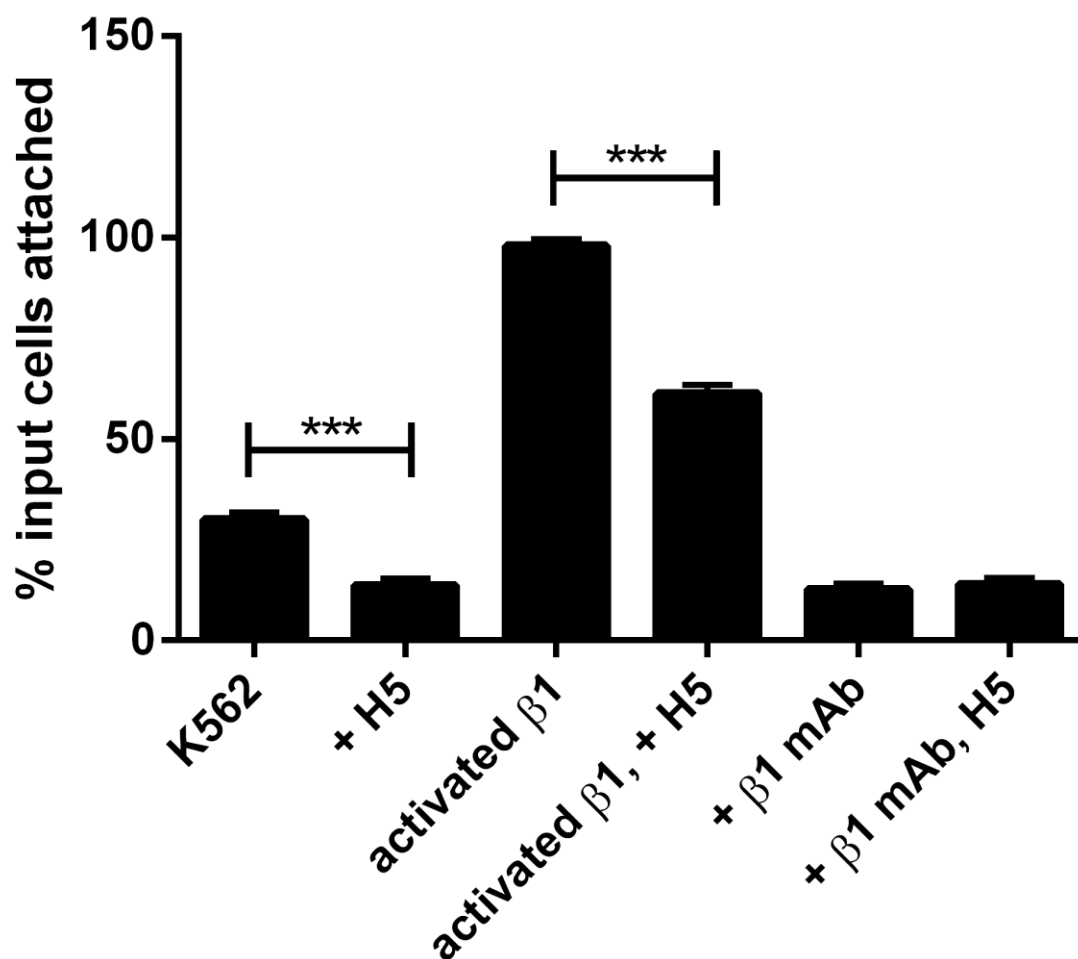
Figure 16. Modulation of K562 attachment to Fn by H5. K562 cells (50,000 cells/well) were seeded on Fn (3 μg/mL) and assayed for attachment in the presence of H5, and an anti-integrin β1 antibody. At least six replicates were used per sample, error bars are SEM. (statistics performed using one way ANOVA with Tukey's post-test ***, p<0.001)

likely, however, is that the insertion of the 4 glycine mutations results in a conformational tilt between the 9th and 10th Fn type III repeats, and studies have suggested that this interdomain tilt angle can regulate both αvβ3 and α5β1 integrin binding to the FnIII9-10 region(104).

The selectivity of the H5 antibody in completely inhibiting integrin αVβ3-Fn interactions, but only moderately inhibiting integrin α5β1-Fn interactions could theoretically allow for H5 to probe the hypothesized "integrin switch" *in vivo*. The utility

of our molecular probes developed against Fn for imaging of Fn was evaluated in a number

of models systems in the next chapter.

CHAPTER 5

CHARACTERIZATION OF ENGINEERED MOLECULAR PROBES FOR IMAGING OF FN *IN VITRO* AND *IN VIVO*

The mechanical properties of the ECM has emerged as a critical factor in regulating cell adhesion (105), migration (106), and fate decisions (107). Moreover, the mechanics of the ECM in native tissues and within tumors microenvironments may be important in controlling and/or promoting transformation and metastases (106, 108, 109). At the cellular scale, topographic features in the ECM that are sensitive to mechanical forces may regulate receptor recognition, resulting in reorganization of cytoskeletal structure and altering cell migration and invasion – a phenomenon that has been well studied *in vitro(44)*.

Despite these important roles of ECM mechanics in regulating cell and tissue function, there are currently no direct methods to image the ECM and provide information on the mechanics of the matrix in a non-invasive manner. Thus, opportunities exist to develop imaging probes that can be sensitive to mechanically-induced conformational changes to ECM proteins. Development of such ECM targeted probes would have applications for diagnosis and targeted therapeutics for tissue engineering and regenerative medicine, as well as enabling fundamental ECM mechanobiology research.

The phage-peptide probes and antibody probes we developed in Chapter 3 and 4 have demonstrated ability to discriminate between Fn of varying molecular conformations. In this chapter, we describe the methods we used to characterize these molecular probes for imaging of Fn in a number of model systems *in vitro*, as well as *in vivo* for minimally-invasive imaging of Fn within the lung parenchyma of mice in a bleomycin-induced model of pulmonary fibrosis.

Experimental Design

The probes were fluorescently labeled with Alexa Fluor dyes for immunofluorescence imaging, and probe staining was evaluated in three types of *in vitro* model systems of Fn. First, the probes were characterized for their staining on *in vitro* Fn fibers of varying strain, using the same method of Fn fiber generation as in Chapter 3. Semi-quantitative analysis of the captured fluorescence images were performed by calculating the ratio of the probe staining normalized to the Fn within the Fn fibers. Next, fibroblasts were used to assemble an ECM in culture, and fluorescent staining of the probes were evaluated and qualitatively assessed, with and without the use of pharmacologic cell contractility inhibitors. In addition, lung tissue sections were prepared from mouse lungs, and similar analysis of fluorescent staining using the phage-peptide probes and antibody probes were performed. Finally, the H5 antibody was labeled with a near-infrared fluorescent dye, and evaluated for ability to image Fn in a live animal (mouse) model of bleomycin induced pulmonary fibrosis.

Materials and Methods

Staining of labeled phage or scFv antibodies on cell assembled ECMs

Coverslips (10mm diameter) were sterilized in 70% ethanol and placed into wells of a 24-well plate, coverslips were coated with Fn (3 μg/mL) overnight at 4 ℃. Prior to cell seeding, the coverslip were washed 3X with PBS and mouse primary lung fibroblasts were seeded at 10,000cells/well. Cell were allowed to attach for 30mins at 37 ℃ in the incubator. After cells have attached, medium was then aspirated and replaced with medium containing 1 μg/mL Alexa Fluor 488 labeled Fn. Cells were then cultured for an additional 48 hours, at 37 ℃, 5% CO_2 in the incubator. In conditions with TGF-β, medium was then to medium containing 1 μg/mL Alexa Fluor 488 Fn, and 10ng/mL TGF-β 16 hours before fixing cells. In conditions where Y-27632 was added, 1 μM Y-27632 was added 1 hour before fixing

cells. Cells were washed 3X with PBS, and fixed in 4% formaldehyde for 20min. Cells were washed again 3X time PBS, with 5min per wash. Fixed cells were blocked for non-specific binding with 3% BSA in PBS, overnight at 4 ℃. Labeled phage (10^{12} CFU/mL) or scFv antibodies were incubated for 1 hour, at room temperature, washed 3X in PBST, and coverslips were transferred to glass slides, mounted in Prolong gold antifade reagent (Invitrogen, Life Technologies, Grand Island, NY), and sealed with a top coverslip and nail polish.

Mouse bleomycin model of IPF

C57/BL6 mice (female, 6-8 weeks age) were anesthetized using a ketamine/xylazine/acepromazine cocktail, and injected with Bleomycin sulfate(Enzo life science, Farmingdale, NY) at a dose of 3.2U/kg through intratracheal injections. Injection volumes were 50 μL of solution, with additional 10 μL of air bolus. Immediately after injection, mice were placed on heating pads and allowed to recover from anesthesia before placed back into housing.
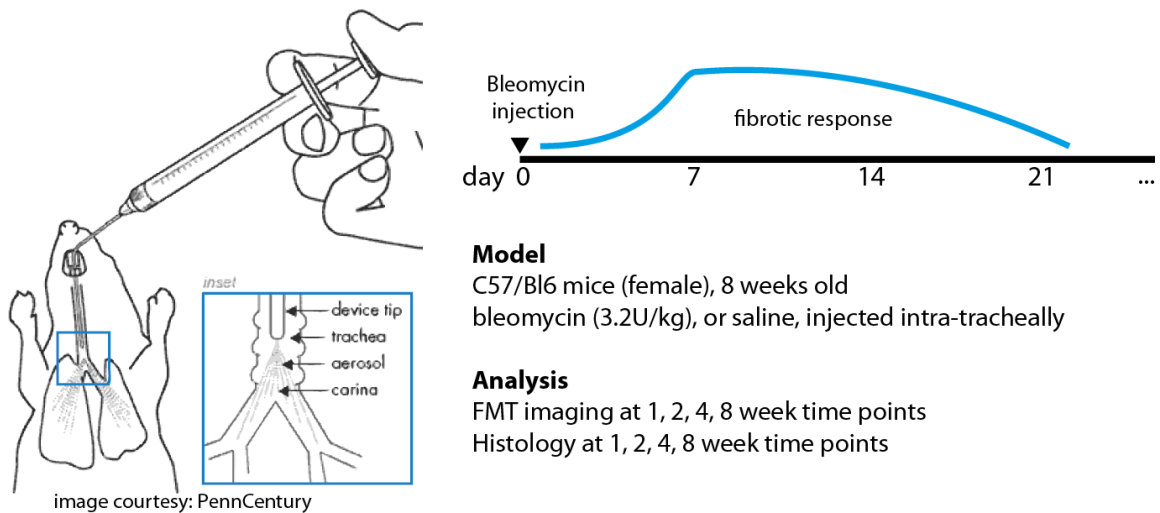

image courtesy: PennCentury

Figure 17. Bleomycin model of mouse pulmonary fibrosis. Bleomycin (3.2U/kg) was injected intra-tracheally into C57/Bl6 female mice of approximately 8 weeks old. This mouse model of fibrosis results in rapid fibrotic response approximately 1 week after bleomycin induction. After approximately 1 month, fibrosis resolves spontaneously..

Lung isolation and tissue sectioning

At set time points after bleomycin injections, mice were euthanized and the lungs were collected. Mice were anesthetized by injections with ketamine/xylazine/acepromazine cocktail (50 μL/animal), and toe pinch was used as a metric to make sure the mice were not responsive. Mice were taped down by the limbs and cleaned by wiping with an ethanol wipe. Using a scissor, a small cut was made near the top of the chest cavity, and the trachea was isolated using tweezers. A nylon string was fed through below the trachea, and a small cut was made in the trachea near the top, and a trachea tube was inserted into the trachea. PBS (500 μL) was injected slowly through the trachea tube to lavage the lung, aspirate and repeat. The nylon string was tied off to close the trachea. A patch of skin was cut and the internal organs of the mouse was exposed: the renal arteries were cut to exsanguinate the mouse. A gauze pad was used to soak up the blood. A cut was made vertically, all the way up to trachea tube and through the rib cage, cut slightly off center to avoid cutting the trachea. Both sides of the rib cage was clipped with hemostat and pried apart, exposing the lungs and heart. The heart was pulled down with tweezers, and a small cut was made in the right ventricle in the orientation aligned with the pulmonary valve. A blunted 30 gauge needle and syringe was inserted into the right ventricle, with the aim of insertion into the pulmonary valve, and 1mL of PBS was injected to perfuse the lungs. The lungs and heart were removed from the rib cage by careful cutting away from the chest cavity by pulling up on the nylon string and cutting away the surround tissue. The lungs and heart were placed on a ringstand with tubing, and fixed with 4% paraformaldehyde in PBS by gravity. The fixed tissue was stored in 4% paraformaldehyde at 4 ℃ until sample processing and tissue slicing.

Cryo-section preparations and immunofluorescence staining of lung samples

Fixed lungs were placed into 20% sucrose overnight at 4 ℃. Samples were placed into cryomolds with O.C.T. compound (Electron Microscopy Sciences, Hatfield, PA).

Using liquid N_2, 1-methylbutane was frozen solid in a plastic container, and the cryomolds were frozen by placing into direct contact with the frozen 1-methylbutane and placed into a -20 ℃ freezer overnight. Next day, frozen sections (10 μm thickness) were prepared on a Cryostar NX70 cryostat (Thermo Scientific, Pittsburg, PA) and transferred to Plus-glass slides. Slides were stored at -80 ℃.

Lung sections were blocked overnight at 4 ℃ with 3% BSA in PBS. All staining was performed by sandwiching the staining solution (150 μL per slide) between the slide and a parafilm surface. Primary scFv antibody (H5) was incubated at 10 μg/mL for 1 hour at room temperature. Slides were washed in PBST, 3 times for 5 minutes each. Anti-myc antibody was incubated on slides at 1:1000 dilution for 1 hour at room temperature. Slides were washed in PBST, 3 times for 5 minutes each. Secondary antibody (Alexa 546 goat anti-mouse, 1:2000 dilution) was incubated on slides for 1 hour at room temperature, followed by washing in PBST, 3 times for 5 minutes each. Slides were mounted in Prolong Gold antifade reagent, sealed with nail polish, and stored at -20 ℃ until imaged.

IVIS imaging with scFv antibodies

Mice (C57/BL6, female, 8 weeks old, Charles River Laboratories, Wilmington, MA) were anesthetized using Ketamine/xylazine/acepromazine cocktail, and hair on chest area was removed by shaving and Nair® hair remover. Alexa Fluor 750 labeled scFv antibodies were injected into the lateral tail vein (50 μg per injection). Mice were imaged on IVIS Lumina® imaging system (Xenogen) using the following parameters: excitation: 745nm, emission, 780nm, exposure 10 seconds, medium binning, field stop: 2, stage position C. Images were acquired with fluorescence efficiencies and acquired at time points up to 40mins following injection.
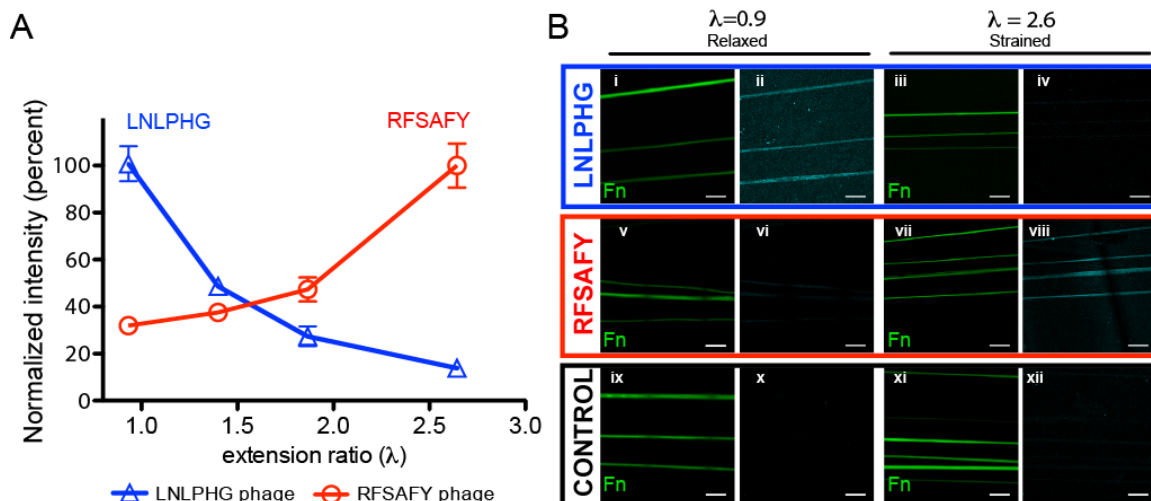
FMT imaging with scFv antibodies

Figure 18. Staining of specific phage clones correlate with Fn fiber strain. Phage clones displaying the LNLPHG and RFSAFY peptides were labeled with AlexaFluor 633 SE and incubated on Fn fibers (1 X 1011 phage per sample). **A)** Staining of labeled LNLPHG phage decreases with increasing fiber strain, and staining of RFSAFY phage increases with increasing fiber strain. **B)** i-xii) Fluorescence images of labeled phage clones on Fn fibers under varying strain. LNLPHG phage binding to relaxed ($\lambda = 0.93$) (i,ii) and strained ($\lambda=2.64$) Fn fibers (iii,iv). RFSAFY phage binding to relaxed ($\lambda = 0.93$)(v,vi) and strained ($\lambda=2.64$)Fn fibers (vii,viii). Labeled control phage show minimal binding (ix-xii). Error bars are SD. All images acquired with 63X oil immersion objective, scale bar is 20 μm.

Mice (C57/BL6, female) were anesthetized by isofluorane inhalation, and hair on chest and back was removed by shaving and Nair® hair remover. Alexa Fluor 750 labeled scFv antibodies were injected into the lateral tail vein (50 μg per injection). Mice were imaged on FMT 2000 fluorescence tomography system (Perkin Elmer). Scans were acquired at pre-injection, and at time points (5min, 10min, 15min, 20min, 30min, 40min) post-injection to monitoring accumulation and clearance of the antibody to and from the lungs.

Results

Immunofluorescence staining of phage probes on Fn in model systems

To directly image phage probe targeting to Fn fibers under varying strain, we used a semi-quantitative approach using fluorescently labeled phage and normalization to fluorescently labeled Fn within the fibers. Phage binding to Fn fibers deposited on micropatterned PDMS substrates was assessed on increasingly strained Fn fibers ($\lambda = 0.9$ to 2.6; **Figure 18a**). Fluorescence intensity of the Fn fiber at 633nm (AF633-labeled phage)
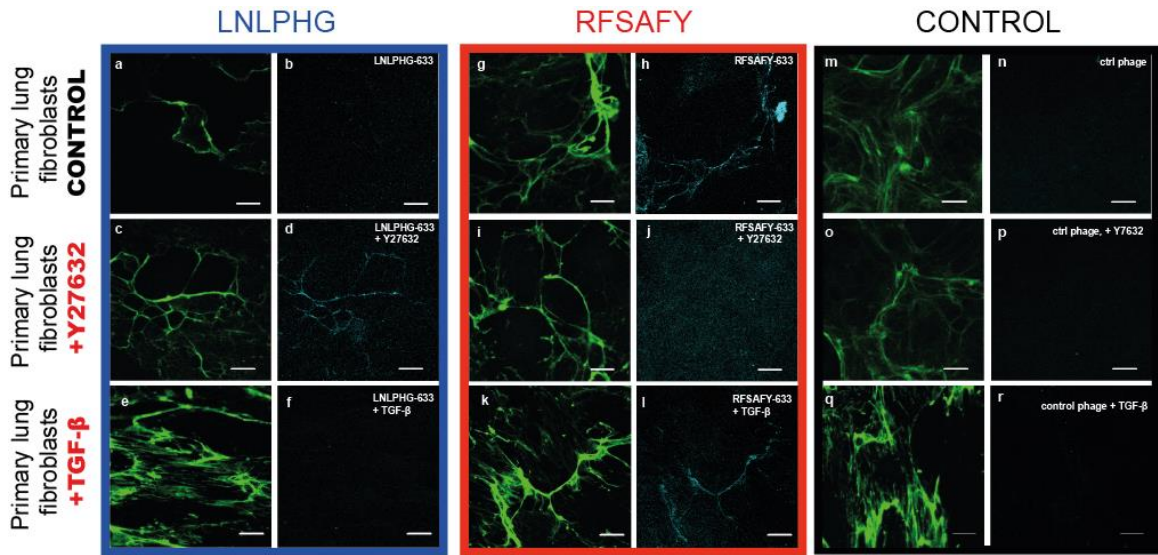
Figure 19. Staining of specific phage clones on cell assembled ECM. Phage clones displaying the LNLPHG and RFSAFY peptide motifs were labeled with Alexa Fluor 633 SE and incubated on ECM assembled by primary lung fibroblasts (1 X 1011 phage per sample). Experiments performed with and without the ROCK inhibitor Y27632 to relax the matrix top left, Staining of LNLPHG phage observed primarily on large diameter fibers, and increased after matrix relaxation top right, Staining of RFSAFY phage observed primarily on large diameter fibers. Staining is minimal after matrix relaxation by Y27632. Bottom, staining of a labeled control phage. All images acquired with 63X oil immersion objective, scale bar is 20 μm.

was normalized to the amount of Fn in the fiber (5% AF488-labeled tracer Fn). The Fn fibers labeled with the LNLPHG clone showed a nonlinear but reproducible decrease in fluorescence signal as strain increased (**Figure 18bi-iv**). Conversely, as expected, Fn fibers labeled with the RFSAFY clone showed an increased signal with fiber strain (**Figure 18b, v-viii**). The intensity of Fn fiber labeled with a control (random) phage was negligible (non-detectable) at all strains tested (**Figure 18bix-xii**). Targeting selectivity for the LNLPHG clone, defined as [signal at λ=0.9]/[signal at λ=2.6], was determined to be 7.29. Targeting selectivity for the RFSAFY clone, defined as [signal at λ=2.6]/[signal at λ=0.9] was determined to be 3.13.

As a result of combining phage display screening with control over Fn fiber strain, we discovered relatively simple probes that are capable of detecting varying states of strain in Fn fibers. Importantly, our approach does not require the Fn to be chemically labeled (a requirement and limitation of the FRET method). Such probes enable the interrogation of *native* Fn ECM, allowing us to address a critical gap in the determination of the relevance
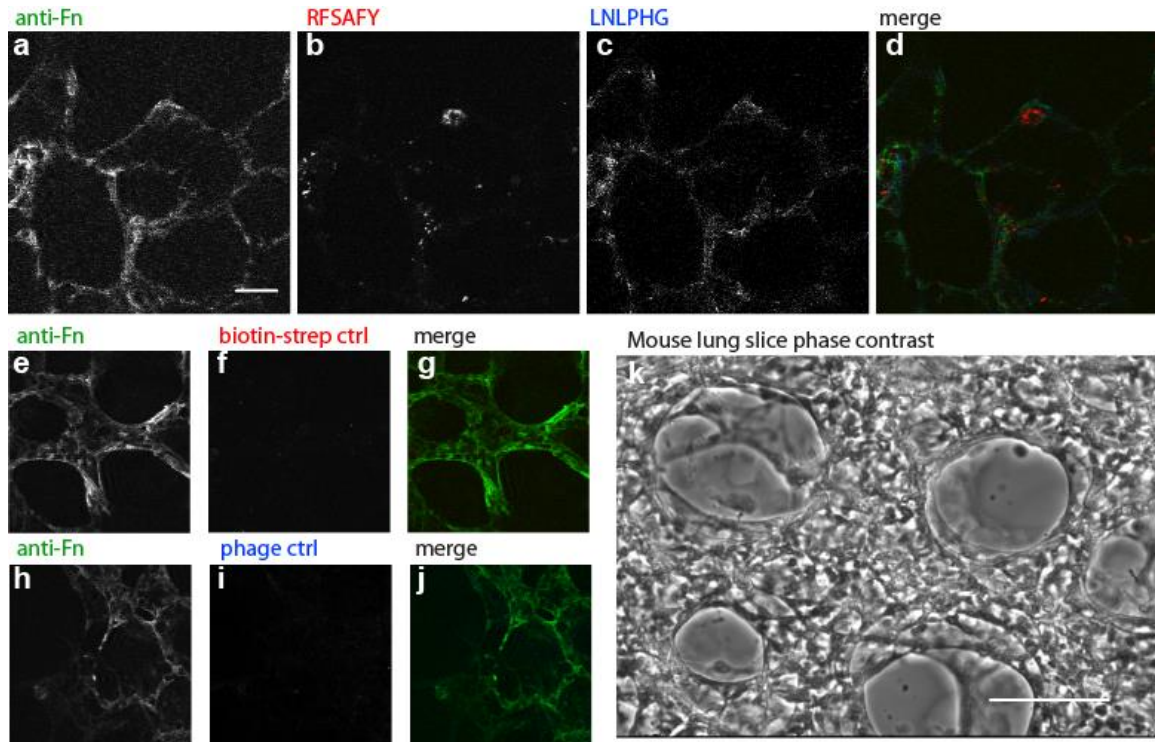
Figure 20: Staining of specific phage clones on prepared living lung slices. a-d) co-staining of multiple Fn targeting probes on a representative mouse lung slice. **(a)** staining of polyclonal anti-mouse Fn antibody, **(b)** staining of labeled RFSAFY phage, detected with AF633.**e-g)** staining of labeled random phage clone detected with AF546. **h-j)** staining of labeled random phage clone detected with AF633. **k)** representative phase micrograph of a prepared living lung slice. Images in panel a-j acquired with 63X oil immersion objective. Scalebars, **a-j)** 20μm, **k)** 100μm.

of force-mediated Fn structural modifications. As a first demonstration of this principle, we used our phage clones to discriminate fibers within native cell-assembled Fn. Fn was assembled by contractile primary lung fibroblasts cultured in the presence of tracer Fn (AF488-labeled; **Figure 19**). Labeled (AF633) phage clones were detectable primarily within larger diameter fibers and their binding was highly correlated with cell-mediated tensional strain of the Fn ECM as demonstrated by the addition of the cellular contraction inhibitor, Rho-kinase inhibitor Y-27632. Specifically, staining of native, cell-derived Fn fibers with the LNLPHG phage was non-detectable at steady state and increased upon addition of Y-27632, which results in a more relaxed (lower strain) Fn ECM (**Figure 19 a,b,c,d**), and decreased upon stimulation of cell contraction with TGF-β(**Figure 19e,f).** Concomitantly, staining of native, cell-derived Fn fibers with the RFSAFY phage clone
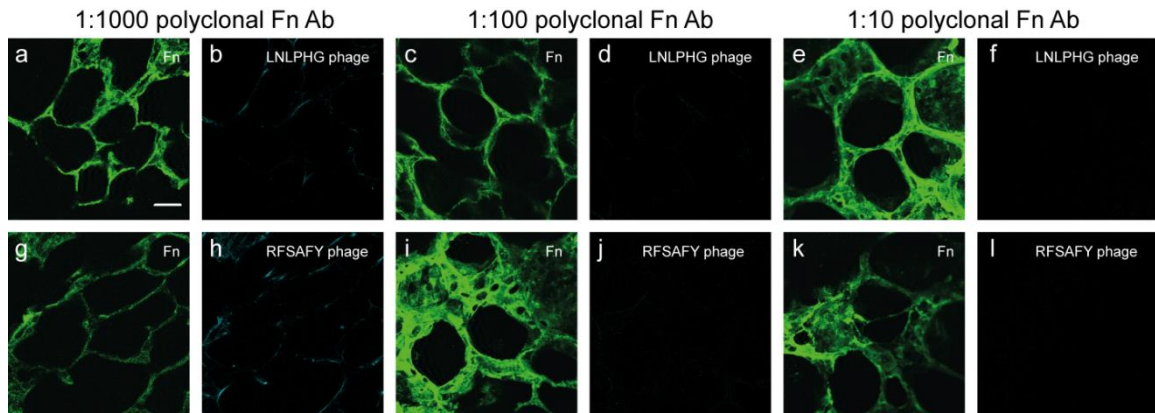
Figure 21. Competitive binding of polyclonal anti-Fn antibody displaces binding of phage probes on tissue lung slices. A polyclonal anti-Fn antibody (1mg/mL) was titrated in along with the LNLPHG phage and RFSAFY phage at 1:1000 (a, b, g, h), 1:100 (c, d, i, j), and 1:10 (e, f, k, l) dilutions. Images acquired with 63X oil immersion objective. Scale bar is 20 μm.

demonstrated robust staining at steady state and significantly decreased upon Y-27632 addition (**Figure 19 g,h,i,j**), but was not changed with TGF-β stimulation (**Figure 19 k,l**). Staining of Fn fibers with a labeled control phage was non-detectable with or without Y-27632 or TGF-β treatment further demonstrating the specificity of the peptide-strain specific antigen interaction (**Figure 19 m-r**).

As a further proof of concept demonstration, mouse living lung slices were prepared (**Figure 20k**), and staining of our phage clones were evaluated in concert with a commercially available anti-Fn antibody **(Figure 20).**

Qualitatively, our phage probes were able to delineate Fn matrix morphology, similar to the staining patterns of the Fn-antibody (**Figure 20 a-d**). Interestingly, the staining of RFSAFY phage **(Figure 20b)** appeared more punctuate and appeared to be more spatially heterogeneous when compare to the staining of Fn antibody **(Figure 20a).** Additionally, labeled control phages displayed no detectable binding regardless of labeling species (**Figure 20 e-j**). In addition, co-incubation with an excess of a polyclonal anti-Fn antibody were able to inhibit binding of both phage probes **(Figure 21).** Similar results were obtained using a molecular probe approach **(Figure 22)**. Specifically, quantum dot-peptide conjugated probes displaying either LNLPHG or RFSAFY peptides similarly co-

stained with a polyclonal Fn antibody **(Figure 22, a-f)**. Further, no staining was observed

for the scrambled versions of both molecular probes **(Figure 22, g-j)**.
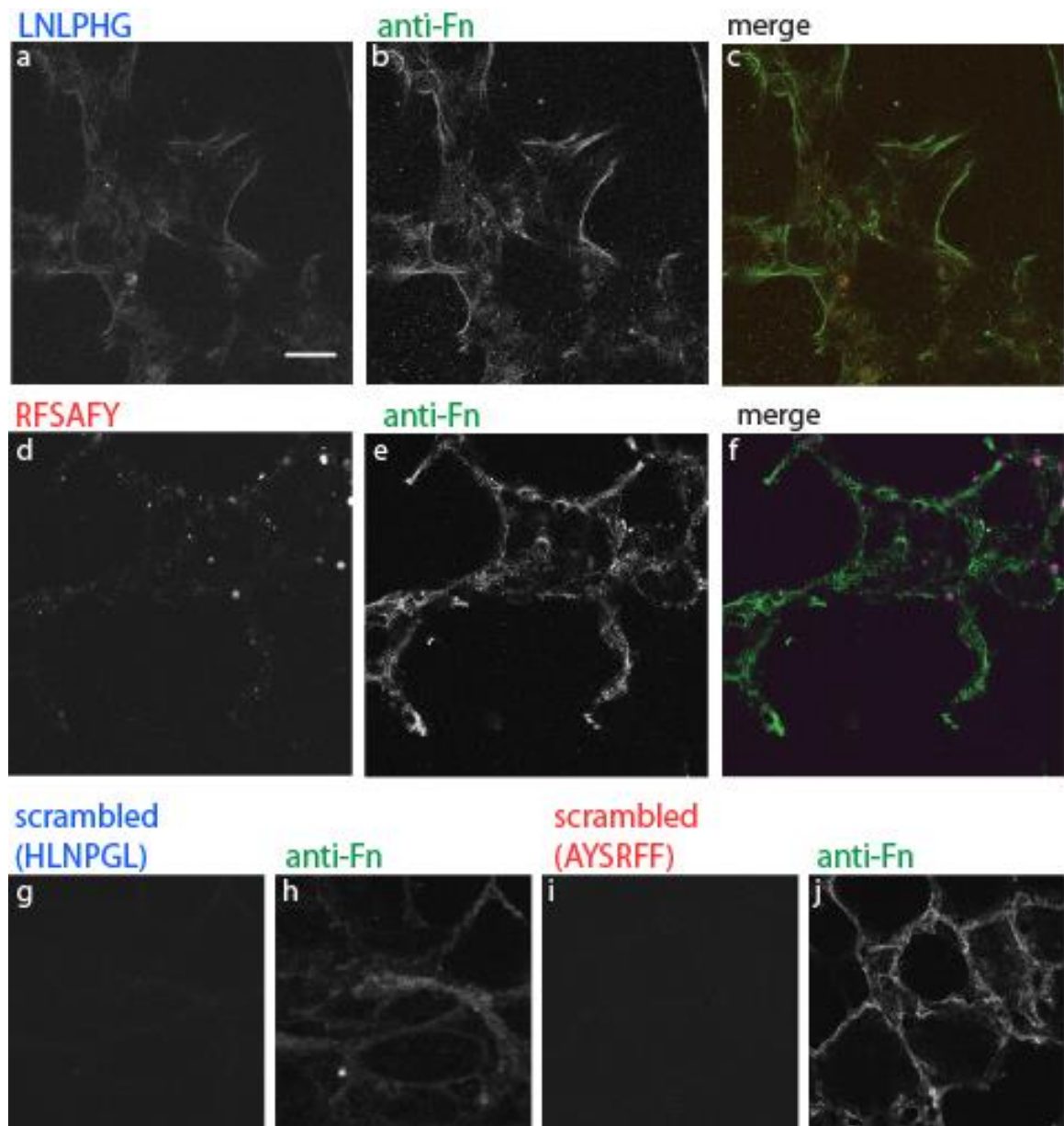
Figure 22. Staining of labeled peptides on prepared living lung slices. Peptides corresponding displayed peptides on phage-based probes were generated by solid phase synthesis and contain a C-terminal cysteine for chemical ligation (peptides: LNLPHGGGC, RFSAFYGGC, HLNPGLGGC, AYSRFFGGC). Peptides were conjugated to Qdot© and purified per manufacturer's instructions (Molecular Probes). **(a-c)** staining of LNLPHG-probe and co-staining with polyclonal anti-Fn antibody **(d-f)** staining of RFSAFY-probe and co-staining with polyclonal anti-Fn antibody. **g-h)** staining of scrambled LNLPHG probe. **i-j)** staining of scrambled RFSAFY probe. All images acquired with 63X oil immersion objective. Scale bar is 20 μm.

Immunofluorescence staining of scFv antibodies of Fn in model systems

On in vitro Fn fibers
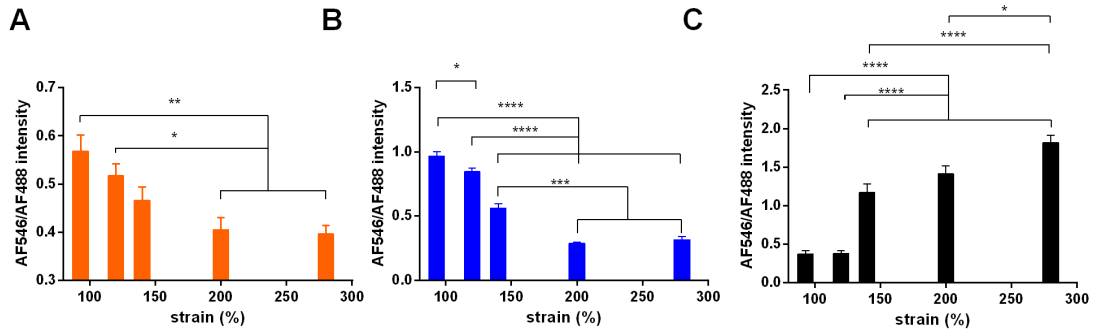
Figure 23. Immunofluorescence staining of scFv antibodies correlate with Fn fiber strain. Fn fibers were deposited on PDMS membranes and strained to defined amounts. At least 6 fibers were analyzed per sample. Error bars are SEM. Statistics performed with one-way ANOVA, with Tukey's post-test, (*, $p<0.05$, **, $p<0.01$, ***, $p<0.001$, ****, $p<0.0001$.)

Purified scFv antibodies were assessed for their utility in immunofluorescence staining of *in vitro* deposited Fn fibers (**Figure 23**). Specifically, staining of the A4 scFv (**Figure 23, a**) and F8 scFv (**Figure 23, b**) both showed a negative correlation with increasing strain in Fn fibers, while the H5 scFv antibody (**Figure 23, c**) showed increased staining with increased Fn fiber strain, with robust staining along Fn fibers at fiber strains above 150% (**Figure 24**).
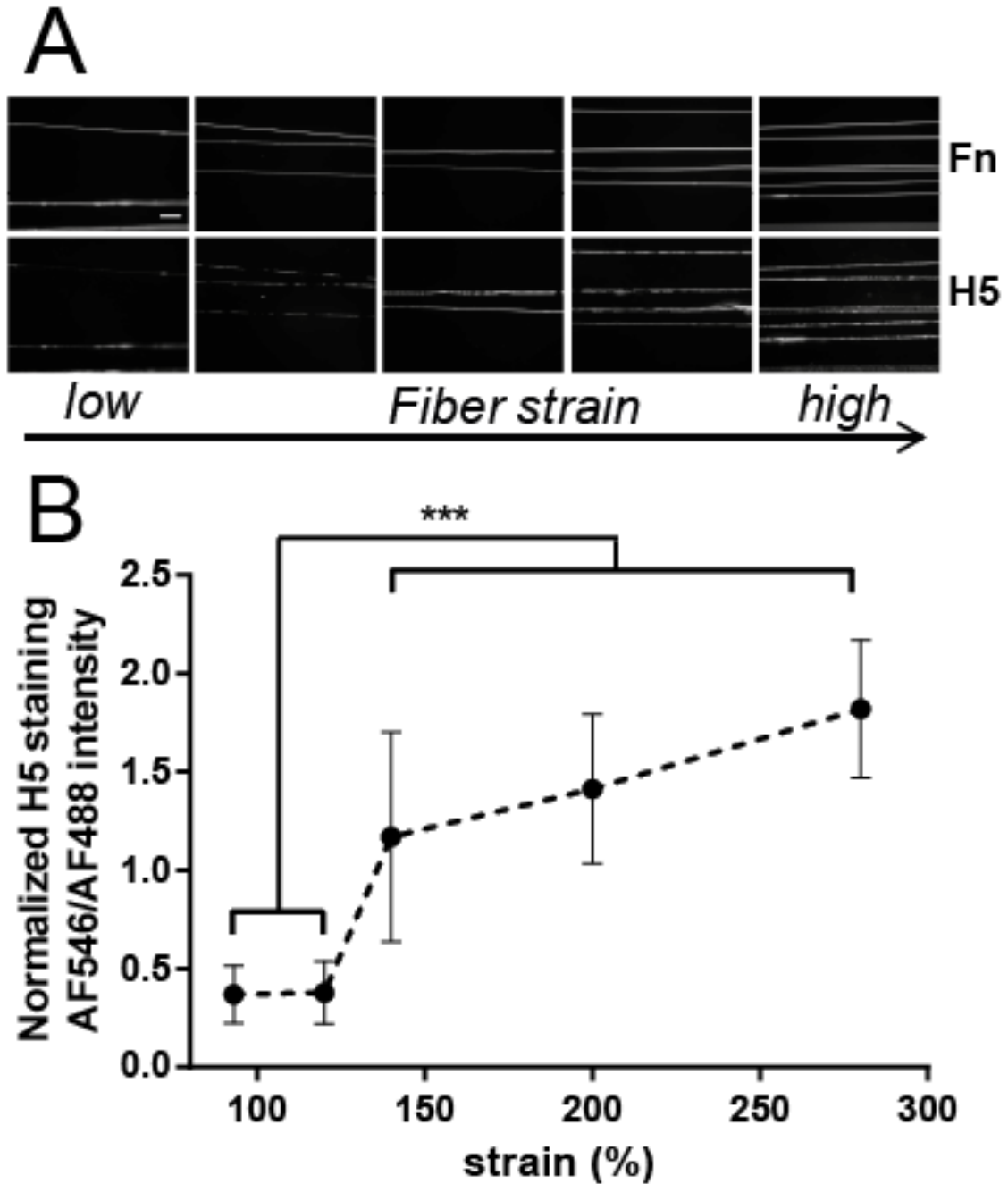
Figure 24. Mechano-sensitive staining of H5 antibody on Fn fibers in vitro. Fn fibers were deposited on PDMS membranes and strained to defined amounts. At least 6 fibers were analyzed per sample. Error bars are SEM. Statistics performed with one-way ANOVA, with Tukey's post-test, (*, $p < 0.05$, **, $p < 0.01$, ***, $p < 0.001$, ****, $p < 0.0001$.)
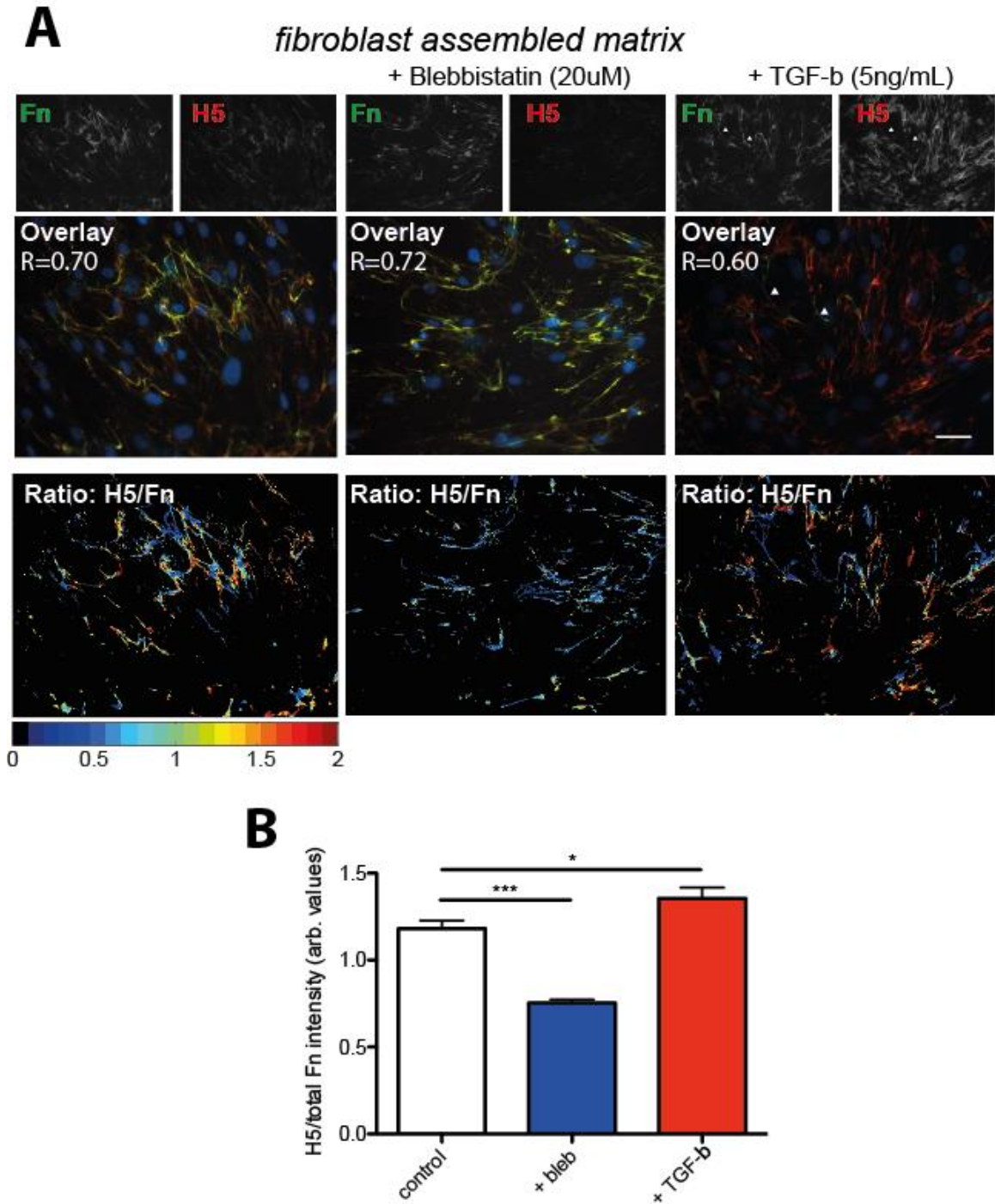
Figure 25. Immunofluorescence staining of H5 on cell assembled ECMs. A) Primary mouse lung fibroblasts were cultured to assemble an ECM containing Fn. Total Fn was visualized by incorporation of Alexa 488 Fn into the Fn matrix. Fn staining is shown in green. Pierson correlation coefficient (R) is shown as indicated. B) Quantitation of ratiometric images from panel A. Scalebar is 20 μm.

61

In ECMs assembled by cultured mouse primary fibroblasts, the H5 antibody can be used to fluorescently image Fn within this matrix (**Figure 25**). Notably, the staining of the H5 antibody do not completely co-localize with fluorescently labeled Fn assembled into the matrix (Pierson correlation coefficient R = 0.70) – suggesting that H5 is likely discriminating between Fn molecules of different conformations within the matrix.

Blebbistatin (20 μM) was added to cultures to inhibit cell contractility and relax the matrix, in which case a slight reduction in overall H5 staining intensity was observed. In cultures where TGF-β (5ng/mL) was added to stimulate cell contractility and induce fibroblasts to exert greater forces on their ECMs, the H5 staining patterns were markedly pronounced when overlaid with the Fn signal, and appears to be able to delineate specific regions along distinct Fn fibers within the matrix (arrowheads), as well as discriminate among Fn fibers. Moreover, quantitative ratiometric image analysis (dividing the H5 signal over the Fn signal) revealed spatially distinct patterns of H5 antibody staining within the ECM, and overall H5 targeting to Fn (as measured by global H5/Fn intensity) was dependent on cell contractile phenotype. The TGF-β cultures stained most prominently for H5, followed by the untreated cells, and the blebbistatin treated cells with the least amount of H5 staining (**Figure 25B**).

On ex vivo mouse lung tissue slices from normal and fibrotic mice

Frozen tissue sections were generated from lungs of normal and bleomycin-induced fibrotic mice, and staining of H5 was assessed on these samples (**Figure 26**). By immunofluorescence, the H5 staining pattern localized to fibrillar Fn within the ECM (Pierson correlation coefficient R = 0.86, normal, and R = 0.73, fibrotic). Furthermore, ratiometric image analysis revealed that the H5 staining patterns within these lung samples were spatially distinct (assayed using a polyclonal anti-Fn antibody) – again suggesting distinct conformational states of Fn within the matrix. Furthermore, the staining of a labeled control scFv antibody was minimal on both fibroblast assembled ECMs and frozen tissue sections of both normal and fibrosis mouse lungs (**Figure 27**).
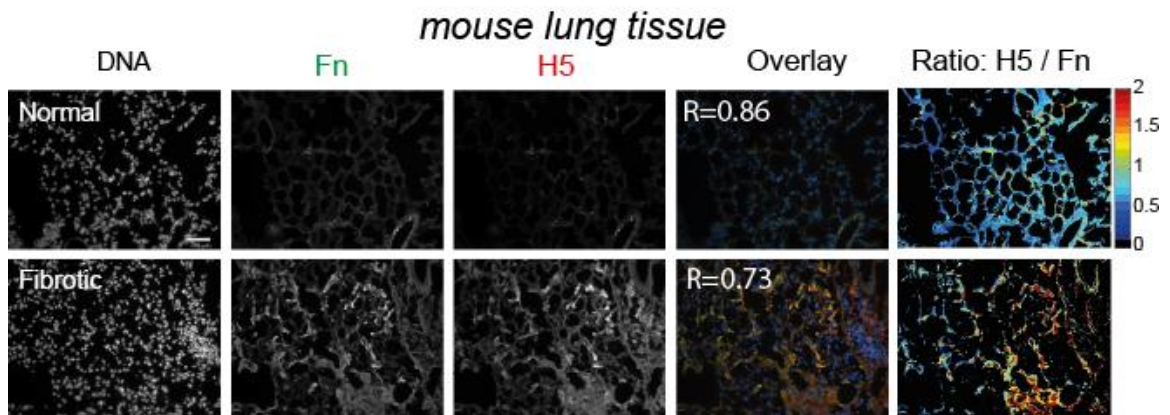
Figure 26. Staining of H5 on lung tissue samples from normal and fibrotic mice. Immunofluorescence staining of H5 on frozen lung tissue slices. In merged image, DNA is shown in blue, Fn is shown in green, and H5 is shown in red. Pierson correlation coefficient (R) is shown as indicated. Scalebar is 20 μm.

Fibroblast assembled ECM

| DNA | Fn | neg ctrl Ab | Merge |
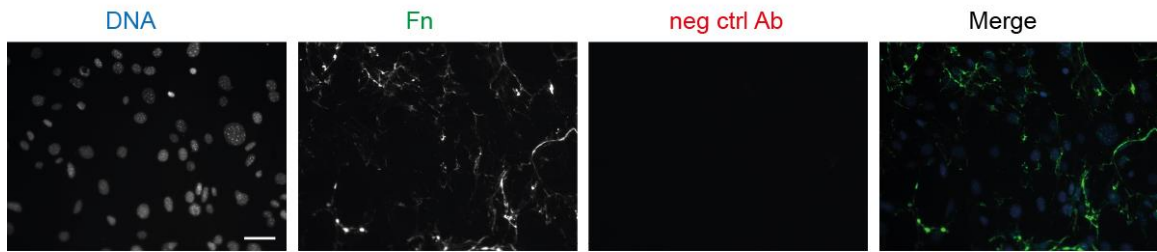
Lung tissue sections
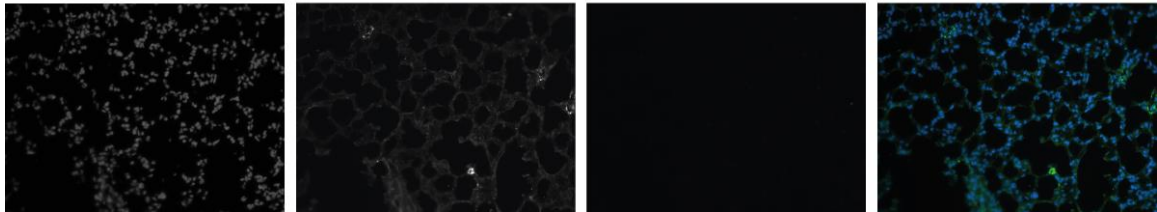
Figure 27. Minimal staining of a negative control scFv antibody. A negative control antibody was produced from a random clone from the parental Tomlinson I library, and staining experiments were performed on fibroblast assembled ECM (top) and on frozen mouse lung tissue sections (bottom). Scale bar is 20 µm.

Minimally invasive imaging of Fn using H5 in live animals

Purified H5 antibody was labeled with Alexa Fluor 750 fluorescent dye and used to image the Fn within the lung interstitium of anesthetized mice. Labeled H5 antibody was introduced by tail vein injection, and accumulation in the lung interstitium was monitored using small animal bioimaging systems. In preliminary experiments using a Xenogen Lumina® IVIS system, the fluorescence of the Alexa 750 labeled H5 antibody was monitored following tail vein injection into both normal and bleomycin induced fibrotic mice. Fluorescence signal appeared to accumulate in the lungs to above background levels approximately 5 minutes post-injection (**Figure 28**), and all fluorescence was undetectable at approximately 1 hour post-injection, usually following urination by the animal.
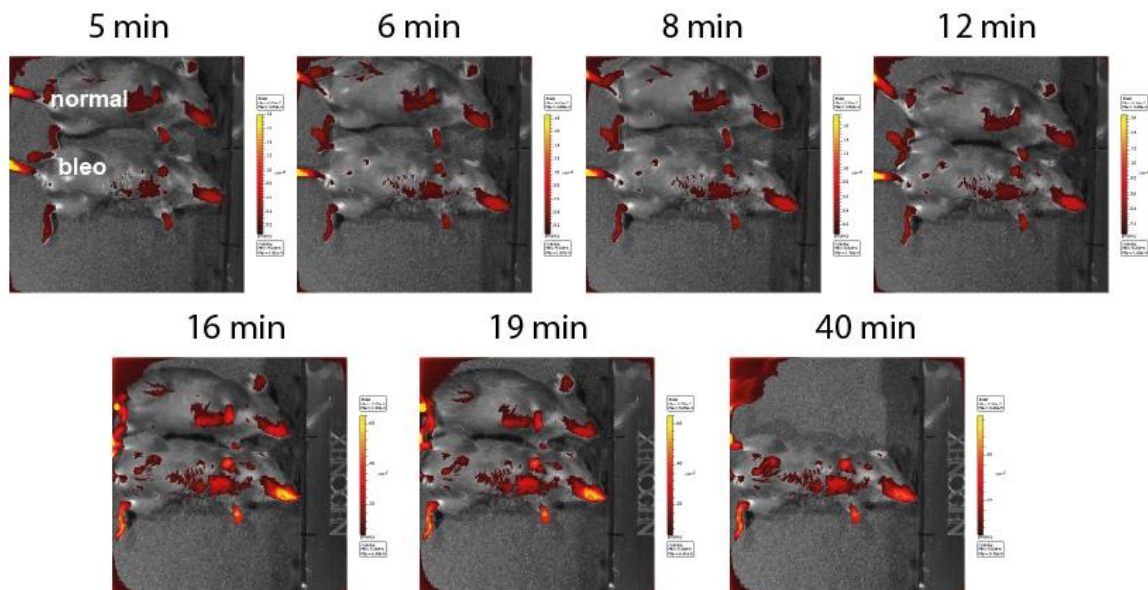
Figure 28. IVIS imaging of normal and fibrotic mice by tail vein injection. Alexa 750 labeled H5 was injected via tail vein and imaged at indicated time points post-injection.

Fluorescence intensity was qualitatively similar between normal and fibrotic mice. However, using a much more sensitive 3D fluorescence molecular tomography (FMT) imaging system, differences in accumulation of fluorescently labeled H5 was distinctly

discernible between normal and fibrotic mice (**Figure 29**). H5 accumulated in both the left and right lungs, and maximal difference in accumulation between normal and fibrotic mice occurred at 10mins following injection, subsequent quantitative analysis showed a difference in total fluorescence of 84.99 (normal, arbitrary units) vs. 745.75 (fibrotic, arbitrary units)
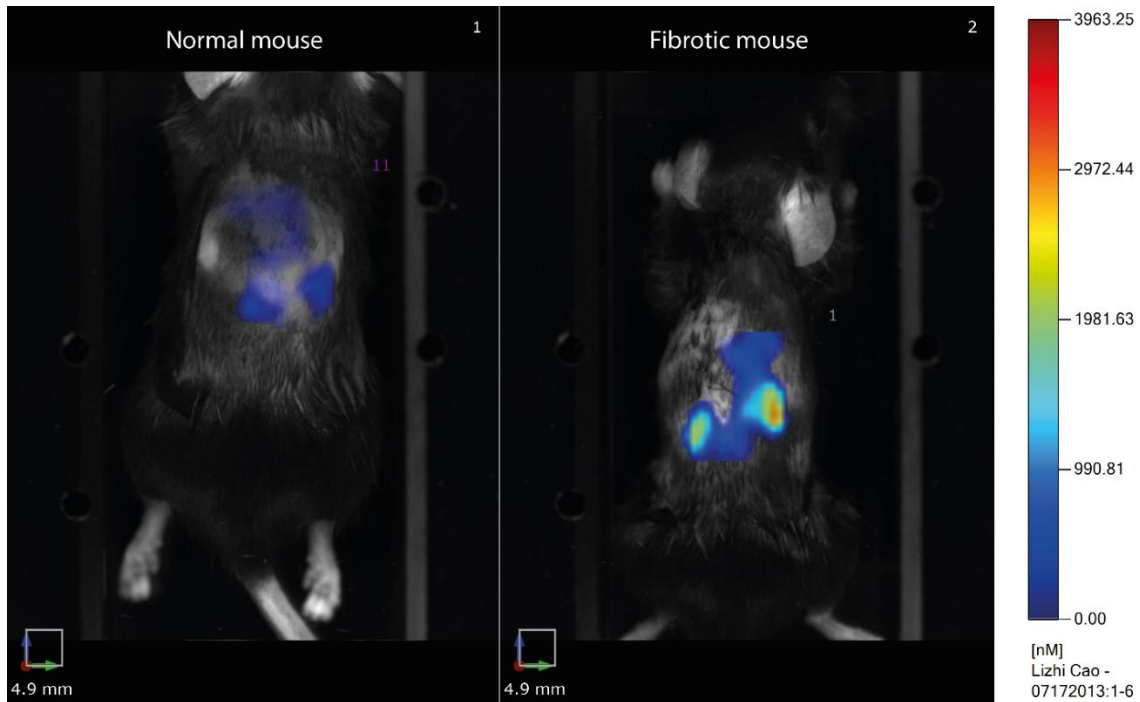
Figure 29. Accumulation of Alexa 750 labeled H5 antibody in lungs of normal and fibrotic mice by tail vein injection. Fibrotic mice was imaged 1 week after bleomycin injection. FMT images were acquired at approximately 10 minutes after injection.

To rule out non-specific accumulation in the lungs, an Alexa 750 labeled negative control scFv antibody was similar injected, and accumulation in the lungs was minimal (**Figure 30**).

In preliminary studies to monitor the kinetics of antibody circulation *in vivo*, it was observed that injected antibodies were rapid cleared via kidneys. At approximately 40 minutes following tail vein injection, most of the injected antibodies were accumulated in the kidneys (**Figure 31**) as monitored by FMT. By approximately 1 hour after injection,

antibodies were secreted by urination, although weak residual fluorescence could still be

detected 24 hours in the lungs following a single injection of H5.
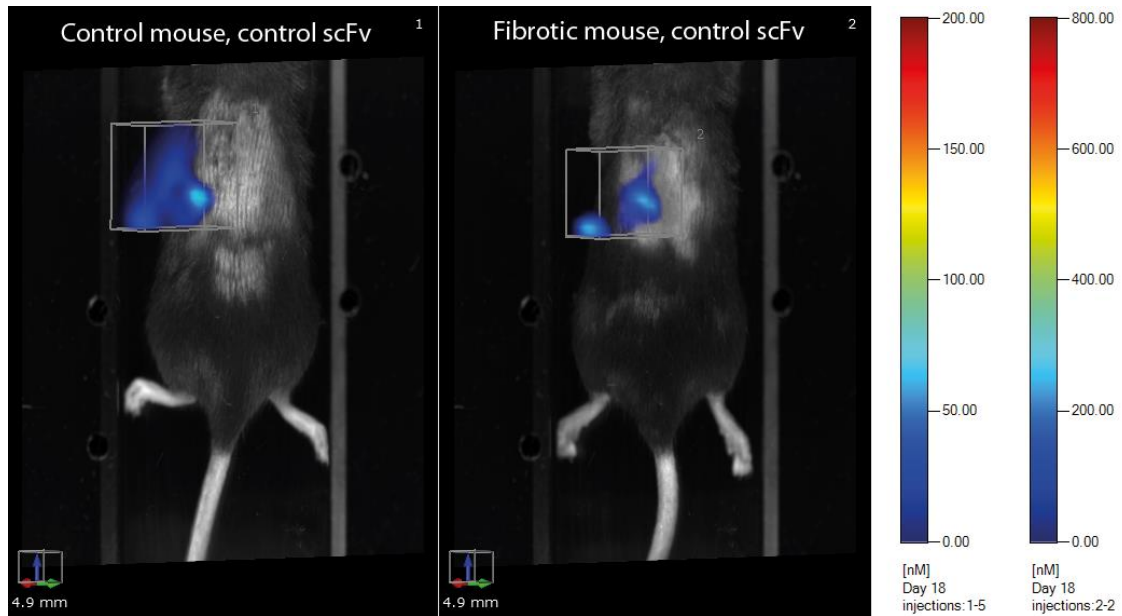
Figure 30. Minimal accumulation of control scFv antibody in mouse lungs. Alexa 750 labeled negative control scFv antibody was injected into control and fibrotic mice via tail vein injections, and imaged via FMT. Accumulation in control mouse: 6.44 AU, fibrotic mouse: 20.3 AU, arbitrary units.
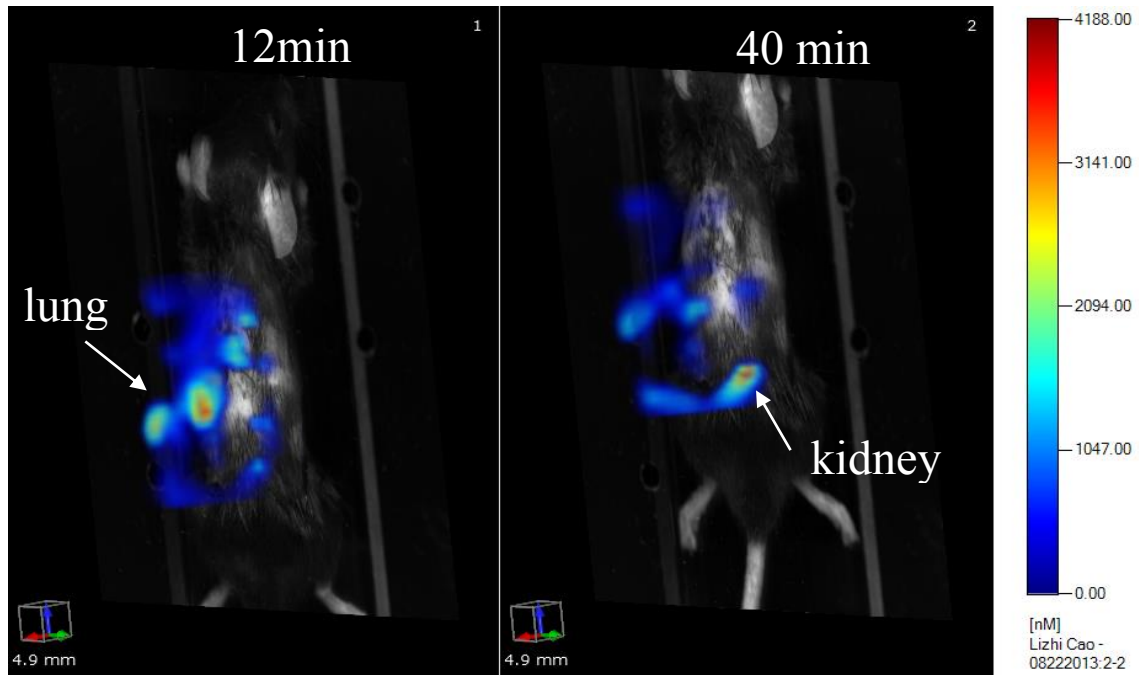
Figure 31. Rapid clearance of injected scFv antibodies via kidneys. One single injection of Alexa 750 H5 antibody was introduced via tail vein, and fluorescence was monitored via FMT. Scans shown in perspective to better delineate anatomy.

Monitoring fibrotic resolution using the H5 antibody

Using Immunofluorescence and Histology

Lungs were harvested from bleomycin injected animals at set time points (1, 2, 4, 8, and 10 weeks). Lung sections were embedded in OCT and frozen sections were generated for staining. By immunofluorescence staining with the H5 antibody, and corresponding H&E staining of serial sections (**Figure 32**), it was observed that maximal fibrosis was observed at the 1 week time point, and coincided with maximal H5 staining. As this time point, lung tissue morphology was significantly disrupted, as imaged with H&E staining. Increases in cell numbers was observed, with increased matrix deposition, and reductions in airway space. This is characteristic of the bleomycin model, and likely represented a combination of fibrosis and inflammatory responses.

Over the subsequent weeks, the architecture of the lungs returned to normal. By 8 weeks, histological sections of the lungs appeared similar to control (saline) sections. The staining of the H5 antibody mirrored the histological observations of fibrosis progression. At the 1 week time point, prominent staining of H5 observed, which decreased in staining and was similar to staining on control (saline) sections by the 8 week time point.
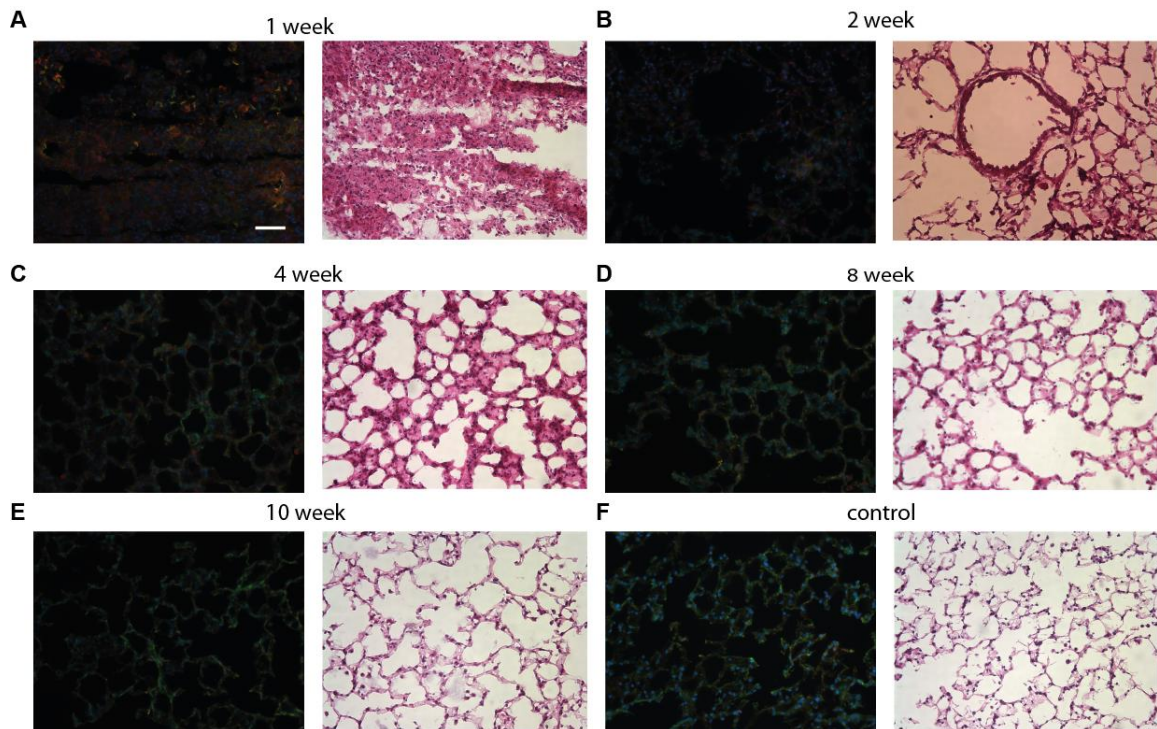
Figure 32. Resolution of fibrosis monitored by H5 in an in vivo model of mouse pulmonary fibrosis. Mouse lungs were harvested at the isolated time points following bleomycin injection, and frozen tissue sections were generated. A, C, E) Tissue sections were immunostained for H5 (red), Fn(green) and DNA (blue). B, D, F) H&E staining of a corresponding serial section at the same time points. Scalebar is 50 μm.

Using In vivo FMT imaging

The H5 antibody was labeled with Alexa 750, and *in vivo* imaging using FMT was performed at 1, 2, 4, and 8 week time points (**Figure 33**) to monitor progression and resolution of fibrosis. In contrast to the gradual resolution observed histologically, imaging by FMT using the H5 antibody revealed that excluding the 1 week time point, scans from the other time points were very similar. This may be attributed to vascular remodeling after 1 week, which may restrict access of the H5 antibody to the lungs.
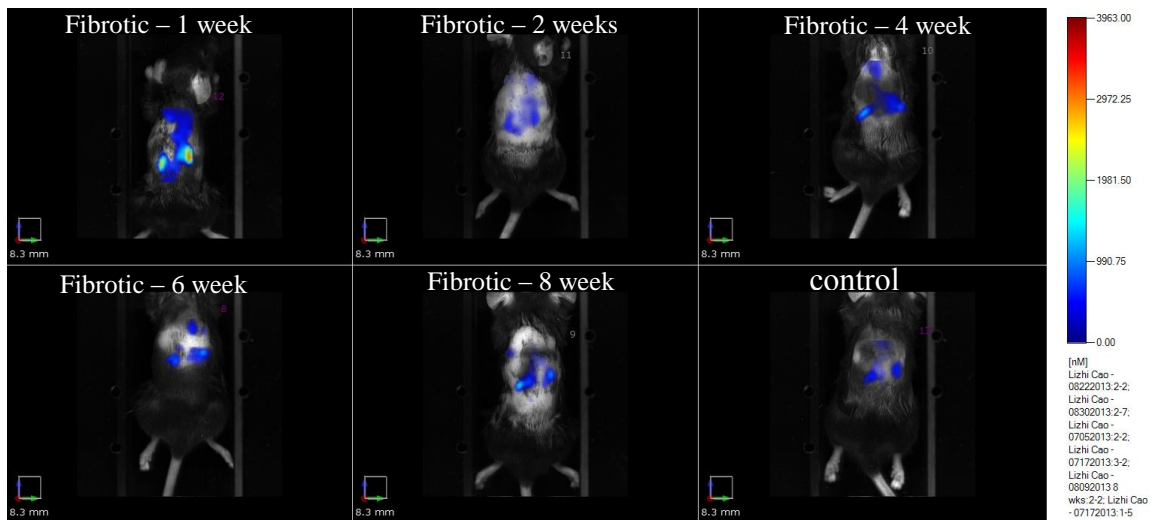
Figure 33. Monitoring of fibrotic resolution by FMT imaging. At set time points indicated, Alexa 750 H5 antibody was injected via tail vein, and accumulation in the lungs was monitored by FMT.

Discussion and Conclusions

The H5 antibody's ability to image Fn within the ECM was assessed in a number of *in vitro* model systems. Using *in vitro* generated Fn fibers deposited on PDMS membranes, we found that the staining of the H5 antibody, when normalized to the total amount of Fn within each fiber, increased in accordance to increasing fiber strain. Additionally, the H5 antibody was also able to fluorescently stain Fn fibers in a more physiologically relevant system of fibroblast-assembled ECMs, whereby staining of H5 correlated with pharmacological perturbations of cell contractility. Thus, the H5 antibody appears to be sensitive to mechanical alterations to Fn fibers, within more strained fibers resulting in higher staining The H5 antibody was also tested on *ex-vivo* lung samples from both normal and bleomycin-injured fibrotic mice, where we observed more pronounced staining of H5 on fibrotic lung sample. Part of the enhanced staining could be attributed to more Fn present in the fibrotic tissue regions, and this was confirmed by probing with a polyclonal anti-Fn antibody. However, co-staining with both the polyclonal anti-Fn antibody and the H5 antibody revealed that H5 was spatially heterogeneous in its staining of Fn within the matrix, with distinct regions of high H5 staining not localized with the polyclonal Fn antibody – further suggesting that H5 is recognizing a specific conformation of Fn within the ECM.

In preliminary studies, the utility of the H5 antibody for *in vivo* diagnosis of fibrosis was assessed in a mouse model of bleomycin-induced pulmonary fibrosis. At the time point associated with maximal Fn deposition as assessed by histology (1 week following bleomycin injection), *in vivo* imaging of accumulated H5 antibody in the lungs revealed that the H5 antibody was able to distinguish between control(saline) mice versus bleomycin-injured mice, with a (>4 fold difference) higher accumulation in lungs of bleomycin-injured mice. With further improvements and optimizations to selectivity of the

71

H5 antibody, one can envision using simple threshold image analysis for processing of clinical images for early detection of fibrosis.

We assessed the potential of the H5 antibody for use in monitoring fibrotic resolution over time. Over a period of 10 weeks, histological sections revealed that the mice graduated recovered without treatment, as expected of the single-dose intra-tracheal bleomycin model. By the 10 week time point, lung architecture, cellularity, and matrix straining was qualitatively very similar to uninjured controls. Additionally, the H5 antibody staining levels was also similar to staining levels on tissue samples from control uninjured mice. Together, these results suggested that the H5 antibody could be useful as an imaging probe to detect early stages of fibrogenesis, and its staining levels can be correlated to fibrotic resolution.

We were less successful in using FMT with the H5 antibody to track fibrosis resolution over time minimally invasively *in vivo* (**Figure 33**). We observed a rapid increase in H5 accumulation in the lungs at the 1 week time point, and lower accumulations at all other time points. This may be attributed to vascular damage and remodeling following the bleomycin injection, which may limit transport of the H5 antibody from the blood at these later time points. Future investigations may explore alternative models of fibrosis without this complicating effect, or controlling for this vascular effect using pharmacological agents.

CHAPTER 6

DISCUSSION

The role of mechanical forces in mediating cell-ECM interactions is becoming increasingly important in understanding how the ECM directs cell behavior and cell fate. In particular, forces emanating from contractile cells such as pathogenic myofibroblasts have been hypothesized to partially unfold ECM proteins like Fn, thus engaging/disengaging theorized integrin "switches"(110) and perhaps be one cause in the pathogenesis of idiopathic pulmonary fibrosis(64). Despite considerable *in silico* and *in vitro* evidence for the extensibility of Fn within fibers and Fn type III domain unfolding (6, 16, 18) there is still no direct evidence that such molecular events occur *in vivo*, a fact that perpetuates the debate regarding the physiological relevance of such observations. We found that we could generate *in vitro* Fn fibers, apply mechanic strain, and observe a
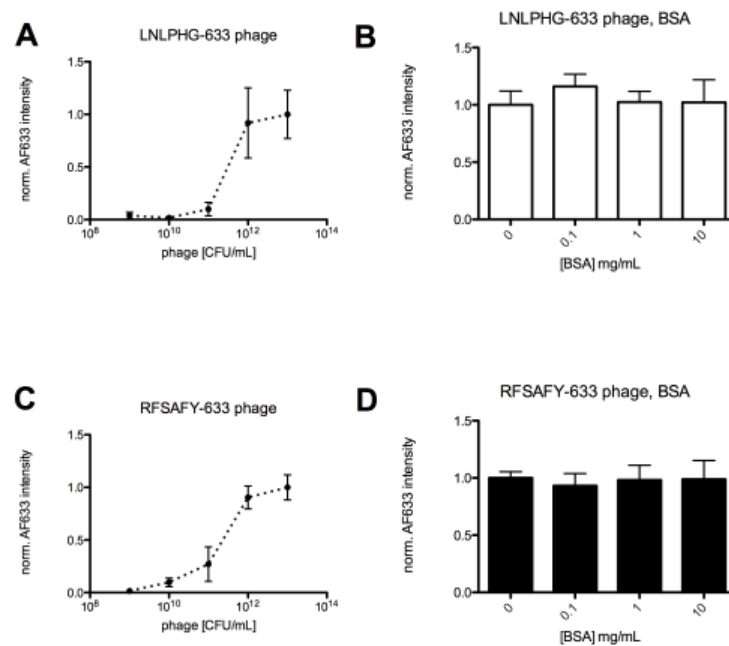
Figure 34. Staining of phage probes is specific and cannot be displaced by BSA. A) AF633 labeled LNLPHG phage were incubated on Fn fibers of $\lambda = 0.9$ at the indicated concentrations for 1 hour. **B)** AF633 labeled LNLPHG phage were incubated on Fn fibers of $\lambda = 0.9$ at the indicated concentrations for 1 hour. **C-D)** the indicated phage were co-incubated with increasing concentrations of BSA on Fn fibers for 1 hour.

concomitant correlation between fiber strain with the exposure of cryptic cysteine residues, consistent with literature reports(111). Furthermore, our lab has also shown that recombinant Fn fragments could be generated to mimic the conformational states of the Fn9-10 type III repeats, and demonstrated a role in directing integrin specificity(51). However, questions remained on whether these biophysical conformational changes to the Fn exists within native ECMs *in vivo*, and furthermore whether these conformational changes could be exploited as molecular targets for study.
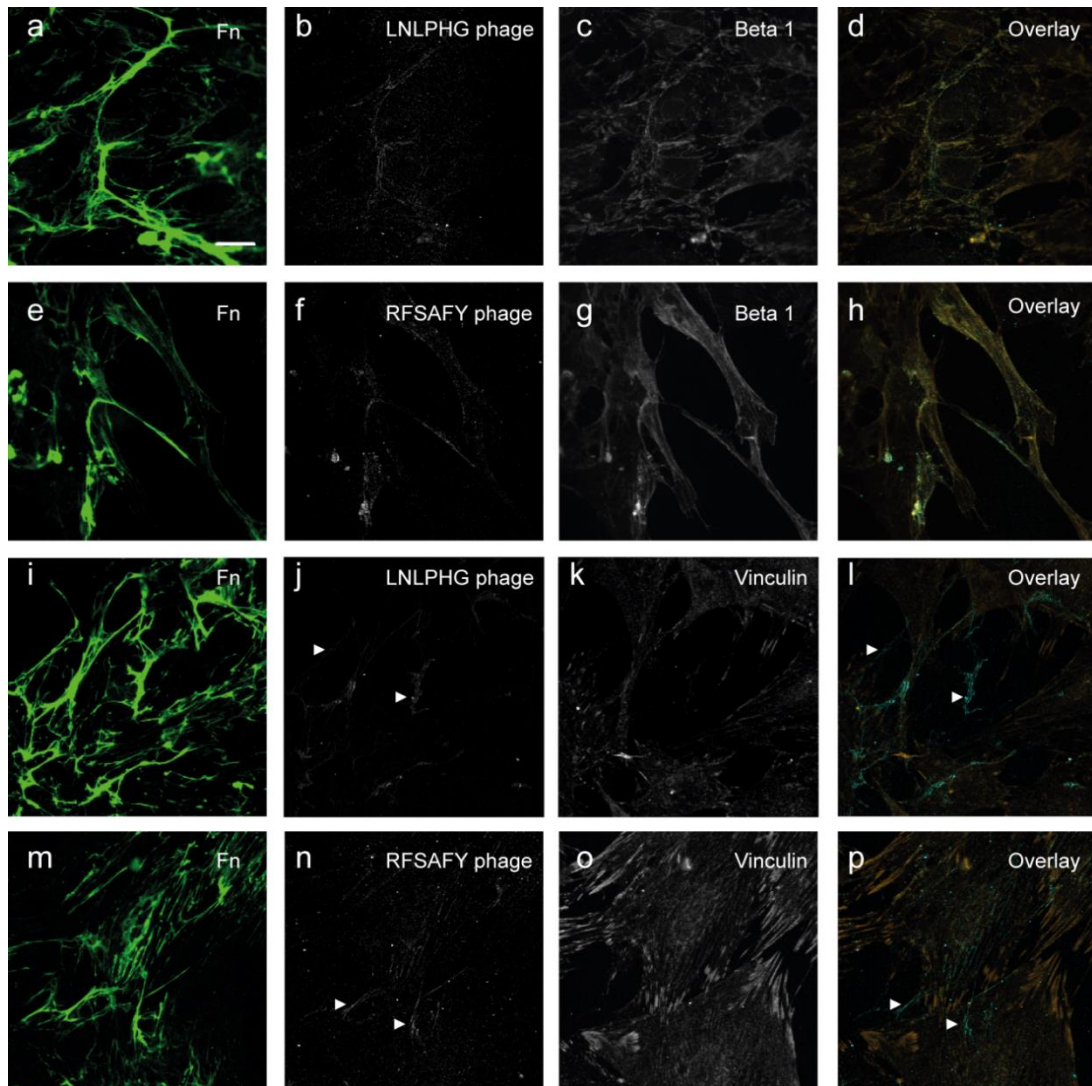
Figure 35. Co-staining of phage probes with Beta 1 integrin subunit and vinculin on fibroblast cultures. a-d) Staining of LNLPHG phage with Beta1 integrin subunit. **e-h)** staining of RFSAFY phage and Beta 1 integrin subunit. **i-l)** staining of LNLPHG phage and vinculin. **m-p)** staining of RFSAFY phage and vinculin.
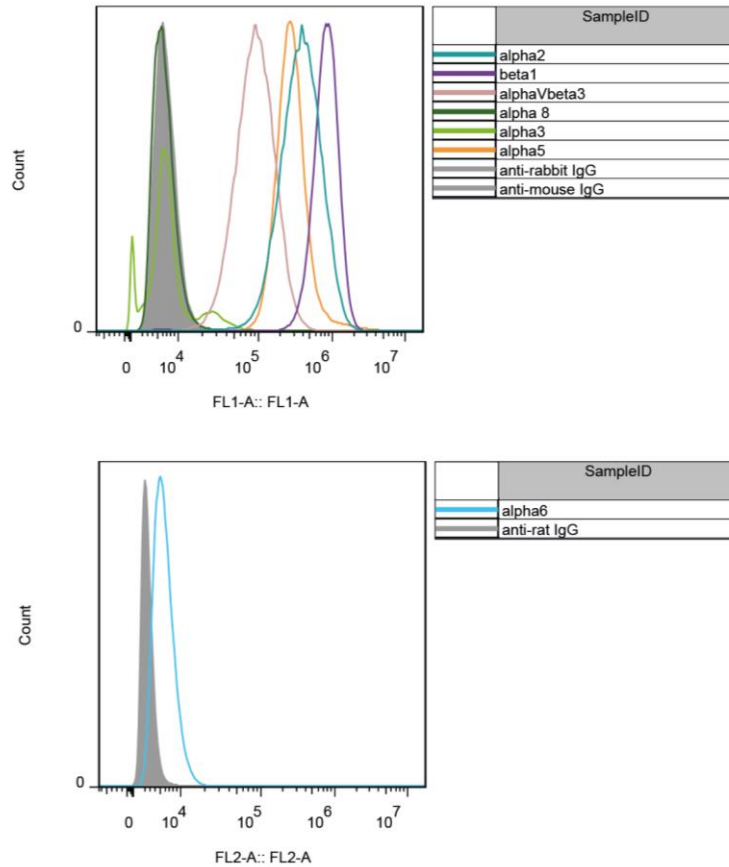
Figure 36. Integrin expression of human foreskin fibroblasts. At least
50000 events were recorded for each sample. Fluorescence was gated on
IgG isotype controls.

 These questions led us to develop platform technologies to isolate conformation-
specific molecular probes to Fn: both for Fn fibers, as well as to engineered Fn type III
repeat fragments. Using a peptide phage display library, we isolate two phage clones
displaying the peptides LNLPHG and RFSAFY that targeting to Fn fibers under relaxed
and strained conditions, respectively.

 The two peptides display highly reproducible binding characteristics to Fn fibers:
with increasing (decreasing) strain, LNLPHG binding is reduced (increased) and RFSAFY
binding is increased (reduced). Therefore these two probes can be used in concert to
achieve exceptionally high resolution of the strain state of Fn fibers through cross
comparison of their binding to the same fiber (e.g., **Figure 20**), assuming no steric
hindrance between the two probes. Most importantly, these peptide-based probes are

capable of discriminating native Fn fibers, enabling the detection of Fn fiber strain events *in vivo*.
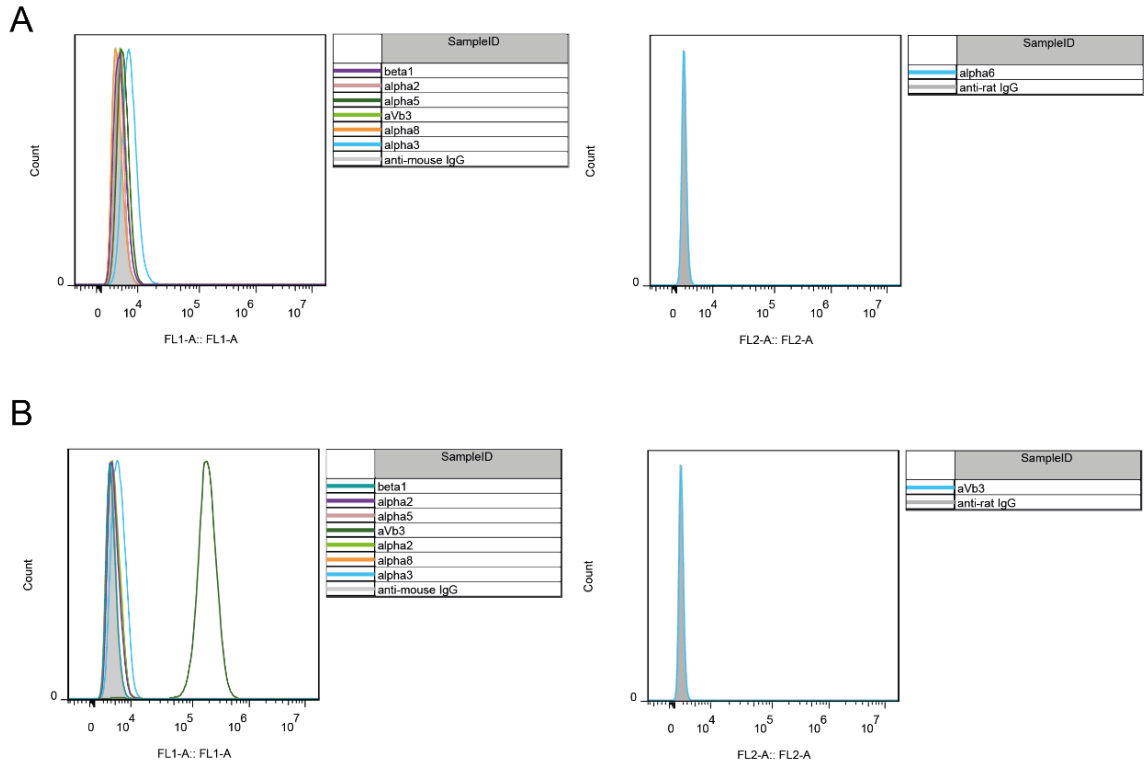
Figure 37. Integrin expression of CHO cell lines. A) CHOB2 cells, **B)** CHOB2-αvβ3 cells. At least 50000 events were recorded for each sample. Fluorescence was gated on IgG isotype controls.

Even with the selectivity of each identified probe in detecting and discriminating Fn fibers of variable strain, the specific epitopes on Fn fibers to which these probes are targeting cannot be determined with the present system. Indeed, this is not a trivial matter since the structure and molecular packing of Fn fibers themselves have not been elucidated. The fibrillogenesis process is known to involve self-association of Fn molecules through integrin-mediated mechanically-exposed cryptic polymerization sites (3) yet recent evidence suggests as many as 8 different Fn-Fn interactions can occur further complicating a basic understanding of Fn fiber arrangement(8). Thus under force, the extensibility of Fn fibers may be due to a combination of rearrangement of Fn-Fn interactions within the fiber, rearrangement of the heterotypic type III domain interactions within a single Fn molecule(18), or unfolding of Fn type III domains (70). Any of these events could

potentially create new epitopes that can be targeted by the phage. Additionally, recent evidence suggests that Fn fibers become fouling, i.e. exhibit significant non-specific and presumably hydrophobic protein-protein interactions, upon straining(76). However, our data suggest that this non-specific fouling effect does not contribute significantly to the observed specific binding of our probes, as we observe saturable binding of our probes with increasing concentrations **(Figure 34 A, C).** Furthermore, at the saturation point, incubations with increasing amounts of BSA **(Figure 34, B, D)** did not significantly affect either probe signal, suggesting that it was not capable of competing for specific binding to fibers with our probes. Additionally, we do not observe significant levels of nonspecific staining of the relaxed fiber-specific probe (or the control phage) on strained fibers. Co-staining of both phage probes with the fibrillar adhesion marker integrin beta-1 and the focal adhesion marker vinculin did not appear to show significant differential phage accumulation at sites of adhesion **(Figure 35)**, suggesting that the epitope targeted by the phage probes is likely along the entire length of the Fn fiber, and not localized at sites of Fn- adhesion linkages.

Building upon techniques that we have used in working with Fn fibers, we then performed phage display using antibody libraries and selection on Fn fragments spanning the 9th and 10th type III repeats to isolate Fn conformation specific antibodies. The approach of isolating conformation-specific antibodies by phage display is not unique, as recent work by Lefkowitz and coworkers have used phage display to isolate a conformation specific Fab to activated β-arrestin-1(112). Likewise, we have used a similar approach, by using phage display to isolate conformation-specific antibodies to the FnIII9-10 region, in support of detecting molecular signatures of the hypothesized integrin switch.

Using phage display, we isolated and identified one particular scFv antibody – the H5 antibody, that was found to have mechano-sensitive immunofluorescence staining of Fn in multiple model systems (*in vitro* fibers, assembled ECMs in culture, *ex vivo* tissue samples), but with more robust staining compared to the earlier peptide phage probes

isolated on Fn fibers, possibly due to the higher affinities of the antibody probes versus the peptide phage probes. Furthermore, the H5 antibody was also found be functionally capable of modulating the attachment of cells to Fn by selectively blocking Fn-integrin αvβ3 interactions – suggesting perhaps detection of the long sought after "integrin-switch". In cell attachment assays using human foreskin fibroblasts (HFFs), co-incubation of the cells with H5 reduced the cell attachment to 59% compared to cells without H5 (**Figure 13**). Incubation with a function blocking antibody against β1 integrins in these cells reduced attachment to 30% even without H5 antibody, but H5 antibody together with function blocking antibody against β1 integrins together further reduced cell attachment to 11% of control levels. These results suggested that H5 was likely inhibiting the interactions of other integrin(s) besides β1 integrins, or that it may have broader inhibitory effects on multiple Fn integrins, that included β1 integrin among other integrins that was express by HFFs. However, HFF express a number of integrin receptors on the cell surface, including α2, α6, α5β1, αVβ3, among others (**Figure 36**), and thus it was difficult to establish which integrin-Fn interaction(s) the H5 antibody specifically inhibits.

 For this reason, we looked at cell lines that expressed a more restricted set of integrins. We first investigated the H69 human small cell lung carcinoma cells (**Figure 14**), which expressed predominantly α3β1 integrins and moderate amounts of α6β1 (113). These integrins bind primarily laminin, but α3β1 also has reported binding to Fn and collagen(113). We observed no significant inhibition of cell attachment with H5 incubation (reduction of attachment from 42% without H5 to 35% with H5). In these cells, incubation with the β1 integrin function blocking antibody had no statistical effect on attachment to Fn (with β1 mAb: 30.9% attachment, without: 42% attachment). For comparison, the background level of attachment to BSA blocked tissue culture wells was 27%. Together, these results suggested that H69 cells do not attach strongly to Fn, and furthermore integrin α3β1 was not the primary integrin mediating this attachment to Fn. The H69 cells have also reported to express αV mRNA as well as small amounts of the protein (114), and this may

be one way in which these cells mediate binding to Fn in the presence by β1 integrin binding antibodies, as integrin αvβ1 can also function as a low affinity fibronectin receptor(115). However, this does not seem to be the target of the H5 antibody's inhibitory effects, as incubation of H5 had no statistical effect on attachment levels.
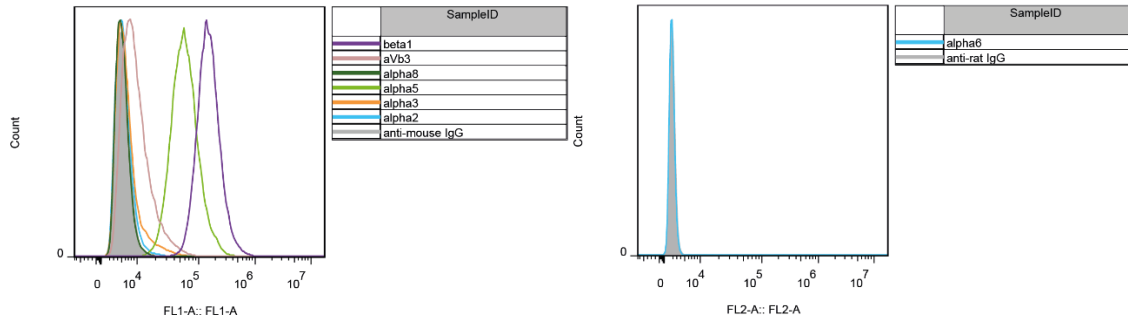
Figure 38. Integrin expression of K562 cells. At least 50000 events were recorded for each sample. Fluorescence was gated on IgG isotype controls.

In order to isolate the integrin specific inhibitory effects of the H5 antibody, we chose to test inhibition of cell attachment in other engineered cell lines: the CHOB2 cell line, along with the CHOB2 cells stably transfected with integrin αvβ3. The CHOB2 cell line was developed as a mutant of the popular Chinese hamster ovary cell line (CHO), in which CHOB2 cells were distinguished by the lack of α5, αV, and β3 integrin subunits(115). By flow cytometry, it was verified that CHOB2 cells lacked all relevant integrins, and stably transfected CHOB2-αvβ3 cells expressed integrin αvβ3 at high levels (**Figure 37**). In CHOB2 cells stably transfected with integrin αvβ3 (**Figure 15**), we observed that incubation with the H5 antibody reduced cell attachment from 51.7% to 22.7%, similar to attachment levels of the CHOB2 parent cell line (22.5%), suggesting robust and complete abrogation of attachment by the H5 antibody.

In another cell line, the K562 leukemia line, which expressed only integrin α5β1 at appreciable levels (**Figure 38**), we observed that the H5 antibody reduced cell attachment by 30% (**Figure 16**), and that this effect was abolished by blocking antibodies against β1. Together, these results suggested that the H5 antibody inhibits cell attachment to Fn by

primarily interfering with Fn-integrin $\alpha v \beta 3$ interactions, and also partially interfering with Fn-integrin of $\alpha 5 \beta 1$ interactions.

The mechano-sensitive targeting of H5 to Fn was supported by the data from a number of experiments that we have conducted. After phage panning and selection, we performed an ELISA assay of binding of scFv antibodies against both adsorbed $FnIII_{9*10}$ and $FnIII_{9-4G-10}$ fragments, from which we discovered that the H5 antibody preferred bound to the $FnIII_{9-4G-10}$ by a factor of approximately 2. In addition, in analyzing the binding kinetics of H5 antibody to both of these Fn fragments using surface plasmon resonance (SPR), the binding affinity of H5 to the $FnIII_{9-4G-10}$ fragment was found to be approximately 6.7 times stronger (Figure 11) compared to binding to the $FnIII_{9*10}$ fragment ($K_D = 16nM$ on $FnIII_{9-4G-10}$ versus $K_D = 107nM$ on $FnIII_{9*10}$). Together, these results confirm that H5 binds the $FnIII_{9-4G-10}$ fragment, which mimics a "strained" conformation of the Fn, with higher affinity. This observation was translated also to Fn fibers, in which we observed that indeed Fn fibers of higher strain show much higher staining intensities of the H5 antibody compared to Fn fibers of low strain. Indeed, the approach of isolating conformation-specific antibodies by phage display is not unique, as recent work by Lefkowitz and coworkers have used phage display to isolate a conformation specific Fab to activated β-arrestin-1.[24] Likewise, we have used a similar approach in this paper, using phage display to isolate conformation-specific antibodies to the FnIII9-10 region, in support of detecting molecular signatures of the hypothesized integrin switch.

The utility of the H5 antibody in mechano-sensitive imaging of Fn was assessed in a number model systems. Most directly, using Fn fibers deposited on PDMS membranes of defined strain (**Figure 24**), normalized fluorescence staining of H5 increased with increasing fiber strain: with little staining on relaxed fibers, and pronounced staining of the fibers at higher strains. Notably, staining was not uniform along the length of the fibers, and seemed punctate in nature – suggesting perhaps differences in conformations of the 9-10th Fn type III repeats along the length of the fiber. Moreover, in ECMs assembled by

80

fibroblasts in culture, the H5 antibody was also able to distinctly stain Fn fibers within the ECM (**Figure 25**). The staining patterns of H5, while specific to Fn fibers, did not completely overlap with fluorescently labeled tracer Fn that was incorporated into the Fn matrix. This suggested that the H5 antibody was able to discern Fn molecules that were of a different conformation, and not otherwise observable by simply staining against Fn. Furthermore, H5 staining greatly increased following TGF-β stimulation of the fibroblasts, which induced cell contractility and increased ECM deposition. However, after brief exposure to TGF-β (overnight), the amount of Fn deposited and assembled into the ECM is not significantly more compared to unstimulated cells. Likely, the Fn already assembled into fibers within the matrix may be under more tension, as these fibroblasts have been induced to exert higher contractile force on their ECMs. Indeed, the enhanced staining of H5 may be suggestive of this ECM signature, in which increased H5 staining may suggest an increase in the conformational epitope for H5 between the 9-10th Fn III domain in these TGF-β stimulated cultures.

We then tested the H5 antibody on lung tissue samples from normal and fibrotic mice in a bleomycin-induced model of pulmonary fibrosis (**Figure 26**). From immunofluorescence studies on frozen lung tissue slices, we observed that the slices from the fibrotic lungs contained more Fn within the interstitium when compared to tissue slices from normal lungs, indicative of enhanced matrix deposition and ongoing fibrogenesis. However, we did observe substantially more H5 staining on fibrotic tissue samples, compared to control (non-fibrotic) samples. Furthermore, when the H5 antibody was co-stained with a polyclonal anti-Fn antibody, we were able to again observe non-complete overlapping and co-localization of the two antibodies, again suggesting that H5 is able to discern conformational states of Fn that was not otherwise observable using a simple antibody stain against Fn. We speculate that regions of high H5 staining maybe be outlining regions of "fibroblastic foci", which are nodules of connective tissue and highly contractile myofibroblasts, and is a signature of pulmonary fibrosis in human IPF tissue samples.

To explore the clinical translational potential of the H5 antibody for using in minimally invasive diagnosis and monitoring of pulmonary fibrosis, we designed experiments using Alexa Fluor 750 labeled H5 antibodies injected via the tail vein in both normal and fibrotic mice at one week after bleomycin injury. We then monitored the accumulation of H5 in the lung interstitial spaces post-injection. Using fluorescence molecular tomography (FMT) imaging, accumulation of H5 was distinctly discernible in both lungs, and maximal signal was observed at 10 minutes after injection. Importantly, the accumulation of injected H5 in the lungs correlated positively with fibrosis (**Figure 29**), with approximately 8.8 times more accumulation in the lungs of fibrotic mice compared to normal lungs (745.75 AU vs. 84.99 AU, arbitrary fluorescence units). This difference in targeted accumulation in the lungs of fibrotic mice is likely due to 2 main reasons: (1), fibrotic lungs contained more Fn within the lung parenchyma and thus more of the injected H5 should accumulate simply due to more Fn present in the lungs of fibrotic mice, and (2), it is likely that within the lungs of the fibrotic mice, due to myofibroblast activation and proliferation, more of the Fn has adopted the molecularly strained conformation that the H5 antibody recognized with high affinity. The relative contributions of these two causes to the enhanced accumulation of H5 in fibrotic lungs is difficult to separate *in vivo*, and may require multi-modal imaging and normalizing with respect to amount of Fn present in both normal and fibrotic lungs.

We assessed the potential of the H5 antibody for use in monitoring the resolution of fibrosis over time, again using the bleomycin mouse model of fibrosis. We harvested lung tissues samples from bleomycin-injected mice at set time points after injury, and tracked the progression and resolution of fibrosis on these tissue samples histologically and using the H5 antibody in fluorescence imaging (**Figure 32**). As expected, we observed rapid onset of fibrosis and an inflammatory phenotype at the one week time point in the lungs. This manifested in increased cellular proliferation, enhanced matrix deposition,

reduction in air space, and general disruption of alveolar structure. At this time point, we also observed the maximal H5 staining of Fn within the ECM.

Over a period of 10 weeks, histological sections revealed that the mice graduated recovered without treatment, as expected of the single-dose bleomycin model. By the 8 week time point, lung architecture, cellularity, and matrix straining was qualitatively very similar to uninjured controls. Additionally, the H5 antibody staining levels was also similar to staining levels on tissue samples from control uninjured mice. Together, these results suggested that the H5 antibody could be useful as an imaging probe to detect early stages of fibrogenesis, and its staining levels can be correlated to fibrotic resolution.

We were less successful in using FMT with the H5 antibody to track fibrosis resolution over time minimally invasively in vivo (**Figure 33**). We observed a rapid increase in H5 accumulation in the lungs at the 1 week time point, and lower accumulations at all other time points. This may be attributed to vascular damage and remodeling following the bleomycin injection, which may limit transport of the H5 antibody from the blood at these later time points. Indeed, this is a limitation of the bleomycin model of mouse pulmonary fibrosis. Future investigations may explore alternative models of fibrosis without these complicating effects, or controlling for this vascular effect using pharmacological agents.

CHAPTER 7

CONCLUSIONS AND FUTURE DIRECTIONS

Over the past two decades, researchers in the biomaterials, tissue engineering, and regenerative medicine communities have come to recognize and fully appreciate the importance of the extracellular matrix. This "matrix centered" paradigm has fueled numerous research efforts to better understand the complexities of the biochemical and biophysical properties of ECMs, with the ultimate goal of harnessing the potential of the ECM to control tissue homeostasis, repair/regeneration, and control disease pathogenesis. Indeed, significant progress has already been made in these efforts. Decellularized ECMs have emerged as one of the most promising scaffolds for tissue engineering in a number of organ systems(116-119), and ECM derived from the small-intestine submucosa (SIS) has been shown to have potent bioactivities in tissue remodeling and regeneration(120, 121).

More recently, researchers have discovered that biophysical changes to the ECM is a critical factor during embryogenesis and tissue development, and that mis-regulation of such changes may be a contributing cause in many cancers and fibrotic diseases. These changes to the ECM can have wide ranging consequences, ranging from changes in binding and sequestration of growth factors, conformational alterations in ECM proteins leading to changes in matrix architecture, and alterations in presentation of cell-binding motifs. Indeed, the importance of ECM mechanics *in vivo* is consistent with the large collection of literature accumulated over the past decades on the effects of substrate rigidity on cultured cells. However, directly probing the conformational states of constitute ECM proteins in native ECM has been difficult, and has hampered efforts to compare *in vitro* experimental findings to physiology *in vivo*.

In this thesis, I have focused on the ECM protein fibronectin (Fn), and have developed mechanically-sensitive targeting probes to both Fn fibers (Chapter 3), and a

portion of the 9th Fn type III repeat (Chapter 4). Furthermore, these probes were to be useful as imaging probes (Chapter 5) for immunofluorescence imaging of Fn within cultured ECMs *in vitro*, as well as physiologically relevant tissue samples. In addition, the H5 antibody was also shown to be promising for targeting of Fn *in vivo*, in a mouse model of pulmonary fibrosis.

The H5 antibody could be useful as an enabling technology for fundamental cell-ECM interactions, as well as for translational applications for minimally-invasive imaging of the Fn ECM for disease diagnosis and monitoring. Future work using the H5 antibody could be to explore the distinct staining pattern observed on Fn fibers, as it may suggest that even under uniform strain in a Fn fiber, heterogeneities may exist in the conformation of Fn molecules within this fiber. In addition, molecular dynamic simulations focused on the linker region between the 9th and 10th Fn type III repeats may help elucidate both the epitope of the H5 antibody (likely on the face of 9th type III repeat adjacent to the linker region, facing the 10th type III repeat), and the mechanisms by which a 4 glycine insertion could alter the stability and equilibrium conformations of this region of Fn.

To further characterize the H5 antibody for translational *in vivo* imaging applications, work should be focused on determining the bio-distribution of the H5 antibody following injection in mice, monitoring accumulation in all relevant organs, and determining the clearance times. Additionally, it would be useful to characterize the H5 antibody on human lung tissue, such as tissue samples from IPF patients, to assess clinical relevance of the H5 as a mechano-sensitive antibody for diagnosis of IPF.

In collaboration with our colleagues at the University of Michigan (Eric White), we will assess the H5 antibody on lung tissue sections obtained via lung cores of normal and IPF patients. Immunofluorescence staining will be performed on frozen, cryosectioned samples. Where possible, adjacent sections will be stained with standard histochemical stains (H&E, Masson's, etc.) in order to establish any specificity of the probes to particular pathological features. In preliminary experiments using our

candidate H5 antibody, the White lab has demonstrated that H5 antibody is capable of binding to fibrillar Fn within human IPF and normal tissue samples. Moving forward, we will characterize differences in conformation-sensitive antibody staining in normal vs. IPF patient samples, and correlate to histological features such as fibroblastic foci, dense fibrosis, and honeycombing.

More broadly, we envision that other investigators can take a similar approach to develop targeting probes to other ECM fibrillar structures, such as collagen, or fibrin. Such developments would open up new avenues of research into the role of ECM mechanics on cell and tissue physiology and may have applications such as imaging guided resection of diseased tissues *in vivo*.

APPENDIX A

DEVELOPMENT OF MAP/DEP TWEEZERS FOR SINGLE MOLECULE FN FRAGMENT TWEEZING

In our investigations into Fn conformational change under force, we explored methods to experimentally manipulate and unfold Fn type III repeats at the single molecule scale. Conceptually, we envisioned a platform whereby we can specifically tether recombinant proteins of Fn type III repeats to an assay surface at their N-termini, and then at their C-termini to polymeric beads. We can then apply forces to these tethered beads on a massively parallel scale to unfold the Fn type III repeats. Further, enclosing such a design in a microfluidic package would allow for potential integration with biochemical methods such as phage display.

A number of biophysical methods have been developed more recently to interrogate molecular interactions at the micro/nanoscale, including: atomic force spectroscopy(122), optical (123) and magnetic (124, 125) tweezers, micropipette based methods(126, 127), and dielectrophoresis tweezers(128-130). These methods, while powerful in specific applications, have a number of important limitations. Atomic force microscopy/spectroscopy and optical tweezers are exquisitely sensitive, but are inherently low throughput. The other "tweezer" based methods usually involve applying a force to tweeze a biomolecule-tethered microbead, but differ in their methodology of generating this force. Importantly, because these methods all utilize a single force to tweeze and displace beads, there is no mechanism to move and hold beads at specific equilibrium positions. Conceivably, two opposing forces could be used to spatially "tweeze and hold" beads at defined positions. Rapid modulation of this position could then make it possible to interrogate bead-surface binding interactions with spatial (x, y, and z-axis) and temporal (time) control. Furthermore, if this could be realized in a highly parallel format, then one could conceivably use controlled bead displacement as a mechanism to develop high
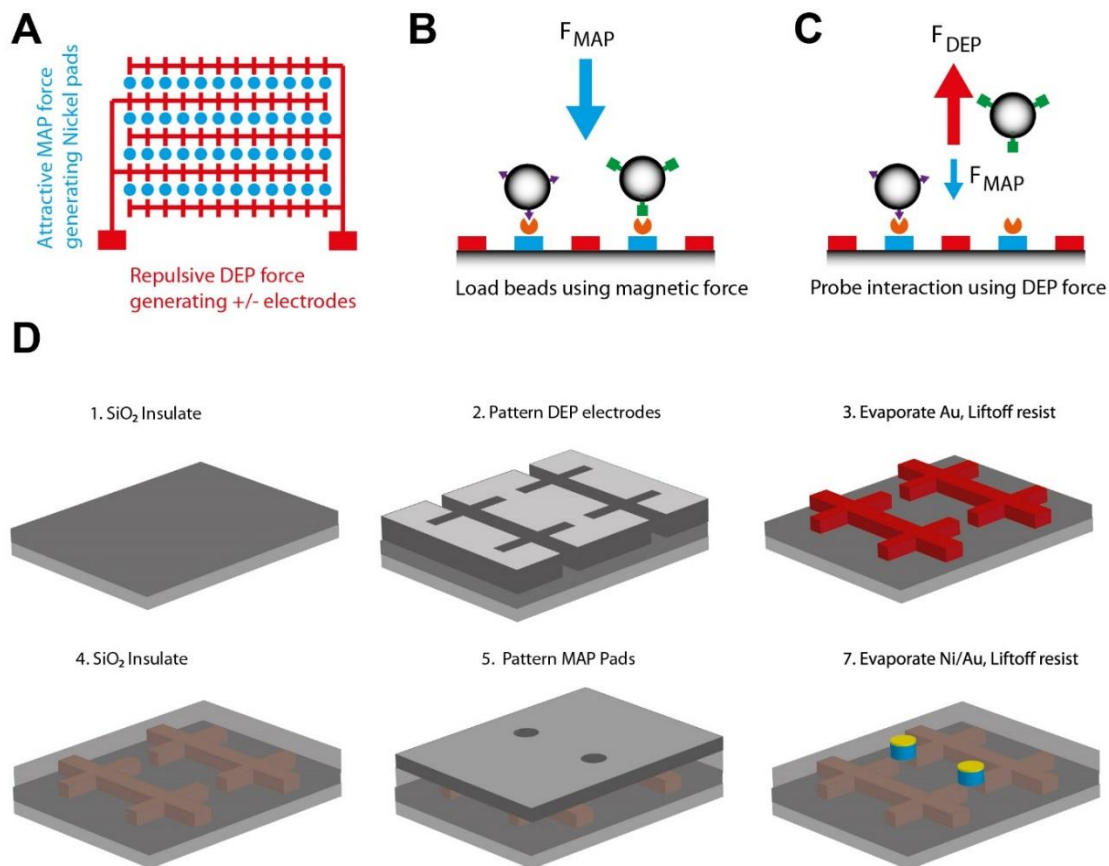
Figure 39. Design of combined MAP-DEP bead displacement chip. A) Schematic of chip layout, Nickel circular pads (blue) can be magnetized in the presence of an external magnetic field, and were flanked by inter-digitated gold electrodes (red). **B)** Paramagnetic beads were introduced to chip surface by microfluidics and loaded onto the magnetic pads, specific antibody-antigen interactions strengthens bead surface tethers. **C)** Interactions probed by application of sufficient DEP force to displace non-specifically loaded beads, but not specifically antibody-bound beads. **D)** Microfabrication process: 1. Grow SiO_2 layer on Si substrate, 2. Pattern electrodes by EBL, 3. Deposit Ti/Au, 4. Liftoff to create electrode layer, 5. Grow SiO_2 to cover electrodes, 6. Align and pattern pads by EBL, 7. Deposit Ti/Ni/Au, 8. Liftoff to create magnetic pads layer.

throughput platforms for controlled Fn type III repeat unfolding studies, and screening of specific biomolecular interactions using methods such as phage display.

Experimental Design

To this end, we chose to exploit magnetic (F_{MAP}) and dielectrophoresis (F_{DEP}) as the two opposing forces, and demonstrated a proof-of-concept design of such a platform by demonstrating the ability to discriminate between specific antibody-antigen interactions from non-specific protein-protein interactions.

This design could be realized using standard microfabrication processes on an insulated silicon substrate. Interdigitated electrodes were used to generate the repulsive DEP force, and patterned soft magnetic circular pads were used to generate the attractive magnetic force to attract superparamagnetic beads to the surface (**Figure 39A**). Manipulating magnetic beads by the application of a magnetic field is termed magnetophoresis(131) and is routinely used in biomedical research for cell separation and immunoassays. The net force imparted on a magnetic bead can be calculated in accordance with the bead's magnetic susceptibility χ, volume of the bead V, and the magnetic flux density of the field, by the relation

$$F_{MAP} = V\chi/\mu_0 \nabla B^2 \text{ (132)}.$$

COMSOL simulations suggested that in the presence of a permanent magnet, the nickel pads on the chip surface can be magnetized, with a surface magnetic flux density of 0.09T. Estimation of the magnitude of F_{MAP} for our design is then approximately 14.2 $\pm$ 0.43pN, as calculated by microfabrication geometries and manufacturer's parameters of the magnetic beads (V = 1.15 $*10^{-17}$ m^3, χ = 192$\pm$40). Commercially available magnetic beads (Dynalbeads, Invitrogen) are mostly polystyrene based (>98% by mass), but contain embedded superparamagnetic nanoparticles. These beads are thus amenable to dielectrophoresis manipulation. The phenomenon of dielectrophoresis motion arises by differential polarization of a dielectric particle within a non-uniform or time varying electric field. The net force driving this motion results from the force difference on charges at opposing ends of an induced dipole. For a homogeneous sphere(133) of radius r, the time averaged DEP force is described by the equation

$$\langle F_{DEP} \rangle = 2\pi r^3 \varepsilon_m Re \left\{ \frac{\varepsilon_p^* - \varepsilon_m^*}{\varepsilon_p^* + 2\varepsilon_m^*} \right\} \nabla |\vec{E}_{rms}|^2$$

where ε_m is the dielectric constant of the medium, and ε_p^* and ε_m^* are the complex dielectric constants of the particle and medium, respectively. In a time varying electric field, the
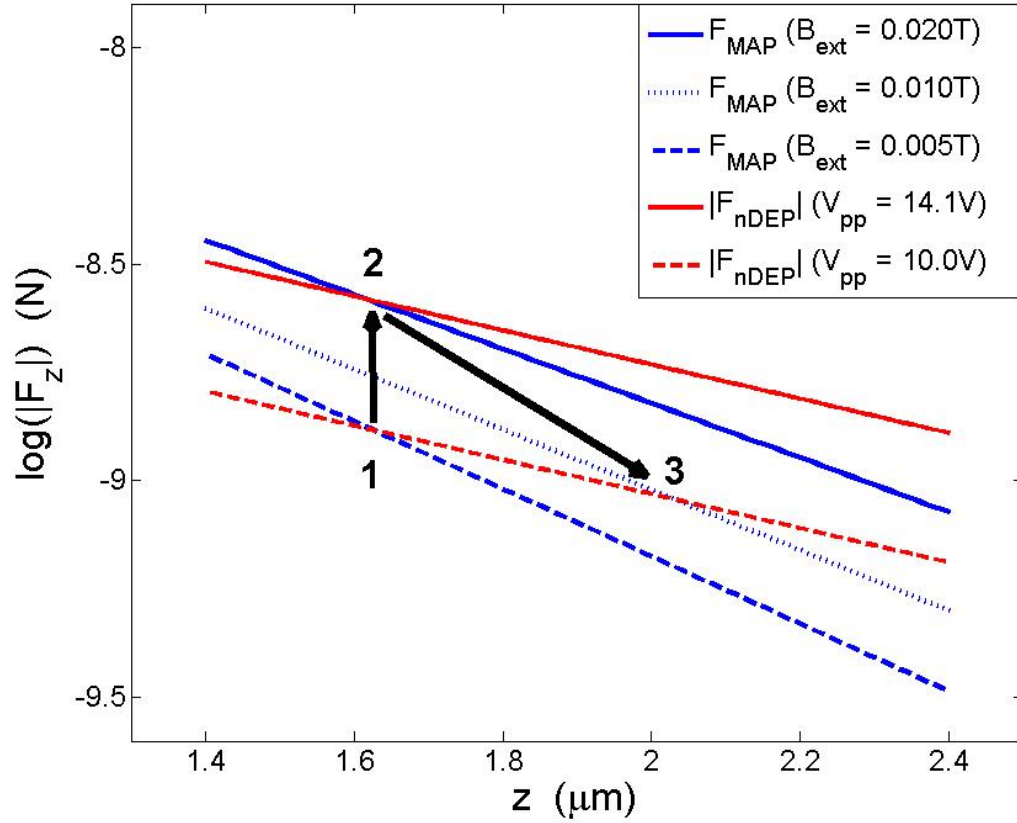
Figure 40. Numerical simulation of the MAP and nDEP forces on a 2.8 μm Dynalbead® imparted by the device as a function of its z-axial position. We note that F_{MAP} decreases faster than F_{nDEP} with increasing separation of the bead from the device surface. $z = 0$ is at the magnetic pad surface, $z = 1.4$ is the center of the bead when it sits on the pad surface, and the z value corresponding to the intersections are the predicted equilibrium positions of the bead. We show that different magnitude of external magnetic field strength and electrical potential can be properly combined to hold the bead at the same z height (e.g., from intersection 1 to 2) and displace the bead along z axis (e.g., from intersection 2 to 3). Material properties: the magnetic susceptibility of the bead $\chi = 0.76$, the relative permittivity of the bead equals 2.4, the relative permittivity of water 80. AC field frequency = 10MHz.

complex dielectric constant is a function of frequency and the electrical conductivity of the material. Thus, depending on properties of the particle vs. the surrounding medium and the characteristics of the electric field, the net DEP force can be either positive (pDEP) or negative (nDEP). In case of polymeric beads suspended in dilute aqueous buffers and sufficiently high AC frequencies, the DEP force will always be negative (nDEP)(128). Numerical Simulations suggested that for the designs that we have chosen, both F_{MAP} and F_{DEP} in the ranges of 0.3pN to 3pN can be achieved (**Figure 40**).

<div align="center">**Materials and Methods**</div>

Microfabrication

Device fabrication was completed on an oxide insulated Si wafer, using a combination of E-beam lithography, UV photolithography, and standard evaporation and liftoff processes (*see Figure 1D for fabrication workflow)*. Dimensions of magnetic pads were 2.5 μm in diameter, with 150nm thickness of Ni, and 80nm thickness of Au. Gold DEP electrodes were 8 μm in length by 2.5 μm in width. The chip surface consisted of a 17x30 array of magnetic pads, flanked by an 18x30 array of interdigitated DEP electrodes. The microfluidic flow channel had inner dimensions of 300 μm in width, and 20 μm in height, and was produced in PDMS. Master mold of the microfluidic flow chamber was patterned onto a Si wafer using SU-8 photoresist, and the PDMS flow chambers were formed by pouring Sylgard 184 (10:1) into molds and curing overnight at 90 °C. PDMS chambers were aligned and bonded to microfabricated device, and capillary tubing was bonded to the inlet/outlet ports of the PDMS channel.

Surface chemistry and bead preparation

Oxide surface surrounding magnetic pads was treated by 3-aminopropyltriethoxysilane, followed by mPEG-NHS (5,000MW) to reduce surface adhesion. A self-assembled monolayer (SAM) of alkanethiols (5% -COOH terminated, 95% -OH terminated) was assembled on the nickel/gold magnetic pads by overnight adsorption from a 2mM solution of alkanethiols in ethanol. Recombinant protein fragments of fibronectin (FN9-10) was immobilized to the magnetic pads using standard NHS/EDC chemistry. Superparamagnetic beads with amine surface functionality (Dynalbeads M-270, 2.8μm diameter) were prepared per manufacturer's instructions: 2×10^8 beads in 100 μL 0.1M MES, pH 4.5, and conjugated to antibodies (4mg/mL) using NHS/EDC chemistry.

Experimental Procedure
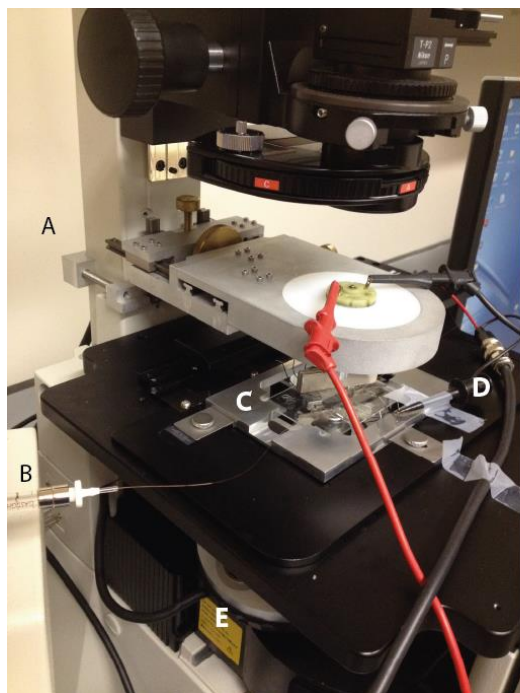
A. Magnet holder with x, y, and x directional control, and rotatational control

B. Syringe attached to syringe pump

C. MAP-DEP chip on stage holder

D. Wires to connect DEP electrodes to function generator

E. Epi-illumination with arc lamp

Figure 41. Microscope configuration for imaging and movie capture.

The MAP-DEP device was assembled on microscope stage (Nikon Eclipse T*i*) as illustrated in (**Figure 41**), and channels were flushed with deionized water, using a 25 μL glass syringe driven by a syringe pump (KDS-230, KD Scientific). Superparamagnetic beads were diluted 1:10 in 0.1X PBS and injected into the channel at 5 μl/min, with rotating external magnet to disperse beads and capture single beads to magnetic pads. For DEP force generation, electrodes were connected to a function generator (Agilent 33522A), and a sinusoidal waveform (10MHz, 10Vpp) was applied.

Results

Design of the combined magnetic and dielectrophoresis bead tweezer (**Figure 39A**) consisted of Ni/Au soft magnetic pads flanked by Au electrodes in an arrayed format: (1) the Ni/Au pads can be magnetized in the presence of an external magnetic field, generating the attractive F_{MAP} force to capture magnetic beads, (2) the interdigitated Au electrodes were used to generate the nDEP force used to tweeze captured beads for out-of-plane
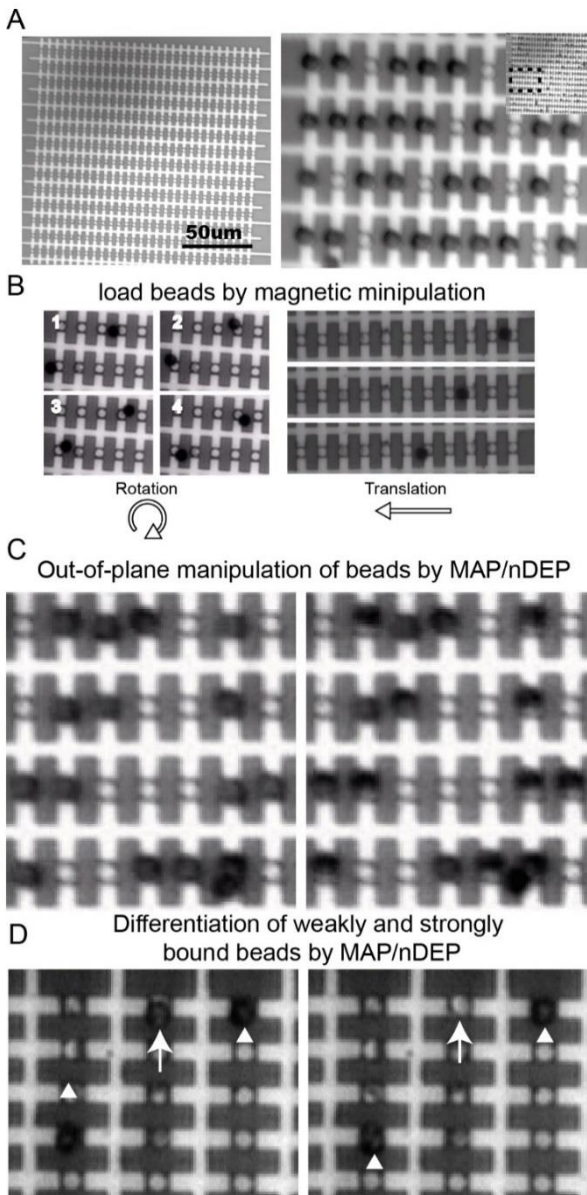
Figure 42. Loading and parallel manipulation of beads by MAP and DEP forces. A) Loading of paramagnetic beads onto magnetic pads on chip surface. Before beads were injected (left), after loading was completed (right), inset, full chip surface showing distribution of beads, scalebar = 50 μm. **B)** Coverage and distribution of beads on chip surface optimized by control of external permanent magnet. Rotation of magnet (top panel) can minimize multiple beads per pad and, translation of magnet (bottom panels) can transport beads and distribute beads over the chip surface. **C)** DEP force can be used for out-of-plane manipulation of bead position. In the case of free floating beads near the surface (arrow), turning off the DEP force will "snap" the beads to the magnetic pads (top panel). Likewise, beads loaded to the magnetic pads can be displaced upwards by the DEP force, and weakly attached beads can be removed (arrow).

displacement. The fabrication procedure (**Figure 39D**) was such that only the gold on the

magnetic pads is exposed to solvent, such that relevant biomolecules can be specifically

immobilized only to the magnetic pad regions using Au-specific chemical coupling strategies. Specific protein-protein interactions can then be probed (**Figure 39B, C**) in which weak non-specific bound beads can be displaced by nDEP, while the specifically bound beads are more strongly attached and retained.
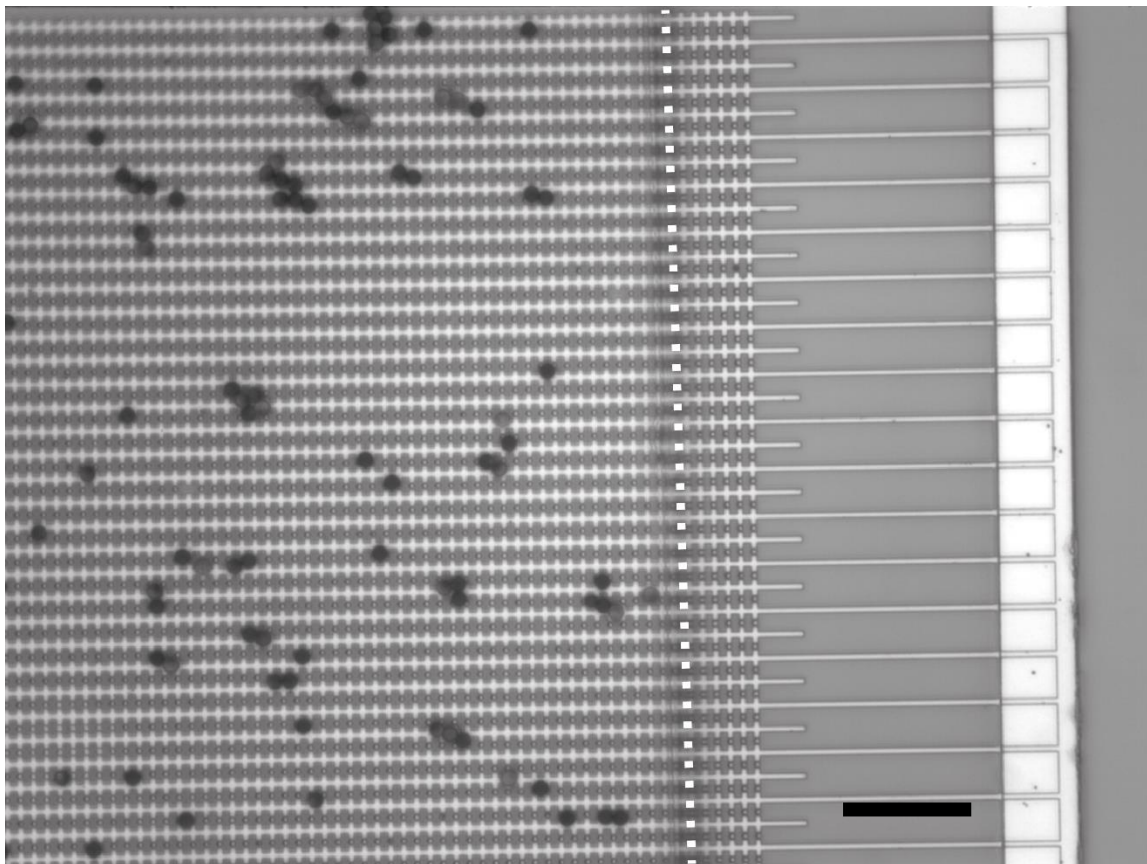
Figure 43. Loading of 2.8 μm beads on chips with 1 μm pads. Dashed lines show edge of microfluidic channel. Scalebar is 50 μm.

Representative images demonstrating the uniformity of bead loading onto magnetic pads (**Figure 42**) showed that good uniformity of loading can be achieved using only the attractive F_{MAP}. The geometry and spacing (2.5 μm diameter pad) is very important and should closely match the cross sectional area of the bead (2.8 μm diameter), as loading experiments using 1 μm diameter magnetic pads with 2.8 μm diameter beads resulted in uneven loading and low surface coverage (**Figure 43**). Furthermore, the rows in the arrays of magnetic pads were spaced at a distance less than one bead diameter apart, which helped

in increasing surface density of the pads as well as helped minimize capturing of multiple beads per pad. To further ensure a single bead per pad, rotation of the external magnet can be used to "kick-off" any extra beads that may have been loaded onto any single pad (**Figure 42B**). Additionally, translation of the external magnet in the x-y plane can transport beads across the magnetic pad array, further improving uniformity in surface coverage (**Figure 42B**).
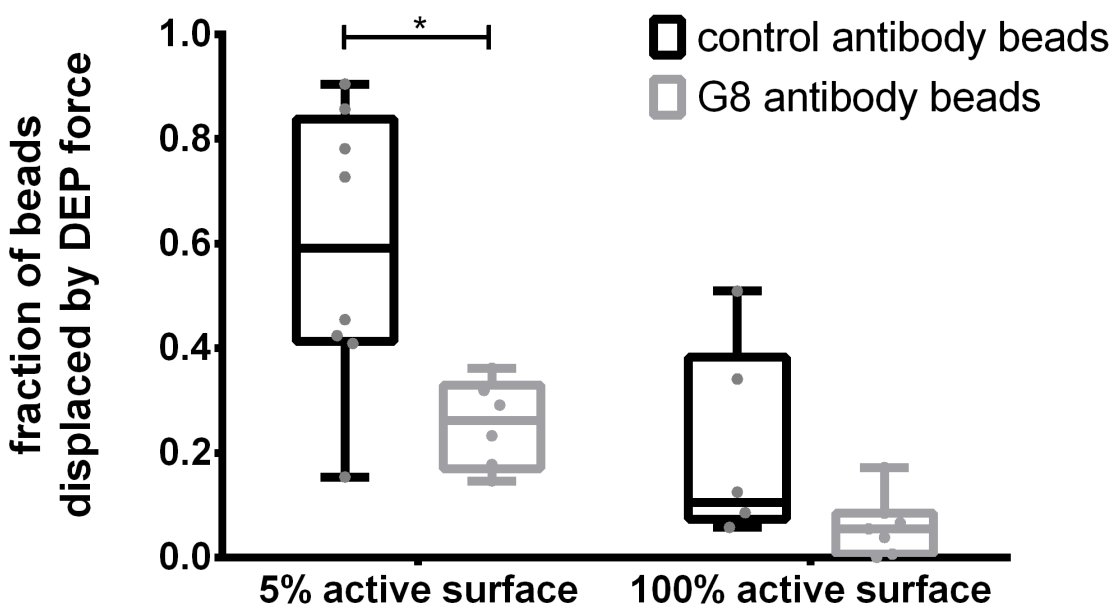
Figure 44. Specific versus non-specific antibody-antigen interactions probed with bead DEP displacement assay. Each data point represents one independent experiment, at least 20 beads were analyzed per experiment. Statistical analysis was performed by t-test, (*, $p<0.05$)

The DEP force (F_{DEP}) can also be used in conjunction with F_{MAP} to capture beads. For a free floating bead close to the surface, turning off the repulsive F_{DEP} can "snap" the bead to the magnetic pad, via the attractive F_{MAP}. (**Figure 42C, top panels**) Conversely, for weakly bound beads, applying F_{DEP} can completely dislodge beads (**Figure 42, bottom panels**) and cause them to float away from the plane of focus. Indeed, this is the mechanism that we chose to explore in assaying the specificity of protein-protein interactions.

As a proof-of-principle demonstration of probing a specific protein-protein interaction, a model protein (Fn fragment spanning the 9th and 10th type III repeats, FN9-10) was immobilized to the chip surface by covalent coupling to active groups on a SAM layer. The DEP tweezing response of two antibody coated superparamagnetic beads was compared (**Figure 44**).
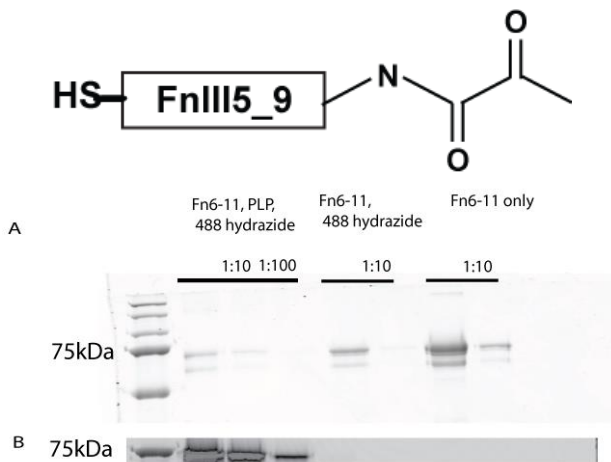
Figure 45. N-terminal modification of Fn fragments by one-step reaction and purification with pyridoxal L-phosphate (PLP). A) SDS-PAGE gel of purified Fn fragment with incubation of both PLP and Alexa 488 hydrazide (left), with Alexa 488 hydrazide alone (middle), or Fn fragments alone (right) **B)** Modified Fn fragment was detected by ketone-specific binding of Alexa 488 hydrazide.

In one group, the beads were conjugated with a specific antibody against FN9-10 (G8 antibody, binding affinity to FN9-10 with $K_D = 56$nM); in the other group beads were conjugated to a control antibody with no binding to FN9-10. At a low level of FN9-10 protein conjugated to the chip surface (5% active surface), the control antibody coated beads were significantly more responsive to DEP displacement when compared to G8 antibody coated beads (59% median responsive vs. 26% median responsive). However, at a high level of protein conjugated to the chip surface (100% active surface), both types of beads were more strongly attached and resistant to DEP tweezing. At this high surface concentration of FN9-10, the difference in DEP responsiveness between control and G8 beads was not statistically significant at a p-value of 0.05 (10% median responsive vs. 5.5% median responsive). This is likely attributed to non-specific protein-protein interactions, at

high protein concentrations these may exceed the magnitude of the DEP force needed to displace the beads. It is worth noting that a significant but constant fraction (~ 10%) of the beads are strongly adhered to the surface, regardless of protein conjugation to chip surface or bead-antibody preparation. These strong adhesions to the substrate may be mediated by contact forces between topological features on the bead to defects on the chip surface. For this reason, optimization of surface chemistries may improve sensitivities of this method at high surface protein concentrations.

Discussions and Conclusions

We have designed an integrated magnetic and dielectrophoresis based platform for nDEP displaced based characterization of specific protein-protein interactions. We used soft magnetic pads on the assay chip surface to evenly capture and distribute superparamagnetic beads to the fingers of the interdigitated DEP electrodes. We then used nDEP to repel and displace beads away from the surface. As a proof of principle demonstration, we show the ability to distinguish between specific antibody coated beads and control non-specific antibody coated beads, at low surface protein coating densities. This platform allows for the potential integration with other bead based immunoassays. Furthermore, the magnetic capture, rotation, and bead transport methods described here

may have utility for bead mixing and separation in microfluidic bioassays.
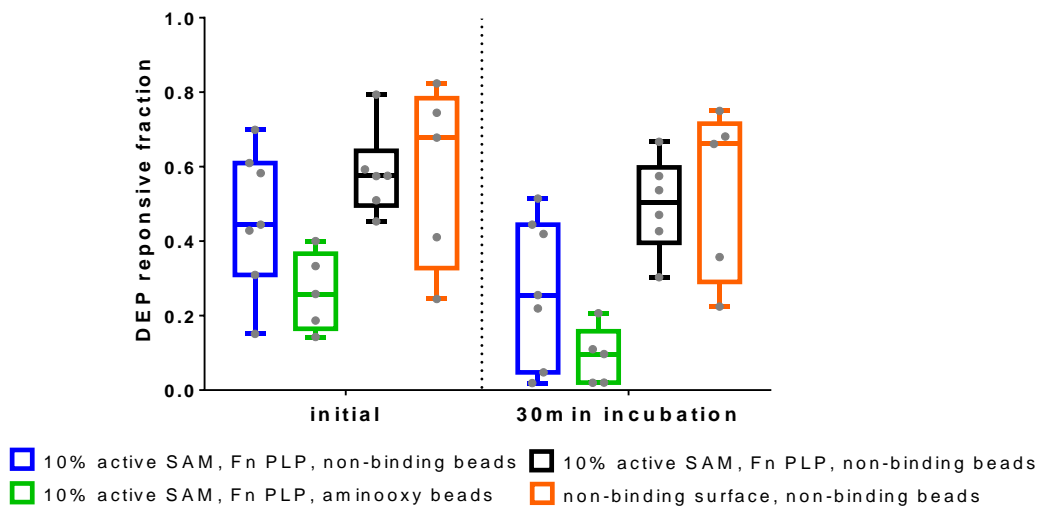
Figure 46. Displacement of Fn fragment-aminooxy beads by DEP. Percentage of magnetic beads loaded onto MAP pads that respond to a 10Vpp step change in DEP.

In preliminary experiments of applying this system to study unfolding of Fn type III repeats, we decided to chemically modify Fn type III repeat fragments to contain a N-terminal ketone group(134), and used oxime ligation to selectively couple the N-terminus of the modified Fn fragments to magnetic beads modified with aminooxy functionality, following published reports of specific oxime ligation for coupling proteins(135-142). The N-terminal modification of recombinant Fn fragments was successfully completed and verified by detection of the ketone functionality (**Figure 45**).

In experiments where recombinant Fn fragments were covalently coupled to an activated SAM surface at the C-terminus, and to the superparamagnetic beads via oxime chemistry at the N-terminus, we observed that strong adhesion to both the surface and the beads (**Figure 46**) and resistance to movement by DEP. In experimental conditions where 10% active surface, Fn fragments with N-terminal ketone groups "Fn PLP" and aminooxy beads where used, only approximately 10% of the loaded beads responded to a 10V step change in DEP force application after 30 minutes of incubation after loading. The strong tethering of the beads suggests that the covalent oxime ligation has occurred, but perhaps

the constrained displacement is not detectable with our current microscopy capabilities. In addition, confounding factors may also include significant non-specific interactions between the Fn fragment coated surface and the beads, as well as likely multiple Fn-fragment binding to a single bead. Future research may focus on improving microscopy methods, such as quantitative imaging by analysis of bead diffraction fringe patterns upon z-axial change, and also exploring alternative surface chemistry and coupling strategies between Fn fragments and magnetic beads.

REFERENCES

1. Pankov R & Yamada KM (2002) Fibronectin at a glance. *J Cell Sci* 115(Pt 20):3861-3863.
2. Mosher DF (1993) Assembly of Fibronectin into Extracellular-Matrix. *Curr Opin Struc Biol* 3(2):214-222.
3. Mao Y & Schwarzbauer JE (2005) Fibronectin fibrillogenesis, a cell-mediated matrix assembly process. *Matrix Biol* 24(6):389-399.
4. Ruoslahti E (1988) Fibronectin and Its Receptors. *Annu Rev Biochem* 57:375-413.
5. Steffensen B, Wallon UM, & Overall CM (1995) Extracellular-Matrix Binding-Properties of Recombinant Fibronectin Type Ii-Like Modules of Human 72-Kda Gelatinase Type-Iv Collagenase - High-Affinity Binding to Native Type-I Collagen but Not Native Type-Iv Collagen. *Journal of Biological Chemistry* 270(19):11555-11566.
6. Krammer A, Lu H, Isralewitz B, Schulten K, & Vogel V (1999) Forced unfolding of the fibronectin type III module reveals a tensile molecular recognition switch. *P Natl Acad Sci USA* 96(4):1351-1356.
7. Erickson HP (1994) Reversible Unfolding of Fibronectin Type-Iii and Immunoglobulin Domains Provides the Structural Basis for Stretch and Elasticity of Titin and Fibronectin. *P Natl Acad Sci USA* 91(21):10114-10118.
8. Singh P, Carraher C, & Schwarzbauer JE (2010) Assembly of Fibronectin Extracellular Matrix. *Annu Rev Cell Dev Bi* 26:397-419.
9. Oberhauser AF, Fernandez-Badilla C, & Fernandez JM (2002) The mechanical conformations of a fibronectin module captured with force spectroscopy. *Biophys J* 82(1):41a-41a.
10. Vogel V (2008) COLL 254-Mechano-sensitive protein assemblies: Insights from the study of fibronectin fibers and talin. *Abstr Pap Am Chem S* 236.
11. Krammer A, Lu H, Isralewitz B, Schulten K, & Vogel V (1999) The fibronectin type III10 module: A tensile molecular recognition switch. *Biophys J* 76(1):A9-A9.
12. Vogel V (2006) Mechanotransduction involving multimodular proteins: Converting force into biochemical signals. *Annu Rev Bioph Biom* 35:459-488.
13. Vogel V & Hytonen VP (2008) How force might activate talin's vinculin binding sites: SMD reveals a structural mechanism. *Plos Comput Biol* 4(2).
14. Li LW, Huang HHL, Badilla CL, & Fernandez JM (2005) Mechanical unfolding intermediates observed by single-molecule force spectroscopy in a fibronectin type III module. *J Mol Biol* 345(4):817-826.
15. Oberhauser AF, Badilla-Fernandez C, Carrion-Vazquez M, & Fernandez JM (2002) The mechanical hierarchies of fibronectin observed with single-molecule AFM. *J Mol Biol* 319(2):433-447.
16. Craig D, Krammer A, Schulten K, & Vogel V (2001) Comparison of the early stages of forced unfolding for fibronectin type III modules. *P Natl Acad Sci USA* 98(10):5590-5595.

17. Lemmon CA, Ohashi T, & Erickson HP (2011) Probing the folded state of fibronectin type III domains in stretched fibrils by measuring buried cysteine accessibility. *J Biol Chem* 286(30):26375-26382.
18. Erickson HP (2002) Stretching fibronectin. *J Muscle Res Cell M* 23(5-6):575-580.
19. Akke M, Liu J, Cavanagh J, Erickson HP, & Palmer AG (1998) Pervasive conformational fluctuations on microsecond time scales in a fibronectin type III domain. *Nat Struct Biol* 5(1):55-59.
20. Wierzbicka-Patynowski I & Schwarzbauer JE (2003) The ins and outs of fibronectin matrix assembly. *J Cell Sci* 116(16):3269-3276.
21. Gutman A & Kornblihtt AR (1987) Identification of a 3rd Region of Cell-Specific Alternative Splicing in Human Fibronectin Messenger-Rna. *P Natl Acad Sci USA* 84(20):7179-7182.
22. Kornblihtt AR, Umezawa K, Vibepedersen K, & Baralle FE (1985) Primary Structure of Human Fibronectin - Differential Splicing May Generate at Least 10 Polypeptides from a Single Gene. *Embo J* 4(7):1755-1759.
23. Kornblihtt AR, Vibepedersen K, & Baralle FE (1984) Human Fibronectin - Cell Specific Alternative Messenger-Rna Splicing Generates Polypeptide-Chains Differing in the Number of Internal Reports. *Nucleic Acids Res* 12(14):5853-5868.
24. Inoue T, Nabeshima K, Shimao Y, Meng JY, & Koono M (2001) Regulation of fibronectin expression and splicing in migrating epithelial cells: Migrating MDCK cells produce a lesser amount of, but more active, fibronectin. *Biochem Bioph Res Co* 280(5):1262-1268.
25. Niimi T*, et al.* (2001) Letter to the Editor: NMR structure of human fibronectin EDA. *J Biomol Nmr* 21(3):281-284.
26. Manabe R, Ohe N, Maeda T, Fukuda T, & Sekiguchi K (1997) Modulation of cell-adhesive activity of fibronectin by the alternatively spliced EDA segment. *J Cell Biol* 139(1):295-307.
27. Plow EF, Haas TA, Zhang L, Loftus J, & Smith JW (2000) Ligand binding to integrins. *J Biol Chem* 275(29):21785-21788.
28. Busby TF*, et al.* (1995) Heparin-Binding by Fibronectin Module-Iii-13 Involves 6 Discontinuous Basic Residues Brought Together to Form a Cationic Cradle. *J Biol Chem* 270(31):18558-18562.
29. Hauzenberger D, Olivier P, Gundersen D, & Ruegg C (1999) Tenascin-C inhibits beta 1 integrin-dependent T lymphocyte adhesion to fibronectin through the binding of its fnlll 1-5 repeats to fibronectin. *Eur J Immunol* 29(5):1435-1447.
30. Midwood KS & To WS (2011) Identification of Novel and Distinct Binding Sites within Tenascin-C for Soluble and Fibrillar Fibronectin. *J Biol Chem* 286(17):14881-14891.
31. Hynes RO (2009) The Extracellular Matrix: Not Just Pretty Fibrils. *Science* 326(5957):1216-1219.
32. Mullen LM*, et al.* (2008) Novel adhesin from Pasteurella multocida that binds to the integrin-binding fibronectin FnIII(9-10) repeats. *Infect Immun* 76(3):1093-1104.

33. Frick IM, Crossin KL, Edelman GM, & Bjorck L (1995) Protein-H - a Bacterial Surface Protein with Affinity for Both Immunoglobulin and Fibronectin Type-Iii Domains. *Embo J* 14(8):1674-1679.

34. Zhong CL*, et al.* (1998) Rho-mediated contractility exposes a cryptic site in fibronectin and induces fibronectin matrix assembly. *J Cell Biol* 141(2):539-551.

35. Hocking DC, Sottile J, & Mckeownlongo PJ (1994) Fibronectins Iii-1 Module Contains a Conformation-Dependent Binding-Site for the Amino-Terminal Region of Fibronectin. *J Biol Chem* 269(29):19183-19191.

36. Campbell ID, Vakonakis I, Staunton D, & Rooney LM (2007) Interdomain association in fibronectin: insight into cryptic sites and fibrillogenesis. *Embo J* 26(10):2575-2583.

37. Marchina E & Barlati S (1996) Degradation of human plasma and extracellular matrix fibronectin by tissue type plasminogen activator and urokinase. *Int J Biochem Cell B* 28(10):1141-1150.

38. Gold LI, Rostagno A, Frangione B, & Passalaris T (1992) Localization of the Cleavage Sites on Fibronectin Following Digestion by Urokinase. *J Cell Biochem* 50(4):441-452.

39. Hu P & Luo BH (2013) Integrin bi-directional signaling across the plasma membrane. *J Cell Physiol* 228(2):306-312.

40. Fu G, Wang W, & Luo BH (2012) Overview: structural biology of integrins. *Methods in molecular biology* 757:81-99.

41. Carman CV & Springer TA (2003) Integrin avidity regulation: are changes in affinity and conformation underemphasized? *Curr Opin Cell Biol* 15(5):547-556.

42. Boettiger D (2012) Mechanical control of integrin-mediated adhesion and signaling. *Curr Opin Cell Biol* 24(5):592-599.

43. Stupack DG, Puente XS, Boutsaboualoy S, Storgard CM, & Cheresh DA (2001) Apoptosis of adherent cells by recruitment of caspase-8 to unligated integrins. *J Cell Biol* 155(3):459-470.

44. Jacquemet G, Humphries MJ, & Caswell PT (2013) Role of adhesion receptor trafficking in 3D cell migration. *Curr Opin Cell Biol*.

45. Ye F, Kim C, & Ginsberg MH (2012) Reconstruction of integrin activation. *Blood* 119(1):26-33.

46. Ross TD*, et al.* (Integrins in mechanotransduction. *Curr Opin Cell Biol* (0).

47. Akiyama SK (1996) Integrins in cell adhesion and signaling. *Human cell* 9(3):181-186.

48. Boregowda RK, Krovic BM, & Ritty TM (2012) Selective integrin subunit reduction disrupts fibronectin extracellular matrix deposition and fibrillin 1 gene expression. *Molecular and cellular biochemistry* 369(1-2):205-216.

49. Mittal A, Pulina M, Hou SY, & Astrof S (2013) Fibronectin and integrin alpha 5 play requisite roles in cardiac morphogenesis. *Developmental biology*.

50. Giros A, Grgur K, Gossler A, & Costell M (2011) alpha5beta1 integrin-mediated adhesion to fibronectin is required for axis elongation and somitogenesis in mice. *PLoS One* 6(7):e22002.

51. Martino MM*, et al.* (2009) Controlling integrin specificity and stem cell differentiation in 2D and 3D environments through regulation of fibronectin domain stability. *Biomaterials* 30(6):1089-1097.

52. Schiller HB, *et al.* (2013) beta(1)- and alpha(v)-class integrins cooperate to regulate myosin II during rigidity sensing of fibronectin-based microenvironments. *Nat Cell Biol* 15(6):625-U422.

53. Frank AO, *et al.* (2010) Conformational control of integrin-subtype selectivity in isoDGR peptide motifs: a biological switch. *Angew Chem Int Ed Engl* 49(48):9278-9281.

54. Smith GP & Petrenko VA (1997) Phage display. *Chem Rev* 97(2):391-410.

55. Brissette R & Goldstein NI (2007) The use of phage display peptide libraries for basic and translational research. *METHODS IN MOLECULAR BIOLOGY-CLIFTON THEN TOTOWA-* 383:203.

56. Jungbauer A & Mersich C (2008) Generation of bioactive peptides by biological libraries. *J Chromatogr B* 861(2):160-170.

57. Weiss GA & Penner RM (2008) The promise of phage display: Customized affinity and specificity. *Anal Chem* 80(9):3082-3089.

58. Banta S, Dooley K, & Shur O (2013) Replacing Antibodies: Engineering New Binding Proteins. *Annu Rev Biomed Eng* 15(1):93-113.

59. Rodi DJ & Makowski L (1999) Phage-display technology - finding a needle in a vast molecular haystack. *Curr Opin Biotech* 10(1):87-93.

60. Burritt JB, Bond CW, Doss KW, & Jesaitis AJ (1996) Filamentous phage display of oligopeptide libraries. *Anal Biochem* 238(1):1-13.

61. Smothers JF, Henikoff S, & Carter P (2002) Affinity selection from biological libraries. *Science* 298(5593):621-622.

62. Pasqualini R, Koivunen E, & Ruoslahti E (1995) A Peptide Isolated from Phage Display Libraries Is a Structural and Functional Mimic of an Rgd-Binding Site on Integrins. *J Cell Biol* 130(5):1189-1196.

63. Walter N, Collard HR, & King TE, Jr. (2006) Current perspectives on the treatment of idiopathic pulmonary fibrosis. *Proceedings of the American Thoracic Society* 3(4):330-338.

64. Loomis-King H, Flaherty KR, & Moore BB (2013) Pathogenesis, current treatments and future directions for idiopathic pulmonary fibrosis. *Current opinion in pharmacology*.

65. Zhou Y, *et al.* (2013) Inhibition of mechanosensitive signaling in myofibroblasts ameliorates experimental pulmonary fibrosis. *The Journal of clinical investigation* 123(3):1096-1108.

66. Bennett KM, *et al.* (2013) Ephrin-B2 Reverse Signaling Increases alpha5beta1 Integrin Mediated Fibronectin Deposition and Reduces Distal Lung Compliance. *American journal of respiratory cell and molecular biology*.

67. Brown AC, Fiore VF, Sulchek TA, & Barker TH (2013) Physical and chemical microenvironmental cues orthogonally control the degree and duration of fibrosis-associated epithelial-to-mesenchymal transitions. *J Pathol* 229(1):25-35.

68. Caravan P, *et al.* (2013) Molecular magnetic resonance imaging of pulmonary fibrosis in mice. *American journal of respiratory cell and molecular biology* 49(6):1120-1126.

69. Cai Y, *et al.* (2013) Non-Invasive Monitoring of Pulmonary Fibrosis by Targeting Matrix Metalloproteinases (MMPs). *Molecular pharmaceutics*.

70. Smith ML*, et al.* (2007) Force-induced unfolding of fibronectin in the extracellular matrix of living cells. *Plos Biol* 5(10):2243-2254.

71. Little WC, Smith ML, Ebneter U, & Vogel V (2008) Assay to mechanically tune and optically probe fibrillar fibronectin conformations from fully relaxed to breakage. *Matrix Biol* 27(5):451-461.

72. Ulmer J, Geiger B, & Spatz JP (2008) Force-induced fibronectin fibrillogenesis in vitro. *Soft Matter* 4(10):1998-2007.

73. Ahmed Z & Brown RA (1999) Adhesion, alignment, and migration of cultured Schwann cells on ultrathin fibronectin fibres. *Cell Motil Cytoskel* 42(4):331-343.

74. Ejim OS, Blunn GW, & Brown RA (1993) Production of Artificial-Oriented Mats and Strands from Plasma Fibronectin - a Morphological-Study. *Biomaterials* 14(10):743-748.

75. Poulouin L, Gallet O, Rouahi M, & Imhoff JM (1999) Plasma fibronectin: Three steps to purification and stability. *Protein Expres Purif* 17(1):146-152.

76. Vogel V, Little WC, Schwartlander R, Smith ML, & Gourdon D (2009) Stretched Extracellular Matrix Proteins Turn Fouling and Are Functionally Rescued by the Chaperones Albumin and Casein. *Nano Lett* 9(12):4158-4167.

77. Ruoslahti E (1996) RGD and other recognition sequences for integrins. *Annu. Rev. Cell Dev. Biol.* 12:697-715.

78. Hersel U, Dahmen C, & Kessler H (2003) RGD modified polymers: biomaterials for stimulated cell adhesion and beyond. *Biomaterials* 24(24):4385-4415.

79. Temming K, Schiffelers RM, Molema G, & Kok RJ (2005) RGD-based strategies for selective delivery of therapeutics and imaging agents to the tumour vasculature. *Drug Resist. Update* 8(6):381-402.

80. Barker TH*, et al.* (2009) Controlling integrin specificity and stem cell differentiation in 2D and 3D environments through regulation of fibronectin domain stability. *Biomaterials* 30(6):1089-1097.

81. Shroff K, Pearce TR, & Kokkoli E (2012) Enhanced Integrin Mediated Signaling and Cell Cycle Progression on Fibronectin Mimetic Peptide Amphiphile Monolayers. *Langmuir* 28(3):1858-1865.

82. Mardilovich A, Craig JA, McCammon MQ, Garg A, & Kokkoli E (2006) Design of a novel fibronectin-mimetic peptide-amphiphile for functionalized biomaterials. *Langmuir* 22(7):3259-3264.

83. Craig JA, Rexeisen EL, Mardilovich A, Shroff K, & Kokkoli E (2008) Effect of linker and spacer on the design of a fibronectin-mimetic peptide evaluated via cell studies and AFM adhesion forces. *Langmuir* 24(18):10282-10292.

84. Shroff K, Rexeisen EL, Arunagirinathan MA, & Kokkoli E (2010) Fibronectin-mimetic peptide-amphiphile nanofiber gels support increased cell adhesion and promote ECM production. *Soft Matter* 6(20):5064-5072.

85. Atchison NA*, et al.* (2010) Binding of the Fibronectin-Mimetic Peptide, PR_b, to alpha(5)beta(1) on Pig Islet Cells Increases Fibronectin Production and Facilitates Internalization of PR_b Functionalized Liposomes. *Langmuir* 26(17):14081-14088.

86. Pangburn TO, Bates FS, & Kokkoli E (2012) Polymersomes functionalized via "click" chemistry with the fibronectin mimetic peptides PR_b and GRGDSP for

targeted delivery to cells with different levels of alpha(5)beta(1) expression. *Soft Matter* 8(16):4449-4461.

87.   Levine RM, Scott CM, & Kokkoli E (2013) Peptide functionalized nanoparticles for nonviral gene delivery. *Soft Matter* 9(4):985-1004.

88.   Adil M*, et al.* (2013) PR_b functionalized stealth liposomes for targeted delivery to metastatic colon cancer. *Biomaterials Science* 1(4):393-401.

89.   van der Walle CF, Altroff H, & Mardon HJ (2002) Novel mutant human fibronectin FIII9-10 domain pair with increased conformational stability and biological activity. *Protein Eng* 15(12):1021-1024.

90.   Humphries MJ (2001) Cell-Substrate Adhesion Assays. *Current Protocols in Cell Biology*, (John Wiley & Sons, Inc.).

91.   Gallant ND, Michael KE, & Garcia AJ (2005) Cell adhesion strengthening: Contributions of adhesive area, integrin binding, and focal adhesion assembly. *Molecular Biology of the Cell* 16(9):4329-4340.

92.   Cutler SM & Garcia AJ (2003) Engineering cell adhesive surfaces that direct integrin alpha5beta1 binding using a recombinant fragment of fibronectin. *Biomaterials* 24(10):1759-1770.

93.   Petrie TA, Capadona JR, Reyes CD, & Garcia AJ (2006) Integrin specificity and enhanced cellular activities associated with surfaces presenting a recombinant fibronectin fragment compared to RGD supports. *Biomaterials* 27(31):5459-5470.

94.   Lee CM, Iorno N, Sierro F, & Christ D (2007) Selection of human antibody fragments by phage display. *Nature protocols* 2(11):3001-3008.

95.   de Wildt RM, Mundy CR, Gorick BD, & Tomlinson IM (2000) Antibody arrays for high-throughput screening of antibody-antigen interactions. *Nature biotechnology* 18(9):989-994.

96.   Wu CY, Bauer JS, Juliano RL, & Mcdonald JA (1993) The Alpha-5-Beta-1 Integrin Fibronectin Receptor, but Not the Alpha-5 Cytoplasmic Domain, Functions in an Early and Essential Step in Fibronectin Matrix Assembly. *Journal of Biological Chemistry* 268(29):21883-21888.

97.   Gianni T, Leoni V, Chesnokova LS, Hutt-Fletcher LM, & Campadelli-Fiume G (2012) alphavbeta3-integrin is a major sensor and activator of innate immunity to herpes simplex virus-1. *Proc Natl Acad Sci U S A* 109(48):19792-19797.

98.   Blystone SD, Graham IL, Lindberg FP, & Brown EJ (1994) Integrin alpha v beta 3 differentially regulates adhesive and phagocytic functions of the fibronectin receptor alpha 5 beta 1. *J Cell Biol* 127(4):1129-1137.

99.   Gianni T*, et al.* (2010) Herpes simplex virus glycoproteins H/L bind to cells independently of {alpha}V{beta}3 integrin and inhibit virus entry, and their constitutive expression restricts infection. *Journal of virology* 84(8):4013-4025.

100.   Meng X*, et al.* (2005) Evidence for the presence of a low-mass beta1 integrin on the cell surface. *J Cell Sci* 118(Pt 17):4009-4016.

101.   Tsuchida J, Ueki S, Saito Y, & Takagi J (1997) Classification of 'activation' antibodies against integrin beta1 chain. *FEBS Lett* 416(2):212-216.

102.   Takagi J, Strokovich K, Springer TA, & Walz T (2003) Structure of integrin alpha(5)beta(1) in complex with fibronectin. *Embo J* 22(18):4607-4615.

103. Liu YQ, Pan YJ, & Xu YH (2010) Binding Investigation of Integrin alpha(v)beta(3) With Its Inhibitors by SPR Technology and Molecular Docking Simulation. *J Biomol Screen* 15(2):131-137.
104. Altroff H, *et al.* (2004) Interdomain tilt angle determines integrin-dependent function of the ninth and tenth FIII domains of human fibronectin. *J Biol Chem* 279(53):55995-56003.
105. Singh A, *et al.* (2013) Adhesion strength-based, label-free isolation of human pluripotent stem cells. *Nat Methods* 10(5):438-+.
106. Paszek MJ, *et al.* (2005) Tensional homeostasis and the malignant phenotype. *Cancer Cell* 8(3):241-254.
107. McBeath R, Pirone DM, Nelson CM, Bhadriraju K, & Chen CS (2004) Cell shape, cytoskeletal tension, and RhoA regulate stem cell lineage commitment. *Dev Cell* 6(4):483-495.
108. Alcaraz J, *et al.* (2011) Collective epithelial cell invasion overcomes mechanical barriers of collagenous extracellular matrix by a narrow tube-like geometry and MMP14-dependent local softening. *Integr Biol* 3(12):1153-1166.
109. Ghajar CM & Bissell MJ (2010) Tumor Engineering: The Other Face of Tissue Engineering. *Tissue Eng Pt A* 16(7):2153-2156.

VITA

LIZHI CAO

Lizhi Cao was born in Changchun, China. He moved do Canada, and then to California – where he attended public schools in San Jose, California. He received his B.S. in Bioengineering from UC Berkeley in 2008, before coming to Georgia Tech in to pursue a doctoral in Biomedical Engineering. When he is not working on his research, Mr. Cao enjoys exercising and fitness, traveling, as well as exploring local restaurants with friends and family.